2014

Experimental Assessment of Cement Integrity under Thermal Cycle Loading Conditions in Geopressured Geothermal Reservoirs

Kolawole Saheed Bello
Louisiana State University and Agricultural and Mechanical College, kbello1@lsu.edu

EXPERIMENTAL ASSESSMENT OF CEMENT INTEGRITY UNDER THERMAL CYCLE LOADING CONDITIONS IN GEOPRESSURED GEOTHERMAL RESERVOIRS

A Thesis

Submitted to the Graduate Faculty of the
Louisiana State University and
Agricultural and Mechanical College
in partial fulfillment of the
requirements for the degree of
Master of Science

in

The Department of Petroleum Engineering

by
Kolawole Saheed Bello
B.S., Louisiana State University, 2012
December 2014

This thesis is dedicated to my late mother and sister, Awulat and Adenike Bello

ACKNOWLEDGEMENTS

I would like to express my sincere gratitude to my major advisor, Dr. Mileva Radonjic for her guidance and support through this project. Thanks to Dr. Paulo Waltrich, Dr. Mayank Tyagi, and Dr. Stephen Sears for their vital contributions.

I wish to thank the U.S Department of Energy for sponsoring my project. Thank you to my colleagues from the Sustainable Energy and Environmental Research (SEER) group, Mr. Fenelon Nunes and Janet Dugas (LSU Department of Petroleum Engineering) for their help during this project. I would like to acknowledge Ms. Wanda Leblanc (LSU Department of Geology and Geophysics), Dr. Syam Doodla (LSU Ag Center), Dr. Dongmei Cao (LSU Shared Instrumentation Facility), and Dr. Amitava Roy (LSU Center for Advanced Microstructures and Devices) for their help with post experimental analysis. I am grateful to Richard Dubois of Halliburton Fluids Laboratory and Rodney Macon of TXI for providing additives used in this study.

Finally, I would like to thank my family and friends for their love and support. In particular I would like to express my deepest gratitude to my wonderful wife, Heidi Henry, my father, Idowu Bello, and my siblings, Yetunde, Ayobamidele, Olajide, and Oluwadamilola Bello for always been there for me.

TABLE OF CONTENTS

LIST OF TABLES

LIST OF FIGURES

ACRONYMS

C_3S	–	Tricalcium silicate
C_2S	–	Dicalcium Silicate
C_3A	–	Tricalcium Aluminate
C_4AF	–	Tetracalcium Aluminoferrite
CH	–	Calcium Hydroxide
$Ca(OH)_2$	–	Calcium Hydroxide
C-S-H	–	Calcium Silicate Hydrate
W/C	–	Water to Cement Ratio
RPM	–	Revolutions per Minute
SEM	–	Scanning Electron Microscopy
EDS	–	Electron Dispersive Spectroscopy
XPS	–	X-Ray Photoelectron Spectroscopy
MIP	–	Mercury Intrusion Porosimetry
TGA	–	Thermogravimetric Analysis
TCL	–	Thermal Cycle Loading
NC	–	Neat Cement
ST	–	Steel Fiber Cement Design
SS	–	Silica Sand Cement Design
CC	–	Calcined Clay Cement Design
GL	–	Glass Cement Design
Q	–	Quartz
CPS	–	Counts per Seconds
eV	–	Electron Volt
Ca	–	Calcium
Cl	–	Chlorine
Si	–	Silica

NOMENCLATURE

$\emptyset$	=	porosity of the core
V_b	=	core bulk volume
V_g	=	core grain volume
$\boldsymbol{\rho}_g$	=	grain density
W	=	core dry weight
μ	=	water viscosity
$\mathcal{C}_f$	=	water compressibility
V_p	=	core pore pressure
V_b	=	core bulk volume
σ	=	compressive strength
$Fmax$	=	maximum compressive force
A	=	core cross-sectional area

ABSTRACT

The number of well integrity issues increase as wells are exposed to severe downhole conditions and have longer lifetimes. Techniques for heat extraction from geopressured geothermal reservoirs involve production of hot water and injection of cold water which expose downhole materials to harsh cyclic temperature variations. Heating and cooling make the cement expand and contract as a result of thermal expansion. This volumetric change can influence cement sheaths causing them to fail. Failure of annular cement sheaths can introduce well integrity issues and subsequently lead to sustained casing pressure.

This study measures the effect of cyclic thermal loading of cement slurry designs in salt brines. Grain volume porosimeter and Liquid Pressure-pulse Decay Permeameter was used to quantify the presence of thermal fractures as it is capable of measuring brine permeability of cement under reservoir conditions. Scanning Electron Microscopy micrographs with Energy Dispersive Spectroscopy capabilities, Thermogravimetric analysis and X-Ray Photoelectron Spectroscopy were used to study the physical and chemical changes in the cement slurry designs.

Five cement designs with a range of chemical additive were subjected to 100 thermal cycles of 40^0C at 100% relative humidity in salt brine. The experimental result indicates leaching of $Ca(OH)_2$ will occur from the cement irrespective of cement composition which causes the porosity and permeability of the cement sheath to increase. Due to the thermal cycling, the strength of the cement sheath decrease. The study also shows that steel fiber can be added to the design to improve the permeability and increase the strength of the cement sheath under thermal cycle loading conditions.

Future work is essential in order to fully understand within which temperature ranges a particular well can be operated, without leaks along the annular cement sheaths. This can be

obtained by conducting tests varying the different materials in the cement mix. In addition, experimental tests determining the effect of exposing the formation to drilling fluids prior to cementing and further thermal cycling can be conducted. Effect of various wellbore scaling ratios is also important, as the effects of the total volumes on the obtained results are unknown.

CHAPTER 1: INTRODUCTION

1.1 Background

Geothermal systems serve as ample source of sustainable carbon-free energy used in the generation of electricity, space heating, and air conditioning. Compared to fossil fuels and other forms of energy, geothermal energy is renewable and is readily available. The four main types of geothermal resources are described in Table 1.1. The United States has abundance of geothermal resources (Figure 1.1) although its current capacity is relatively small compared to the resources. The current production capacity of the United State is 106 petajoules (PJ) [Geothermal Energy Association, 2013]. There is a need to increase geothermal energy production in order to meet the world energy demand. For example, the United States consumed over 40000 PJ of geothermal energy in 2012 but only 3 % (281 PJ) of that was sourced from geothermal energy according to 2013 reports from the U.S. Energy Information Administration with the other 97 % mostly sourced from petroleum, gas, and coal [U.S Energy Information Administration, 2013].

Table 1.1: Description of the four types of Geothermal Systems.

Geothermal Resource	Description
Conventional Hydrothermal Systems	Water aquifer with temperature and flow capacity that is naturally sufficient to produce electricity.
Geothermal Energy and Hydrocarbon Co-production	These type of systems use produced fluids resulting from oil and/or gas production for the production of geothermal power.
Geopressured systems	These systems use kinetic energy, hydrothermal energy, and energy produced from associated gas resulting from geopressured gas fields to produced geothermal energy.
Enhanced Geothermal Systems (EGS)	In these systems, extremely high temperatures are produced from igneous and metamorphic rocks by hydraulic fracturing.

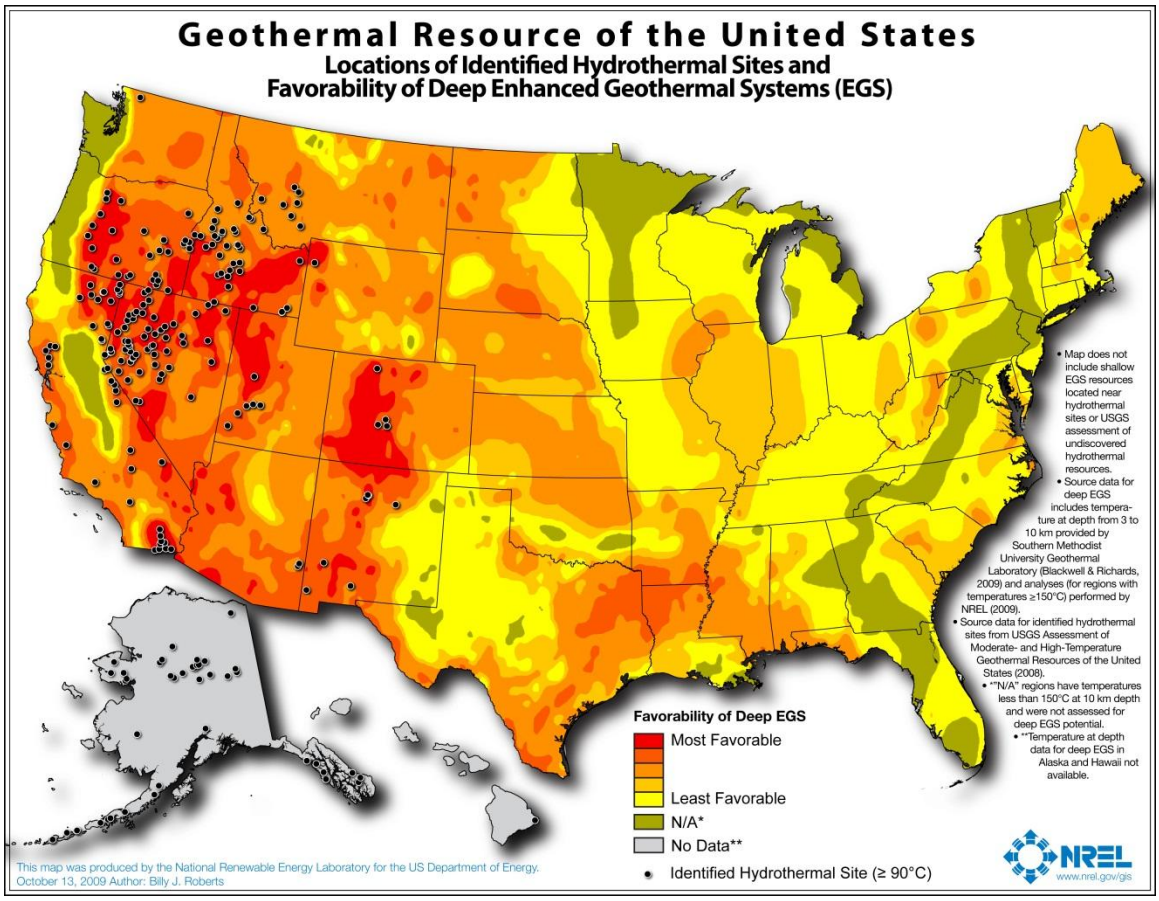

Figure 1.1: Geothermal Resource of the United States [National Renewable Energy Laboratory, 2013].

Geopressured aquifers are undercompacted brine saturated porous and permeable formations that have anomalously high pore pressures and temperatures. Geopressured geothermal reservoirs have been very unproductive due to lack of technological certainty that could lead to high production cost making it uneconomical. The main concern with producing geopressured reservoirs used to be the environmental changes brought about by the removal of vast amounts of high-pressure subsurface water and the subsequent decrease in reservoir pressures. This can result in surface subsidence or worse induce an earthquake [Herrin, 1975]. Novel wellbore system with downhole heat exchanger is been investigated for in-situ heat harvesting resulting in zero-mass withdrawal using production tubing inside a production casing making it safe to produce geopressured geothermal reservoir [Feng et al., 2011; Feng, 2012, Feng et al., 2015].

As with all geothermal wells, there is a challenge in producing geopressured reservoirs has to do with the drilling and completion process. This is always a challenge due to the durability of materials and downhole assembly including wellbore cements under high temperature. There is need for systematic studies on existing development techniques as well new technology to avoid safety and environmental issues especially after 2010's Deepwater Horizon disaster in the Gulf of Mexico. The accident showcases the importance of ensuring well integrity over the life cycle of the well.

Cement is one of the main components used in ensuring wellbore integrity. Failures in cement sheaths can lead to the contamination of fresh water aquifer, migration of reservoir fluids from high pressure sands to low pressure sands, and sustained casing pressure as a result of fluid migration from the reservoir to the surface [Guen et al., 2009; Dusseault et al., 2000; Cavanagh et al., 2007]. With in-situ heat harvesting, the wellbore cement in the production and injection zones will experience differential temperatures which can lead to three types of cement failures: failure within the cement sheaths and interface de-bonding as a result of cyclic thermal loading, cement strength retrogression due to high temperature, and cement dissolution from exposure to corrosive reservoir fluids mainly low pH high salinity brines. Leaching of $Ca(OH)_2$ and calcium silicate hydrate occur in cement during exposure to low pH conditions causing an increase in porosity, permeability, loss of strength and inability to protect the casing from corrosion [Nelson, 1990; Ekström, 2001].

1.2 Objective

The main objective of this project is to study the effect of temperature cycling on cement sheath integrity for five different cement slurries design under the harsh south Louisiana geopressured geothermal reservoir conditions. This entailed describing the current knowledge about cement failure during thermal cycling and design of cement slurries based on cement chemistry. Experiments, poro-mechanical measurements, and material characterization

techniques were used to quantify and qualify the behavior of different cement design in geopressured geothermal environments.

1.3 Methodology

A cyclic thermal loading experiment was conducted on a batch of cement cores of five different slurry designs cured in salt brine. The experiment was carried out to study the effect of production on cement under proposed wellbore conditions. Each cycle took 12 hours with the temperature ramped from 40^0C to 90^0C and back to 40^0C. The cyclic thermal loading was conducted at 100% relative humidity (RH) in a temperature cycling/relative humidity chamber (environmental chamber). Cement cores were made from 13.1 lb/gal class H cement slurry designs with approximate dimensions of 5.08cm (3in.) by 2.54cm (1in.). Porosity and permeability of the samples from the cement designs was done after the experiments. Compressive strength of the samples were measured to quantify the effect of the cyclic thermal loading on the mechanical properties of the cement while material characterization of the cement cores were done to evaluate the physical and chemical changes in the cement and compliment findings from petrophysical analysis.

CHAPTER 2: LITERATURE REVIEW

2.1 Geopressured Reservoir

Geopressured aquifers are undercompacted brine saturated porous and permeable formations that have anomalously high pore pressures and temperatures. Geopressured geothermal reservoirs have been very unproductive due to lack of technological certainty that could lead to high production cost making it uneconomical. The main concern with producing geopressured reservoirs used to be the environmental changes brought about by the removal of vast amounts of high-pressure, subsurface water and the subsequent decrease in reservoir pressures. This can result in surface subsidence or worse induce an earthquake [Herrin, 1975]. Novel wellbore system with downhole heat exchanger is been investigated for in-situ heat harvesting resulting in zero-mass withdrawal using production tubing inside a production casing making it safe to produce geopressured geothermal reservoir [Feng et al.,2011; Feng, 2012, Feng et al., 2015].

2.1.1 Geopressured-Geothermal Reservoir in the Gulf of Mexico

In the Gulf of Mexico, geopressured reservoirs form as a result of rapid sediment loading from riverborne systems and their deltas. The penetration of sands into underlying muds resulted in isolation of large sand members from the overlying strata. The weight of the sediment layer on the trapped fluids results in elevated pore pressures. These isolated units of sands and muds contain pore pressure of 15.269kPa/m (0.675psi/ft.), or higher [Griggs, 2004]. In addition, expulsion of water into sands from underlying shale as montmorillite converts to illite which/and contributes to the elevated pressure [Dorfman, 1982]. Temperatures in geopressured reservoir in the Gulf of Mexico typically range from 90^{0}C to $200+^{0}$C. Since these reservoirs have temperatures greater than 15^{0}C and are above 10km, they are classified as a geothermal resource

[White et. al, 1975]. Reservoir simulations by Ganjdanesh et al. and Plaksina suggest that production from these reservoirs would be economical when natural convection of heat from the reservoir is coupled with CO_2 sequestration [Ganjdanesh et al, 2012; Plaksina, 2011]. Camerina Sand A, a geopressured geothermal reservoir in Vermilion Parish, Louisiana is used as a case study.

2.1.2 Camerina Sand A

The properties of Camerina Sand A's geopressured geothermal aquifers can be gathered from the date of the abandoned Fairfax Foster Sutter No. 2 well located in St. Mary's parish and the Beulah Simon No. 2 well located in Vermilion Parish. Camerina Sand A is a sandstone reservoir that lies on a geosyncline in the gulf coast basin. It is made up of recent to Cretaceous age sediments bounded by the Gueydan Salt Dome from the Louann salt [Gray, 2007]. The reservoir characteristics are presented in Table 2.1.

Table 2.1: Reservoir Characteristics of the Camerina Sand [Adapted from Gray, 2007; McCoy et. al., 1980; Hanor and Mercer, 2010].

Reservoir Characteristics	
Net Thickness	0.1 km
Average Porosity	0.187
Average Permeability	12 mD
Temperature	130 ^{0}C
Reservoir Pressure	13015 psia
Salinity	98.678 g/L
Brine pH	6.61
Brine Density	1.066 g/mL

Of critical importance to this study is the brine salinity and the pH of the aquifer. The salinity is high due to dissolution of surround salt domes [Hanor and Mercer, 2010]. Table 2.2

displays the brine composition based on water analysis from the Camerina Sand. Sodium chloride, NaCl and calcium carbonate, $CaCO_3$ are the primary minerals dissolved in the brine.

Table 2.2: Brine Composition of the Camerina Sand [Adapted from McCoy et. al., 1980].

Brine Water Constituent (g/L)	
Sodium (Na)	32.19
Potassium (K)	0.454
Chloride (Cl)	50.3
Calcium (Ca)	7.87
Magnesium (Mg)	0.91
Bicarbonate(HCO_3)	0.606
Carbonate (CO_3)	0.001
Total Iron (Fe)	0.033
Sulfate (SO_4)	0.444
Dissolved Silica (Si)	0.092
Heavy Metals	0.098
Total Dissolved Solids	103.9
Total Solids	104.9

2.1.3 Proposed Wellbore System for Zero Mass Withdrawal

There is current work on a novel wellbore system for geopressured geothermal aquifers that employs downhole heat exchanger to transfer heat from hot reservoir fluid to cold working fluid [Feng et al., 2011; Feng, 2012, Feng et al., 2015]. This would allow the production of geopressured geothermal energy without inducing negative seismic events such as earthquakes or subsidence [Herrin, 1975]. The heat harvesting would occur along a lateral section of the wellbore. The reservoir fluid is produced into the production casing at the beginning of the lateral section and then injected back into the reservoir at the end of the production casing (Figure 2.1). A cold working fluid is injected from the surface, absorbs heat from the reservoir brine and is produced back at the surface as a hot fluid using downhole pump system.

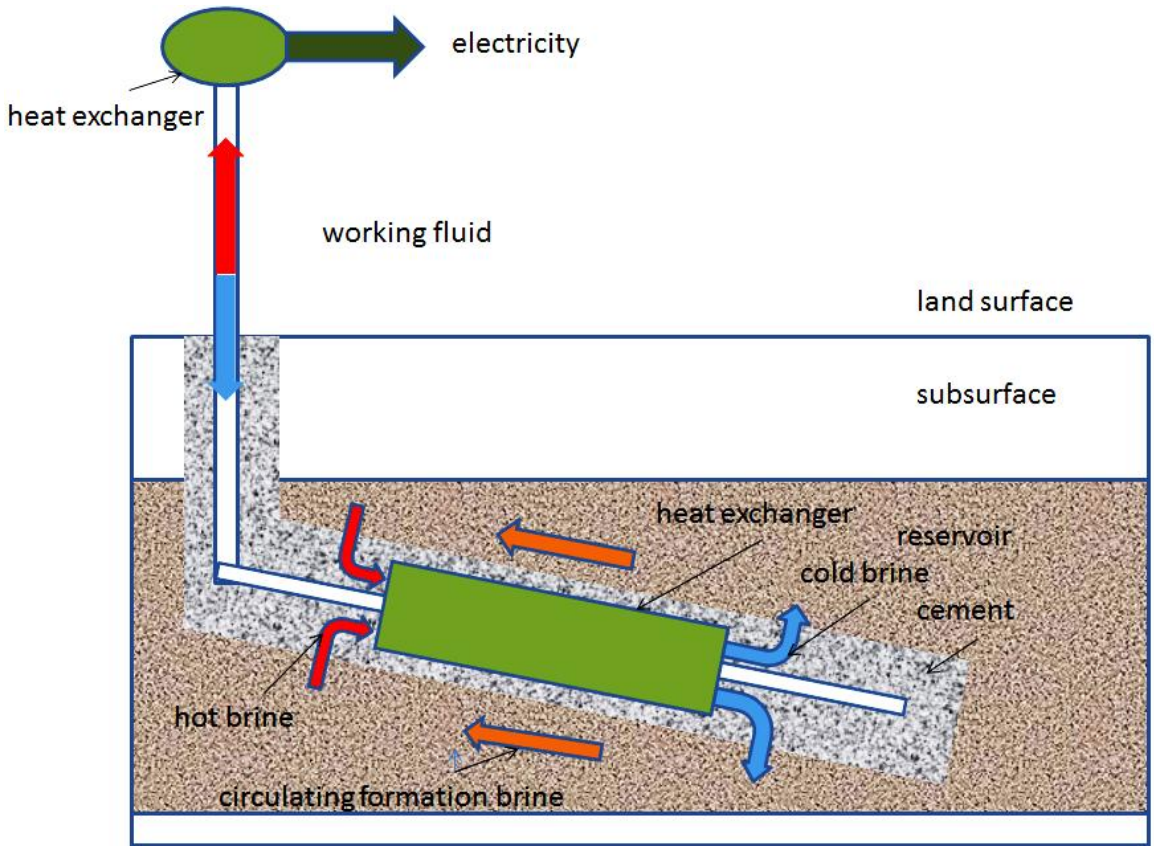

Figure 2.1: Schematic of heat extraction with downhole heat exchanger in proposed wellbore for zero mass withdrawal.

2.2 Wellbore Cement

2.2.1 Chemistry of Portland Cement

Portland cement is the most common cement used in wellbore cement slurries worldwide. It is used for primary cementing, wellbore remediation, and plug and abandonment of wells. The main function of cement in wellbores is to provide zonal isolation by preventing migration of formation fluids to the surface. It also protects the casing from corrosive formation fluids and supports the weight of the casing.

Unhydrated cement clinker is made through the fusion of limestone and clay at 1480^{0}C. Unhydrated cement contains four mineral phases commonly known as tricalcium silicate (C_3S),

dicalcium silicate (C_2S), tricalcium aluminate (C_3A) and tetracalcium aluminoferrite (C_4AF) as shown in Table 2.3 [Nelson, 1990].

Table 2.3: Mineralogical composition of unhydrated Portland cement clinker.

Compound Name	Common Name	Chemical Composition	Weight Concentration (%)
Tricalcium silicate	Alite	$3CaO•SiO_2$	55-65
Dicalcium silicate	Belite	$2CaO•SiO_2$	15-25
Tricalcium aluminate	Aluminate	$3CaO•Al_2O_3$	8-14
Tetracalcium aluminoferrite	Ferrite	$4CaO•Al_2O_3•Fe_2O_3$	8-12

Cement slurry is made by mixing cement powder by mixing cement powder with water. The hydration process is an exothermic chemical reaction between the different compounds in cement when it comes in contact with water. As the cement sets and hardens, heat is generated. The cement has not only the ability to set in air but also underwater. Upon complete hydration, the two main hydration products are: calcium silicate hydrate (C-S-H) and calcium hydroxide ($Ca(OH)_2$) as shown in Table 2.4, and remains of unhydrated minerals, gypsum and minerals. However the main phase, C-S-H is not crystalline.

Table 2.4: Cement hydration products.

Hydrated Products	Chemical Formula	Concentration (wt.%)
Calcium Silicate Hydrate	$3CaO·2SiO_2·3H_2O$	50 - 70
Calcium Hydroxide	$Ca(OH)_2$	15 - 25
Ettringite	$Ca_6Al_2(SO_4)_3(OH)_{12}·26H_2O$	

C-S-H is the main binding phase and thus influences strength in hydrated cement [Taylor, 1997]. Cement is a porous material with highly alkaline (pH~13) pore solution (pore water),

depending on the water to cement ratio. The alkalinity maintains the $Ca(OH)_2$ in the cement matrix. Ettringite connects the different minerals during cement hydration.

The rate of hydration, the strength and the permeability of hydrated product depend primarily on the water to cement ratio (w/c), type of cement, its fineness, additives, temperature, and relative humidity curing conditions. Under ambient conditions, as the degrees of hydration increases the porosity and permeability of the cement decreases while the cement strength increases. The degree of hydration of cements with water to cement ratio between 0.3 and 0.6 does not change substantially after 28 days at ambient conditions [Taylor, 1997]. This point can be achieved in less number of days at higher temperature.

2.2.2 Classification of Portland Cement

Most standard wellbores use Portland cements and could have different formulations due to the wellbore conditions. They have been classified into 8 groups by the American Petroleum Institute in API RP-10B based on the degree of sulfate resistance and hydration rate [Recommended Practice For Testing Oil-Well Cements And Cement Additives, 1977]. In addition, other cement types are also developed in order to handle particular challenges such as high pressure high temperature (HPHT) and thermal conditions [Nelson and Guillot, 2006].

Additives are used in Portland cements to alter the performance of cements systems to enable successful cement placement, rapid strength development and low permeability that enables adequate zonal isolation over the life of the well. Cement additives have to be added to the base Portland cement to accommodate for the severe environmental conditions. Corrosive fluids, porous formation and over pressured formation fluids are also conditions where additives are useful. Presently, more than 100 additives are available within the following main groups [Nelson and Guillot, 2006]:

- Accelerators (chemicals that accelerate the setting process of the cement system)
- Retarders (chemicals that inhibit rapid setting of the cement system)
- Extenders (materials that lower the density of the cement system, reduce cement per unit volume, or both)
- Weighting agents (materials that increase the density of the cement system)
- Dispersants (chemicals that decrease the viscosity of the cement system)
- Fluid-loss control agents (materials that control fluid loss from the cement system)
- Lost circulation control agents (materials that control loss of cement slurry to the formation)
- Specialty additives (various additives, such as fibers, flexible particles and anti-foam agents)

Pozzolan, silica flour, polymer fiber and steel fiber are cement additives that can be used to prevent cement strength retrogression, limit dissolution of $Ca(OH)_2$, and prevent thermal fractures in wellbore cement. It is important to discuss response of a cement system to different additives, because response and performance may vary during various conditions. Cement-water ratio, additive concentration, temperature, pressure, mixing order, and mixing energy are conditions which may impact the performance of additives. In addition, physical and chemical properties of cement play an important role as well. Properties such as particle size, free alkali content, reactivity of hydrating phase, silicate and aluminate distribution, gypsum ratio, sulfate content, chemical nature, quantity, and specific surface area of initial hydration products are crucial for additive response. These influencing factors confirm the significance of laboratory tests prior to developing a cement system for use in the field [Nelson and Guillot, 2006].

2.2.3 Geopressured Geothermal Wellbore Cement

Geothermal wells are usually completed in similar manner as oil and gas wells. The problem with using conventional Portland cement in cementing geopressured geothermal wellbores has been their poor performance in providing zonal isolation and mechanically supporting the well casings and in mitigating the pipe's corrosion in very harsh reservoir conditions [Sugama, 2006]. Therefore, it is important to consider both the physical and chemical properties of the formation when designing the cement slurry.

To minimize heat loss, insulating cement sheaths is desirable in geothermal wells. However insulating cement has a detrimental effect on the casing. They place additional stress on the casing resulting from increasing casing temperature. Thermal conductivity has been determined to be a function of density of the cement as displayed in Figure 2.2.

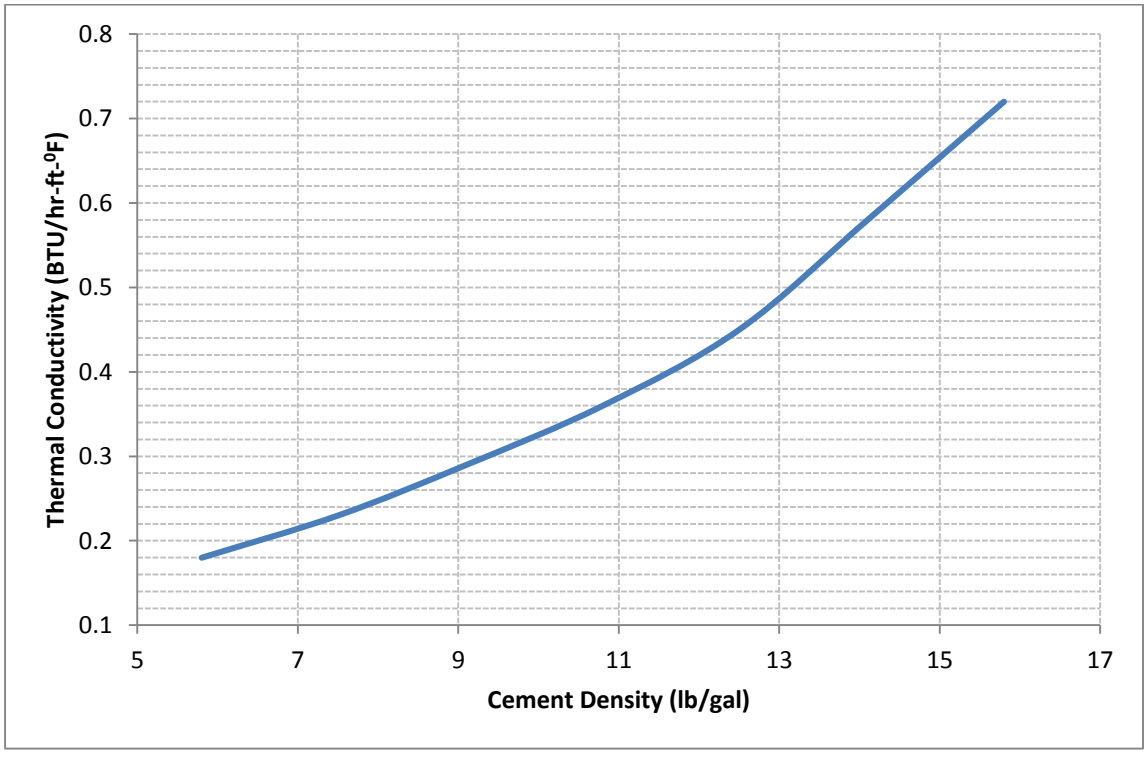

Figure 2.2: Cement density/thermal conductivity relationship [Data replotted from Nelson and Guillot, 2006].

2.2.4 Cement Failure

Several pieces of wellbore construction may compromise cement sheath integrity. These will produce conduits for formation fluid to flow into other geological zones or up to surface, leaving the surrounding environment in danger for contamination, and rendering the well unsafe. The conduits created within the cement are often referred to as microannuli. Cement failures can occur at the cement-casing interface known as inner de-bonding, at the cement-formation interface known as outer bonding, or within the cement sheaths as a result of shear damage and radial cracking. Outer debonding can be caused by dissolution of cement due to exposure to corrosive fluid from the reservoir such as salt water and also due to cyclic loading of temperature and pressure. Figure 2.3 illustrates the possible pathways for formation fluids to migrate when cement sheath fails.

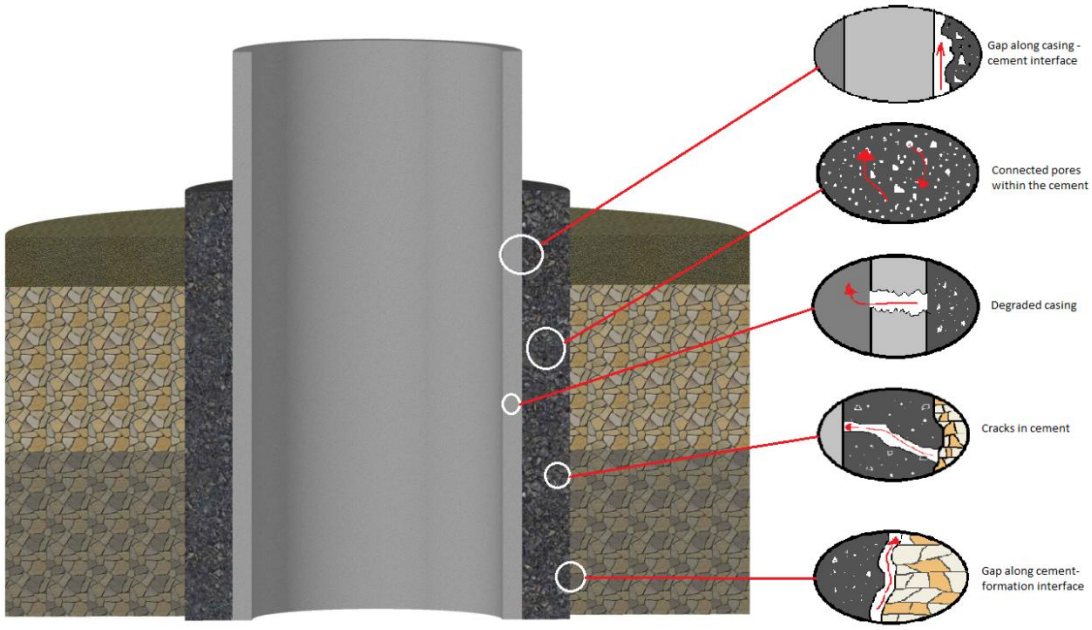

Figure 2.3: Well integrity depends on cement sheath integrity. Several formation fluid pathways are illustrated.

2.2.4.1 Cement Shrinkage

During exothermic hydration process of cement clinker, C-S-H gels form followed by precipitation of hexagonal $Ca(OH)_2$ (CH) plates (Figure 2.4). As the hydration process continues, the gel structure binds the different compounds in cement making a set solid structure, which gives cement its beneficial properties [Bois et al., 2009]. The resulting set cement net volume becomes less than the initial water and cement powder. This occurs because the absolute density of the set cement is greater than the water and cement powder, which is the cause of volumetric shrinkage of cement. The hydration process of the silicate phase can be described as:

$2CaO{\cdot}3SiO_2 + 6H_2O \rightarrow 3CaO{\cdot}2SiO_2{\cdot}3H_2O + 3Ca(OH)_2$ formation of C-S-H and $Ca(OH)_2$ from C_3S

$4CaO{\cdot}2SiO_2 + 4H_2O \rightarrow 3CaO{\cdot}2SiO_2{\cdot}3H_2O + 3Ca(OH)_2$ hydration of C_2S forms C-S-H and $Ca(OH)_2$

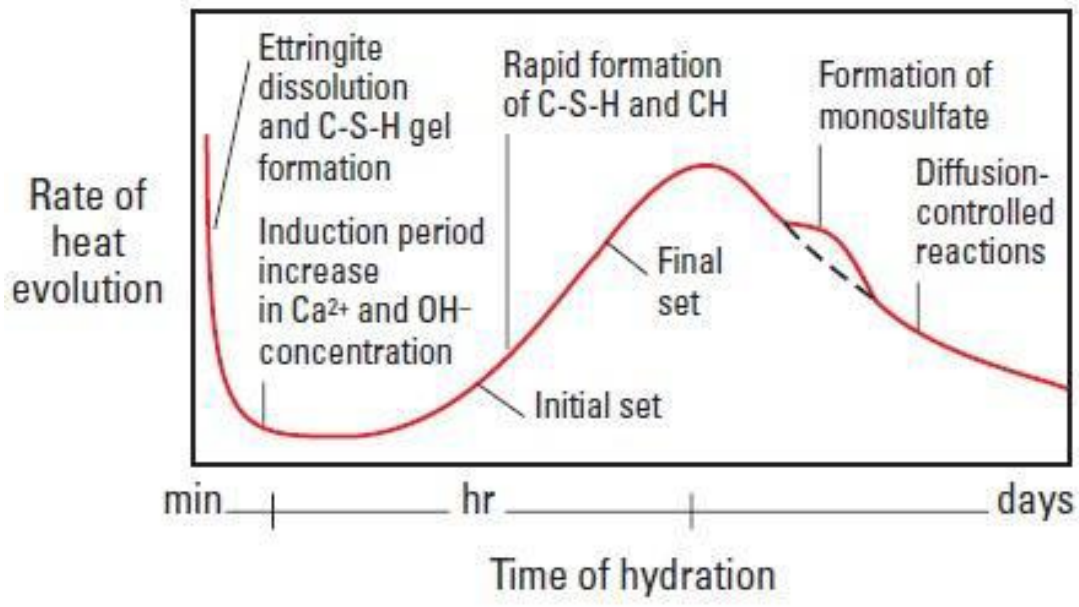

Figure 2.4: Heat evolution during hydration of Portland cement [Nelson and Guillot, 2006].

2.2.4.2 Thermal Degradation of Cement

The strength of hydrated cement increases with age and on reaching maximum strength remains constant under ambient conditions as C-S-H is an excellent binding material at temperatures below 110^0C (230^0F). Strength retrogression occur in cements at temperatures above 110^0C as C-S-H phase in hydrated cement converts to alpha dicalcium silicate hydrate {(Ca2(HSiO4)(OH)} phase [Taylor, 1997]. The greater the temperature increase, the quicker the rate of transformation of C-S-H. This changes the structure of the hydrated cement leading to increased porosity, permeability, and lowered compressive strength [Taylor, 1997]. In addition, ettringite formation in high temperature environments can cause cement sheath to crack [Taylor, 1997; Tian et. al, 2000].

The real problem lies in the great increase of permeability as it makes the cement susceptible to corrosive formation fluids [Nelson and Guillot, 2006; Sugama, 2006]. Experimental studies by Yalkinkaya et al. shows that exposure of cement fracture to CO_2 rich brine will increase the porosity and widen the fracture [Yalcinkaya et al., 2011, Yalcinkaya, 2010; Yalcinkaya et al., 2011, Ozyurtkan and Radonjic, 2014].

2.2.4.3 Cement Behavior in Low pH Environment

Portland cement is subject to chemical attack from formation fluids and substances injected from the surface into reservoirs. Over time, these saline geothermal fluids are damaging to cement integrity especially those containing carbondioxide, CO_2 and sulfates, $(SO_4)^{2-}$ like the Camerina Sand A. As a result of thermodynamic inequilibrium, pore fluid in cement, strongly alkaline at pH ~ 13 chemically interacts with the slightly acidic formation brine. $(SO_4)^{2-}$ in formation brine react with cement to form ettringite and gypsum ($CaSO_4{\cdot}2H_2O$) which have greater bulk volume than the cement pores and hydration products [Taylor, 1997; Tian et. al,

2000]. This induces stress that causes cement fracturing due to crystal growth. Possible chemical reaction that could result in gypsum formation are listed below:

$MgSO_4 + Ca(OH)_2(s) + 2H_2O \rightarrow CaSO_4 \cdot 2H_2O + Mg(OH)_2$ formation of gypsum from magnesium sulfate dissolved in brine

$Na_2SO_4 + Ca(OH)_2(s) + 2H_2O \rightarrow CaSO_4 \cdot 2H_2O + 2NaOH$ gypsum is formed from sodium sulfate in brine

In addition when cements are exposed to acidic formation brines, outward diffusion of Na^+, K^+, and OH^- from the cement matrix can occur as a result of the concentration gradient between the surrounding formation brine and the cement pore water. The diffusion of Na^+, K^+, and OH^- out of the cement matrix lowers the pH of the cement causing $Ca(OH)_2$ to dissolve. CO_2 combines with water to form carbonic acid which in turn dissolves Ca out of cement matrix to form calcium carbonate ($CaCO_3$) [Klutchko, 2007, Duguid and Scherer, 2010, and Duguid et. al, 2011]. The chemical equations below describe dissolution of Ca^{2+} from the $Ca(OH)_2$.

$CO_2 + H_2O \leftrightarrow H_2CO_3$ carbonic acid is formed

$2H_2CO_3 + Ca(OH)_2(s) \rightarrow Ca^{2+}(aq) + 2HCO_3^- + 2OH^-(aq)$ $Ca(OH)_2$ is dissolved

$Ca^{2+}(aq) + HCO_3^- + OH\text{-}(aq) \rightarrow CaCO_3(s) + H_2O$ $CaCO_3$ is formed

As the $Ca(OH)_2$ in the cement matrix is used up, the pH of the cement drops causing the $CaCO_3$ to start dissolving. This leaves the C-S-H with no defense causing the decalcification of C-S-H into Ca^{2+}, OH^-, and amorphous silica gel [Yang et al., 2012; Jain et al., 2009].

$H^+(aq) + CaCO_3(s) \rightarrow Ca^{2+}(aq) + HCO_3^-(aq)$ $CaCO_3$ is dissolved

$3CaO \cdot 2SiO_2 \cdot 3H_2O(s) \rightarrow Ca^{2+}(aq) + OH^-(aq) + SiO2(am)$ declassification of C-S-H

The leaching process increases the porosity and modifies the microstructure of the cement matrix leading to increase in permeability and inability to protect the wellbore casing from corrosion.

2.2.5 Thermal Cycling of Cement

Production/injection wells, Steam Assisted Gravity Drainage (SAGD), or gas producing wells, are some of the well situations that can causes thermal cycling of the cement as the downhole materials are exposed to severe fluctuations. The steel casing for example is influenced by pressure and temperature. When high temperature is applied, the steel casing will expand. The same scenario would occur if the pressure is increased. Stop of production, or injection of relatively cold water, would change the downhole conditions, therefore the casing contracts, causing challenges to maintain isolating annular cement sheath. The expansion and contraction induce stress regimes on the cement sheath, making it to crack in addition to debonding [Nelson and Guillot, 2006]. Heat of hydration could be an affecting factor as well, during hydration the cement system produce heat, this can be unfavorable for the binding of casing and cement causing a potential microannuli.

A production stop due to an intervention could drastically change the temperature gradient across the wellbore. This may be injection of various fluids, acid fracturing, hot oiling, perforation and etc. [Bosma et al., 1999]. Furthermore, a production well may after some years be changed to a pure injection well, or to an alternating injection production well of water or gas. But this may not have been considered initially, when the well was planned and constructed [Vignes et al., 2008]. The design criteria may then, not be sufficient in order to withstand severe temperature changes. All these mentioned parameters during the life time of a well, affect the

temperature ranges the well is exposed to, making thermal cycling of cement interesting to investigate.

In SAGD application, hot steam is generally injected downhole to reduce the viscosity of hydrocarbons in the form of heavy oil, making the heavy oil exploitable. By means of gravity, heavy oil with lowered viscosity is able to flow to the production casing below the injected steam. Heat is considerably lower during production, making the temperature difference between injection and production to be several hundred degrees. High temperature differences undoubtedly expose downhole equipment to extreme circumstances making material selection critical [Taoutaou et al., 2010]. To date, several cement systems have been developed by service companies for such applications in addition to casing and casing connections with premium steel grading [Lepper, 1998]. However, laboratory verifications of the materials in representative downhole conditions are still missing.

2.2.6 Nature of Cement in Wellbore Design

In the reservoir at the production end, the cement is in direct contact with the saline brine at temperatures above 110^0C (Figure 2.5, bottom left). This would cause cement retrogression and leaching of calcium (Ca) and silicon (Si) from the cement and formation of gypsum and ettringite. At the injection point for the reservoir fluid (Figure 2.5, bottom right), the casing cement interface experiences a lower temperature compared to the rock-cement interface due to the heat exchange in the wellbore. This causes a differential temperature across the cement. Cyclic thermal loading of geothermal cement during in-situ heat harvesting can potentially cause thermal fracturing and durability issues.

The combination of leaching, crystal growth, strength retrogression and thermal cracks would cause an increase in permeability, loss of strength, and inability to protect the casing from

corrosion consequently leading to lack of zonal isolation. Therefore, with temperature, pressure and formation fluid changing with location and depth, Portland cement have to be customized for different wellbores. It is important to address cement durability at different environments and provide solutions to prevent cement degradation over time.

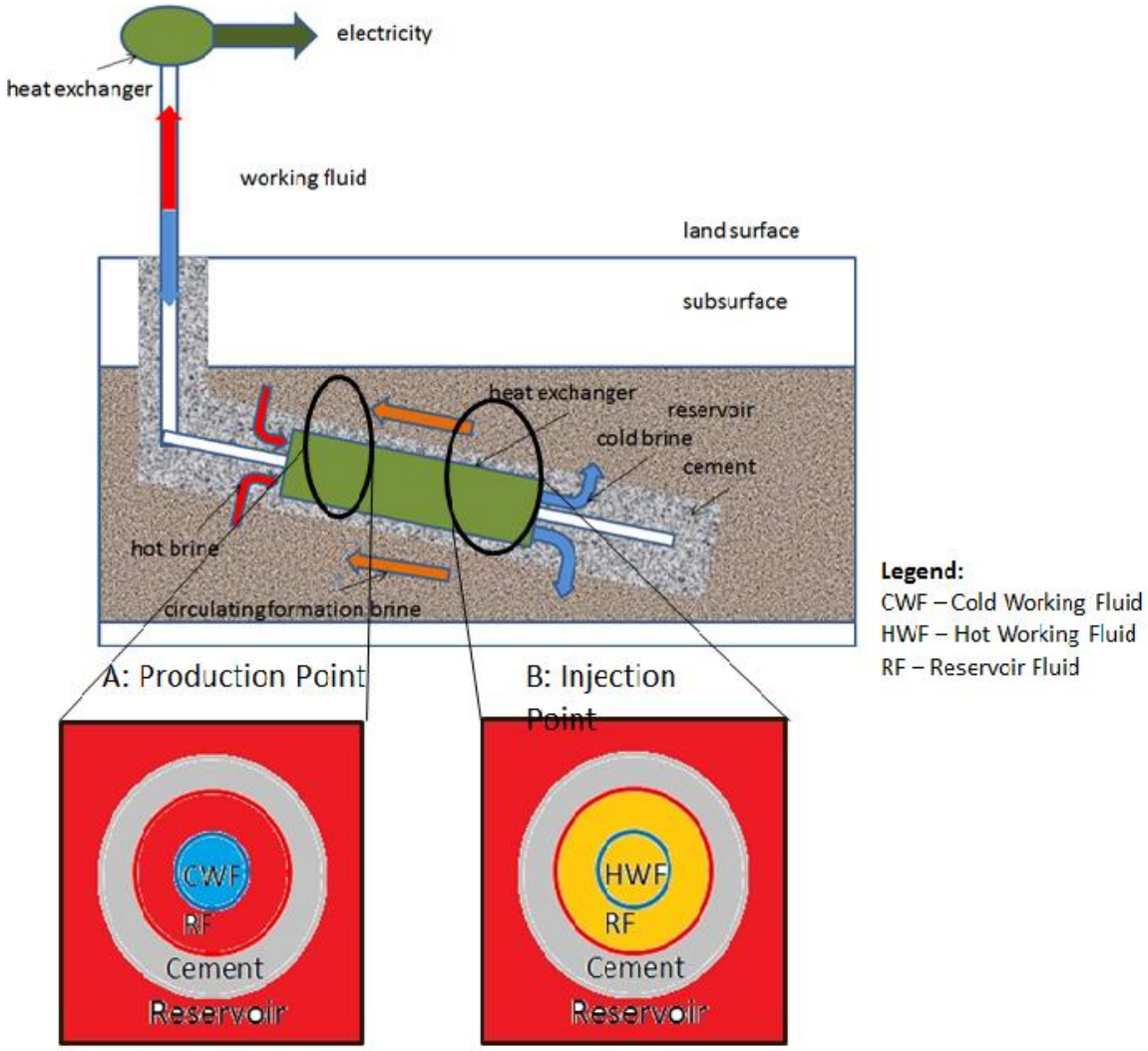

Figure 2.5: Lateral section of proposed wellbore system. Bottom: cross-sections of the wellbore at production point for reservoir fluid (L), and injection point.

2.3 Experimental Cement Design

In order for the wellbore cement to function properly in a wide range of working conditions, additives are often added to neat cement. This study evaluates the effect of pozzolan,

silica flour, polymer fiber and steel fiber on neat cement under the conditions of the proposed zero mass withdrawal wellbore. The chemical additives (Figure 2.6) were added to Portland cement slurry to counteract and curb strength retrogression, by changing cement hydration products into chemically more stable phases, with favorable Ca to Si ratio. The selected additives were also chosen because of their potential to prevent thermal micro fracturing of cement sheath.

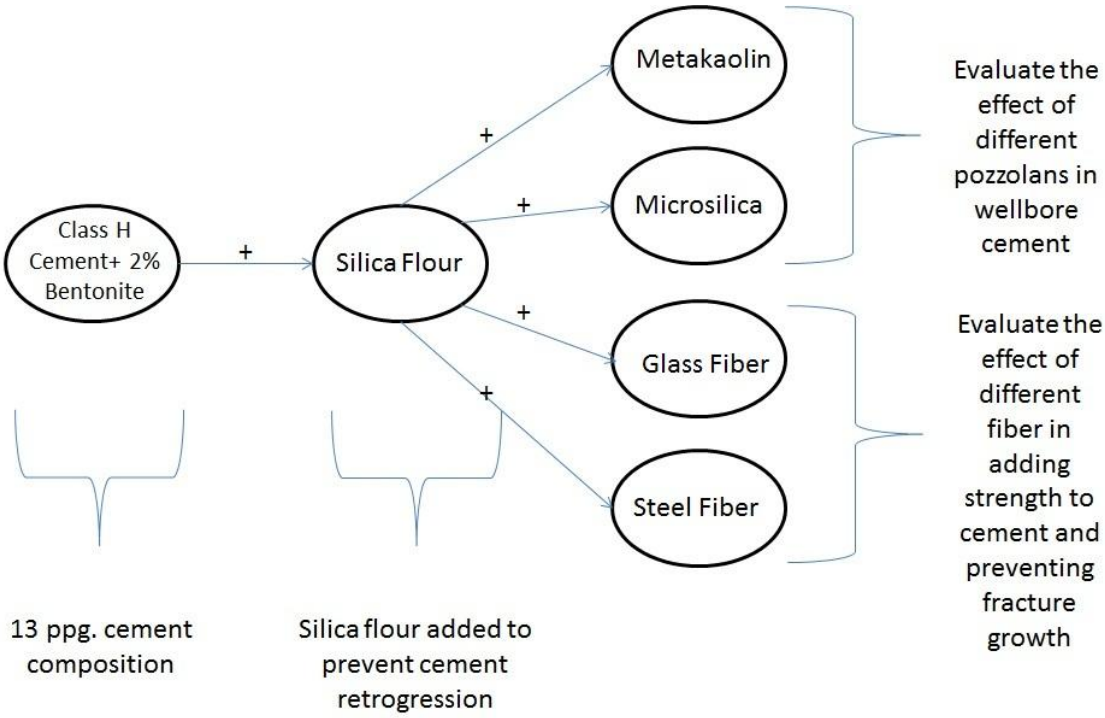

Figure 2.6: Proposed cement design for geopressured geothermal design.

2.3.1 Pozzolans

Pozzolans are very fine, siliceous or aluminous materials which react with $Ca(OH)_2$ to form C-S-H in the presence of water [Ambroise, 1985; Sabir et. al, 2001; Vejmelkova, 2012].

$SiO_2(am) + Ca(OH)_2(s) \rightarrow 3CaO{\cdot}2SiO_2{\cdot}3H_2O(s)$ formation of C-S-H from pozzolan and $Ca(OH)_2$

The use of pozzolan improves the durability and strength of cements as a result of the additional C-S-H and removal of $Ca(OH)_2$ which can be dissolved by reservoir brine. Metakaolin, a calcined clay would be used as an admixture. The advantages of using metakaolin as an admixture are higher strength, increased durability, reduced heat of hydration, reduced sulfate attack, and low cost [Ambroise, 1985, Vejmelková et al., 2012]. A 1:1 bulk volume of metakaolin to cement ratio is used for mixing resulting in 10 % metakaolin by weight of cement (BWOC) in 13.2 lb/gal cement slurries [Nelson, 1990]. Condensed silica fune (silica sand) with particle sizes ranging from 0.1μm to 0.5μm can also be used as a pozzolan in cements. Silica sand is fine, pure, and highly reactive leading to high compressive strength in low density slurries. Concentration of microsilica is 15 % BWOC [Nelson and Guillot, 2006].

2.3.2 Silica Flour

Silica in the form of α-quartz is used in cement to prevent strength retrogression [Nelson and Guillot, 2006; Gaurina-Medimurec et al., 1994]. At high temperatures, silica reacts and prevents formation of $Ca_2(HSiO_4)(OH)$. Addition of quartz to cement is done by adding 35 to 40% quartz BWOC. This raise the Ca to Si ratio in cement to ~1 which is associated with C-S-H properties required for low permeability.

2.3.3 Glass Polymer Fibers

To modify the elasticity of the cement, glass polymer fibers will be added to the cement. Addition of glass polymer fibers makes cement less brittle, thereby preventing thermal fractures in cement when subjected to thermal cyclic loading [Nelson, 1990]. The glass polymer fibers can restrain crack opening and crack growth by effectively bridging across the micro cracks. Glass fiber are usually high in quartz and sodium oxide.

2.3.4 Steel Fibers

Steel fibers are used to increase compressive and tensile strengths of cement. They are also used to reduce cement segregation which is very beneficial in depleted formations against loss circulation of cement [Nelson, 1990; Gaurina-Medimurec et al., 1994; Shyrock, 1984]. A study by Berndt et al. on effects of fibers on cements shows that the tensile strength of Class G cement and 40% silica flour mix was improved with the addition of steel fibers [Berndt and Philippacoulos, 2002]. The study also concluded that significant improvement are seen when round steel fibers are used than in straight and crimpled stainless steel fiber as a result of higher fiber count and aspect ratio.

CHAPTER 3: EXPERIMENTAL SETUP AND PROCEDURES

3.1 Experimental Program

To study the behavior of cement in proposed wellbore [Feng et al.,2011; Feng, 2012, Feng et al, 2015], a batch experiment was conducted using four different class H cement slurry design (Table 3.1). Four cement slurry designs with cement additives to accommodate for the severe environmental conditions were investigated and compared with neat cement slurry. In addition, cores from all five cement designs was cured in in water bath at ambient conditions as control samples.

Table 3.1: Mix proportions of cements by mass. Slurries were mixed using water to solid ratio of 0.87 to achieve slurry density of 13.1 lb/gal. For cement with additives, there was 35% weight replacement of cement with silica flour.

Design	Neat Cement	Steel Fiber Cement	Silica Sand Cement	Calcined Clay Cement	Glass Fiber Cement
Class H Cement	1	1	1	1	1
Bentonite	0.02	0.02	0.02	0.02	0.02
Silica Flour	-	0.35	0.35	0.35	0.35
Steel Fiber	-	0.02	-	-	-
Silica Sand	-	-	0.02	-	-
Calcined Clay	-	-	-	0.02	-
Glass Fiber	-	-	-	-	0.02
Water	0.87	1.17	1.17	1.17	1.17

All four cement slurry designs contain class H cement and silica flour. Fine metakaolin, silica sand, steel fiber, and polymer were added to the first, second, third and fourth sample respectively (Table 3.1). The calcined clay has a grain size ranging from 45 μm to 75 μm. The calcined clay and steel fiber have a size range of 5 μm and 400 μm respectively. The glass fiber has the biggest grain size of the additives with a range of 3-5 mm. Cement core samples were made according to the American Petroleum Institute (API) recommended practice [Recommended Practice for Testing Oil-Well Cements and Cement Additives, 1977].

The cement slurry was prepared by mixing Class H cement and distilled water at a water to solid ratio of 0.87. The mixing was done with a four liter, 3.75 horsepower Waring® blender. Bentonite and water was mixed first at 16,000 revolutions per minute (RPM). After five minutes, the rest of the material was added to the mixture in the blender and mixed at 20,000 RPM for the next 35 seconds. The cement slurry was poured into 7.63x2.54 cm. (3x1 in.) cylindrical brass molds. The wait on cement period was 24 hours after which the cement cores were de-molded and used in the experiments.

Hydrated cement cores were subjected to cycles of differential temperature of 50^0C with 100% relative humidity (RH) in experimental brine (Table 3.2) in temperature cycling/relative humidity (environmental) chamber. Each cycle took 12 hours with the temperature ramped from 40^0C to 90^0C and back to 40^0C (Figure 3.1). The experiment was limited by the boiling point of water, and that was why it was conducted at 90^0C rather than over 100^0C as reported in literature. After 100 cycles, poro-mechanical analysis and material characterization were done to evaluate the changes in the cement.

Table 3.2: Brine composition for experiment.

Salts	Amount mixed with 1L of distilled water
Sodium Chloride (NaCl)	32.19 g
Potassium Chloride (KCl)	0.454 g
Magnesium Chloride ($MgCl_2$)	0.991

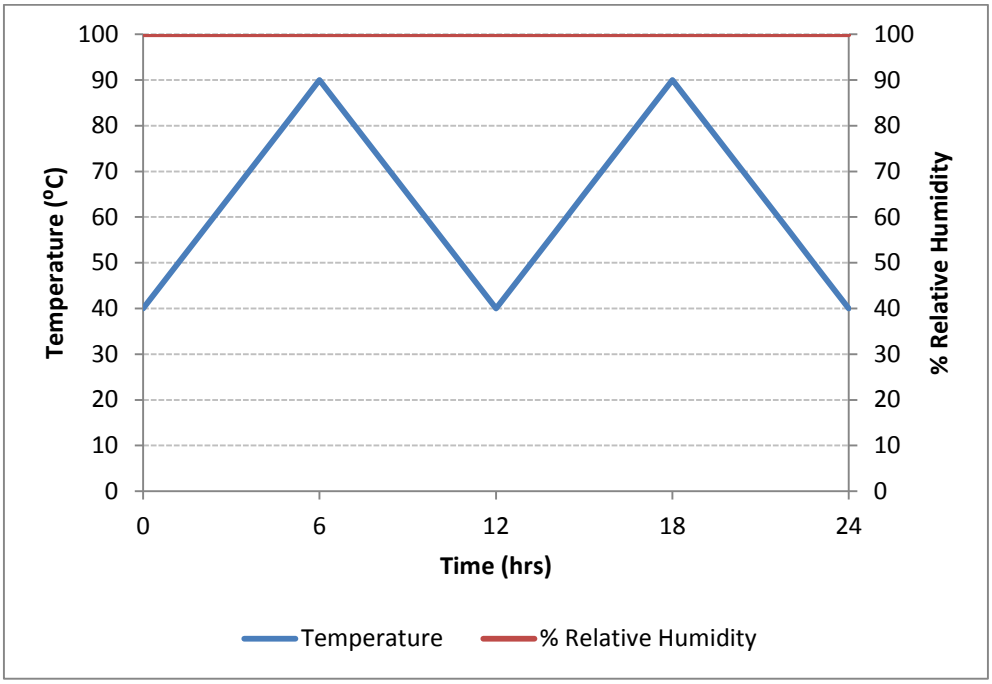

Figure 3.1: Profile showing conditions applied to two cycles in the TCL experiment. Analysis was conducted after 100 of this cycle.

3.2 Temperature Cycling/Relative Humidity Chamber

The temperature cycling/relative humidity chamber (environmental chamber) was used for testing the cement under geothermal conditions. The environmental chamber was used to subject the cement cores to thermal cycle loading as described in section 3.1 (Figure 3.2). The environmental chamber is an ESPEC EGNL12-4CAL model with a lower and upper with a lower and upper temperature limit of -40 ^{0}C and 180 ^{0}C respectively.

<table>
<tr><td>  </td><td>  </td></tr>
<tr><td>A. Cement slurry was mixed in this 1 liter Waring® blender using distilled water, class H cement and additives as listed in Table 3.1.</td><td>B. Cement slurry was poured into lubricated brass mould and allowed to harden for 24 hours before been removed and used in experiment.</td></tr>
<tr><td> 
</td><td>  </td></tr>
<tr><td>C. Core of hardened cement slurry used in experiment.</td><td>D. Cement samples from same design placed in heat resistant carbon fiber bowl containing experimental brine.</td></tr>
<tr><td>  </td><td>E. Carbon fiber bowl containing samples was covered with aluminium foil to prevent evaporation and placed in environmental chamber for thermal cycling loading using a differential temperature of 50^0C at 100% RH.</td></tr>
</table>

Figure 3.2: Sample and experimental preparation.

3.3 Inductively Coupled Plasma-Optical Emission Spectroscopy (ICP-OES)

The brines in which the different cement designs were cured and a control brine were analyzed using ICP to determine if there was any leaching from the cement matrix or precipitation of salt crystals in the cement matrix as a result of thermal cycle loading. ICP-OES was used to determine the amount of cations contents present in the brine. Each element present in the fluid emits energy at specific wavelengths peculiar to its atomic structure. To determine what elements are present in the brine, the emitted wavelength and their intensities are analyzed relative to a reference standard. Brine samples were analyzed at LSU Department of Plant, Environmental and Soil Sciences using a Spectro Ciros^{CCD} ICP-OES machine.

3.4 Helium Gas Porosimetry

The porosity and density were determined on three cores from each sample design. This was accomplished by using a Ultragrain GrainVolume Porosimeter, UGV-200 from Core Laboratories. The UGV-200 utilizes Boyles Law helium gas expansion porosimetry. 10 cc of helium gas at a certain pressure is expanded into the cement cores. The final pressure occupied by the gas is then used to determine the grain volume (V_g) of the cement cores. The grain volume with the bulk volume (V_b) of the core is then used to determine the porosity of the cement cores. The grain volume and the dry weight (W) of the cores are also used to determine the grain density ($\boldsymbol{\rho}_g$) of the cement cores. The bulk volumes of the cores are calculated using the core dimensions taken with a caliper while the weight of the cores are measured using a mass balance.

$$\emptyset = \frac{V_b - V_g}{V_b} \quad (1)$$

$$\rho_g = \frac{V_b}{W} \quad (2)$$

The samples were dried in an oven to remove all the pore water to allow for accurate measurement of the pore spaces. The weights of the samples were measured before and through the drying process as a way to monitor the level of pore water present in the sample. To prevent thermal cracking in the drying process, the temperature was ramped from ambient to 105^0C over the first 24 hours and then left constant till the end of the drying process.

3.5 Liquid Pressure-Pulse Decay Permeameter

Laboratory measurement of low permeability media such as cement to water is usually a technical challenge. The liquid pressure-pulse decay permeameter (PDPL) is a tool capable of quantifying the permeability changes in cement. A PDPL model CFS-200 was used to determine the permeability of the cement cores as it employs a transient technique to measure cement permeability to water. Cores are placed in a pressure vessel that allows hydrostatic confining pressures as high as 680 bar (10000 psi), maximum back pressure of 400 bar (6000 psi) and resist temperatures to ~ 150^0C. The permeability was reported in nanoDarcy (nD) (equivalent to 10^{-21} m^2).

Compared to conventional (steady state) methods, the liquid pressure-pulse decay permeameter cuts down the long time required to stabilize water fluxes from days or weeks to hours. This is very critical as cement permeability could change due to leaching or hydration during the time required in steady state methods [Scherer et al., 2006; Boulin et al., 2006]. Under in-situ confining pressure, water permeability is a more accurate measure for the flow of reservoir brine than gas permeability due to the difference in the compressibility of gas and water, where permeability is a function of pressure decay through the core over time [Jones, 1997; Chen and Stagg, 1984]. Pressure differential across the cores were plotted against time on a semi-log plot with the slope used in permeability calculation (Equations 1-3).

$$k = \frac{\emptyset \mu m C_f}{\alpha^2} \quad (3)$$

$$m = \frac{\log(^{\Delta P_2}/_{\Delta P_1})}{t_2 - t_1} \quad (4)$$

$$\alpha tan\alpha = \frac{Vp}{Vb} \quad (5)$$

where $\emptyset$ = p$orosity$ of the core, μ = water v$iscosity$, C_f = water c$ompressibilty$, V_p = Core pore p$ressure$, V_b = core bulk v$olume$

3.6 Mercury Intrusion Porosimetry (MIP)

MIP is typically used to determine the pore size in cement as shown in Figure 3.3. It's raw data are incremental and cumulative intrusion of mercury into the pores (both in ml/g), the capillary pressure and pore throat size. The pore throat diameters in hydrated cement are typically in the nanometer to micrometer range with the capillary pores ranging between 10 to 100 nm.

MIP was used to confirm the porosity measurement and determine pore size distribution [Hewlett, 1998]. Mercury is injected into cement with the injection pressure gradually increased to intrude even smaller pore throats with a lower limit of 0.001μm. MIP assumes that all the pores are connected [Abell et al., 1999] and cement samples are required to be dried prior to MIP analysis to remove surface water. Besides its disadvantages, it is a quick technique that has been in application for many years; therefore, it was employed to see the effect of acidic brine on the pore throat size distribution.

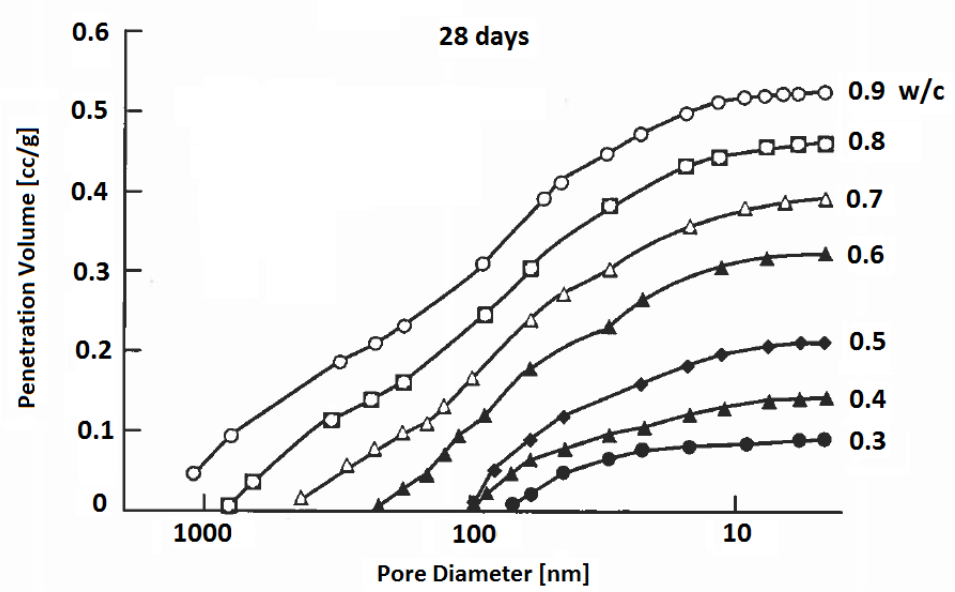

Figure 3.3: Figure from MIP data showing the relationship between porosity (penetrated volume of cement) and pore throat diameter of cement sheath with different water to cement [Mehta and Monteiro, 2006]. As the w/c increases, the porosity increases and so does the amount of larger pores.

3.7 Compressive Strength Tester

A Model 4207D Compressive Strength Testers was used to measure the unconfined maximum compressive strength of hydrated cement cubes after experiments according to the API RP 10A [Recommended Practice For Testing Oil-Well Cements And Cement Additives, 1977]. The result from this analysis was used to establish the relationship between cement's pore connectivity and their compressive strength. In addition, it was used to gauge the strength of the different cement designs under the proposed reservoir and wellbore condition.

3.8 Thermogravimetric Analysis

Thermogravimetric Analysis (TGA) was used to determine the weight change of $Ca(OH)_2$ within each cement sample design. TGA measures physical and chemical changes of materials as a function of increasing temperature with constant heating rate. TGA was used to determine the mass loss in $Ca(OH)_2$, one of two main hydration product of cement. TA

Instruments SDT Q600 Simultaneous DSC/TGA was used from ambient to 1500°C (2732°F). The following parameters were used in the analysis: purge gas of nitrogen at a flow rate of 0.0035 ft^3/min (100 ml/min); alumina pans; equilibration at 104°F (40°C) for 10 minutes; heating rate of 41°F/min (5°C/min) from 104°F (40°C) to 392°F (200°C), followed by a heating rate of 50°F/min (10°C/min) up to 1832°F (1000°C).

3.9 Scanning Electron Microscopy (SEM) and Energy Dispersive Spectroscopy

SEM was used to generate high-resolutions micrographs of the nano-structures of hydrated cements before and after exposure to high temperature and differential temperature. It was also used to show spatial variation in chemical compositions of hydrated cements along with EDS using spot and area chemical analysis. Hydrated Samples were polished and coated with platinum to achieve improved imaging quality. The SEM micrographs were captured using a FEI Quanta 3D FEG dual beam SEM/FIB system at the Material Characterization Center in the Department of Mechanical Engineering, Louisiana State University.

SEM uses a focused beam of high energy electron to generate signals at the surface of solid objects. The signals reveal information about texture, crystalline structure, and orientation of the mineral composition of the object. SEM produces 2-dimensional micrographs of high magnification with resolutions as high as 1 nm. Kinetic energy from accelerated electrons is dissipated as a variety of signals by electron-sample interactions when the incident electrons are decelerated in the solid object. The interaction of the electrons with the object generates secondary electrons, backscattered electrons and X-rays [Goldstein et al., 2003]. These signals are detected and processed to provide information about the object's topography and composition. The secondary electron imaging is most valuable for providing information about the morphology and topography of the object. The reflection of backscattered electrons from the

object is a function of the atomic number of the elements on the surface and is most useful for depicting contrast in chemical composition across the sample [Swapp, 2013]. When combined with EDS, SEM can be used to determine chemical present in areas of interest. EDS uses the characteristic x-rays emitted by the object to determine the elemental composition of the object.

CHAPTER 4: RESULTS

This chapter reports the results from thermal cycle loading experiment in order from the experimental methodology in Chapter 3. For petrophysical and mechanical analysis, measurements were taken on both control cores (cement cores cured at ambient conditions) and cores from thermal cycle loading experiment.

4.1 Chemical Monitoring During and Post Thermal Cycle Loading

The pH and temperature of a control sample of brine placed at ambient condition was taken after 45 days. The pH was measured to be 8.92 at 22.3^{0}C. Higher pH was measured in the experimental brines during the thermal cycle experiment. Table 4.1 shows the pH at respective temperature of the brines after 90 cycles of thermal loading.

Table 4.1: pH measurement of control brine after 45 days at ambient conditions and brine samples containing all the different samples after 90 thermal loading cycles. Higher pH measured in the brine containing cement samples suggests dissolution of cement matrix during thermal loading experiment.

Cement Sample in Brine	Brine pH	Brine Temperature [^{0}C]	Brine pH	Brine Temperature [^{0}C]
Control Brine	8.92	22.3	8.86	24.3
Neat Cement	11.27	61.3	12.67	24.3
Steel Fiber	11.54	41.6	12.20	24.5
Silica Sand	11.36	43.3	12.08	24.4
Calcined Clay	11.42	45.8	12.25	24.3
Glass Fiber	11.25	45.9	12.07	24.3

Figure 4.1 presents a plot of the analysis of the brine for common ions present in cement after 120 thermal cycles. Inductively Coupled Plasma (ICP) mass spectrometry was used to detect the concentration of Al^{3+}, Ca^{2+}, Fe^{3+}, Mg^{2+} and Si^{4+}. There was an increase in the ions for all brines compared to the original brine except for Mg^{2+} which decreased. The most notable

change was observed in the concentration of Ca^{2+} with almost three orders of magnitude increase. Brines in contact with cement cores containing steel fiber and glass fiber cements had the highest concentration of Ca^{2+} with 1200 mg/L and 1202 mg/L respectively. Of significant importance is also the concentration of Si^{4+} observed. Brine with glass fiber cement had a Si^{4+} concentration of 18 mg/L which is the highest amongst the entire samples.

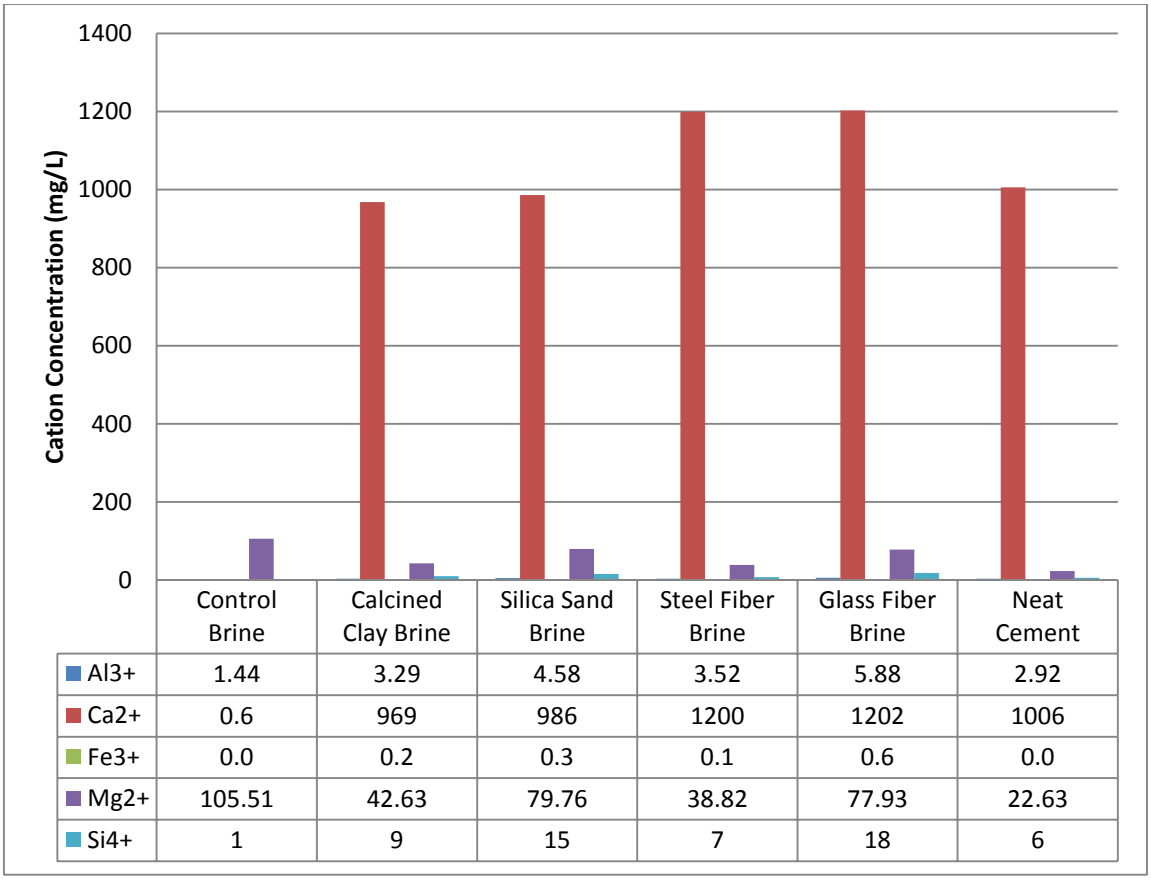

	Control Brine	Calcined Clay Brine	Silica Sand Brine	Steel Fiber Brine	Glass Fiber Brine	Neat Cement
Al3+	1.44	3.29	4.58	3.52	5.88	2.92
Ca2+	0.6	969	986	1200	1202	1006
Fe3+	0.0	0.2	0.3	0.1	0.6	0.0
Mg2+	105.51	42.63	79.76	38.82	77.93	22.63
Si4+	1	9	15	7	18	6

Figure 4.1: Inductively Coupled Plasma cation identification in brine containing different cement design after 100 cycles of thermal loading. Increase in $Ca^{2+}$and Si^{4+} in all the brines compared to the original brine indicate dissolution of main minerals in hydrated cement.

4.2 Porosity Measurement from Porosimeter

Porosity and grain density was determined on cores from each sample design using a Helium Boyle's Law Porosimeter. The cores were approximately 5.08 cm. (2 in.) length and 2.54

cm. (1 in.) in diameter. The average porosity of the control samples are presented in Table 4.2. The average porosity of the neat cement was the lowest at 52.74% while the highest average porosity of 56.38% was measured in the glass fiber cement design. Steel fiber cements, silica sand cements, and calcined clay cements have average porosities of 53.47%, 54.88%, and 55.06% respectively.

Table 4.2: Average grain density and average porosity of control cement designs. The samples were cured in water bath at ambient conditions (~25°C).

Cement Sample	Average Grain Density (g/cc)	Porosity (%)
Neat Cement	2.214±0.012	52.74±0.16
Steel Fiber	2.270±0.011	53.47±0.24
Silica Sand	2.272±0.001	54.88±1.23
Calcined Clay	2.271±0.005	55.06±1.23
Glass Fiber	2.315±0.047	56.38±0.57

Table 4.3 summarizes the porosity of the four designs after 100 cycles. Steel cement design exhibit the lowest porosity with an average of 54.36%. The highest porosity average was 56.97% measured in glass fiber cement cores. A cement core containing glass fiber had the highest porosity at 58.34% while a cement core containing steel fiber had the least porosity of 51.03%. It should be noted that the density of the steel cement core with the least porosity was lower compared to the rest of the cores. The porosities of all the cores were very similar with a range of 7.31% and a smaller range of 2.18% if the 51.03% porosity measured in the cement core containing steel sample was not considered.

Table 4.3: Average grain density and average porosity of cement sample designs after 100 thermal cycle loading. Glass fiber cement design had the highest porosity while steel fiber cement design had the lowest porosity.

Cement Sample	Average Density (g/cc)	Average Porosity (%)
Neat Cement	2.343±0.015	57.41±0.608
Steel Fiber	2.363±0.072	54.36±2.895
Silica Sand	2.382±0.018	56.56±0.421
Calcined Clay	2.400±0.034	55.63±0.238
Glass Fiber	2.397±0.041	56.97±1.328

4.3 Permeability of Cement Cores Post Experiment

Permeability measurement was carried out on wet cement cores, both on the control samples and samples that have undergone thermal cycle loading in the environmental chamber after 100 cycles using a liquid pulse pressure decay permeameter. Permeability in all cement designs are close in the $10^{-18} – 10^{-19}$ m^2 ($10^2 – 10^3$ nD) range. Glass fiber cements had the lowest permeability with an average of 1.384×10^{-20} m^2 (14.03 nD) and 9.120×10^{-20} m^2 (92.41 nD) from the control samples and the TCL samples respectively. Steel fiber cements had the highest average permeability from the control samples at 2.442×10^{-19} m^2 (247.4 nD) with silica sand cement very close behind. From the thermal loaded samples, silica sand had the highest permeability at 3.914×10^{-19} m^2 (396.6 nD) for the TCL experiment. The neat cement design had a lower permeability compared to the steel fiber cement design. Table 4.4 shows the average permeability value of each cement design for the control samples and TCL samples.

Table 4.4: Average permeability of control samples and samples after 100 thermal cycles. Silica sand cement design exhibit the highest permeability while glass fiber cement design has the least permeability for both control samples and thermal cycle samples.

Sample	Average Permeability (x 10-20 m^2) of Control Samples	Average Permeability (nD) of Control Samples	Average Permeability (x 10-20 m^2) after 100 Thermal Cycles	Average Permeability (nD) after 100 Thermal Cycles
Neat Cement	15.83±1.21	160.4±12.3	30.12±2.85	305.2±28.9
Steel Fiber	24.42±0.95	247.4±9.6	25.43±2.32	257.7±23.5
Silica Sand	22.53±0.42	228.3±4.3	39.14±3.98	396.6±40.3
Calcined Clay	20.46± 1.13	207.3±11.5	28.59±5.92	289.7±60.0
Glass Fiber	1.384± 0.424	14.03±4.29	5.499±6.442	55.72±21.09

4.4 Mercury Intrusion Porosimetry (MIP) Result

MIP was done on samples from all cement design from thermal loaded samples. The result show pore throat radius distribution between 0.0025 μm and 2.5 μm. The porosity according to MIP of the thermal cycled samples are listed in Table 4.5. With MIP, the calcined clay cement sample had the lowest porosity at 50.81% while the silica sand cement sample had the highest at 58.71%. The porosity of the neat cement sample, the steel fiber cement sample and the glass fiber cement sample are 51.41%, 54.18%, and 55.24% respectively. This result clearly shows complete repeatability and agreement with porosity data from helium gas Porosimetry.

Table 4.5: Calculated porosity from Mercury Intrusion Porosity of the samples after 100 thermal cycles.

Cement Sample	MIP Porosity (%)
Neat Cement	51.41
Steel Fiber	54.18
Silica Sand	58.71
Calcined Clay	50.81
Glass Fiber	55.24

Figure 4.2 shows that the wide range of pore throat diameter can be further divided into three categories: 0.0025 μm to 0.01 μm, 0.01 μm to 0.1 μm, and 0.1 μm to 1 μm. In all the cement designs, there are similar amounts of pores with diameter between 0.01 μm and 0.1 μm. The difference in porosity of the cement designs after 100 thermal cycles can be observed in the really small pores of 0.0025 μm to 0.01 μm and the large pores with porosity of 0.1 μm to 1 μm. The neat cement has the lowest amount of the smaller pores (Figure 4.3) and the highest amount of the larger pores (Figure 4.4).

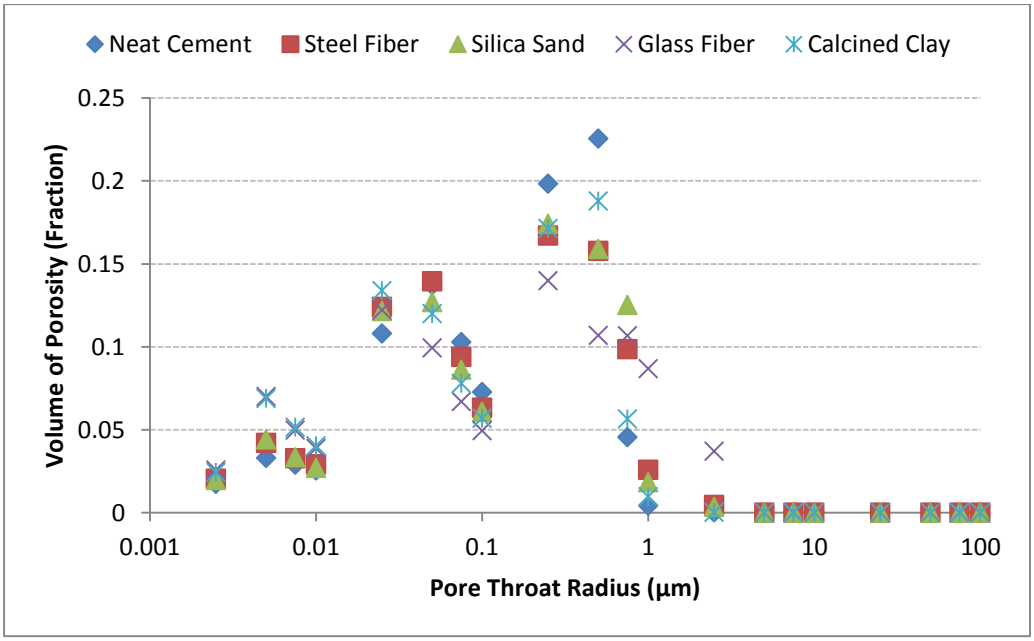

Figure 4.2: Pore throat size distribution of samples from thermal cycle loading experiment. MIP data indicates there are three categories.

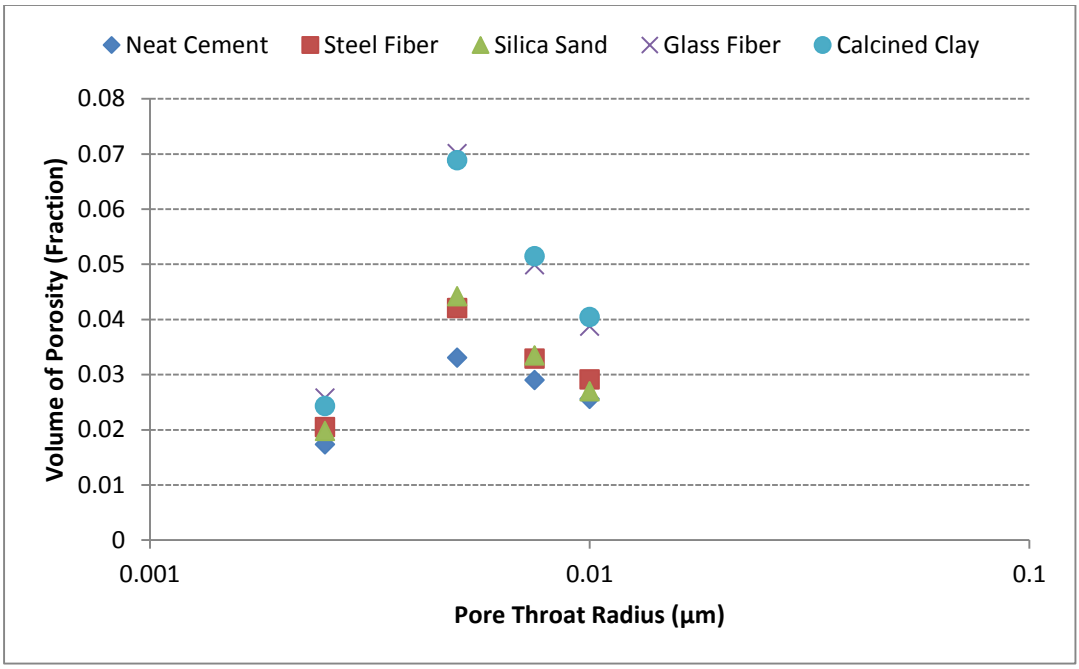

Figure 4.3: Pore throat size distribution between 0.0025 µm and 0.01 for TCL experiment. Sample of the neat cement design have the smallest amount of pores with this pore size distribution.

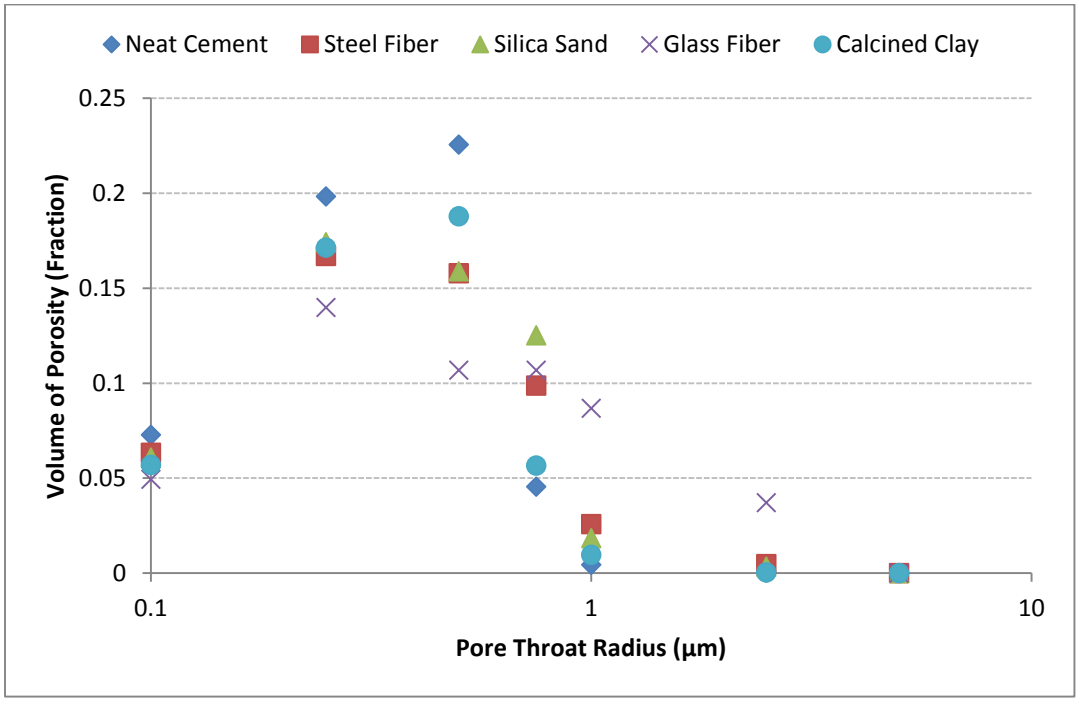

Figure 4.4: Pore throat size distribution between 0.0025 µm and 0.01 µm. Sample of the neat cement design have the smallest amount of pores with this pore size distribution.

4.5 Unconfined Compressive Strength Analysis

A Model 4207D Compressive Strength Tester was used to determine the unconfined maximum compressive strength of hydrated cement cores after 100 thermal loading cycles according to the API RP 10A [Recommended Practice For Testing Oil-Well Cements And Cement Additives, 1977]. This was done in order to quantify the effect of thermal cycle loading on the strength of the cement. The Compressive Strength Tester measures the maximum force (F_{max}) required to compress the cement core. The maximum force is divided by the cross sectional area (A) of the cement core to derive the compressive strength (σ). Two cores from each design were tested for strength.

$$\sigma = \frac{F_{max}}{A} \qquad (3)$$

Compressive strength was also measured on core samples from cement designs cured in water bath (Table 4.6). The compressive strength of the control cement cores were significantly greater than those measured in the thermal cycle loaded core samples for all the designs. Neat cement cores had the highest compressive strength of 7.936 MPa. This was significantly greater than what was measured in the rest of the designs.

Table 4.6: Average compressive strength for control samples. The compressive strength for each sample death was greater than those undergoing thermal cycle loading.

Cement Design	Average Compressive Strength [MPa]	Average Compressive Strength [psi]
Neat Cement	7.936±2.284	1151±331
Steel Fiber	3.968±0.683	575.5±99.0
Silica Sand	3.015±1.189	437.4±172.0
Calcined Clay	3.415±1.179	495.3±171.1
Glass Fiber	4.232±0.211	613.7±30.5

The compressive strength of the steel fiber, silica sand, calcined clay, and glass fiber cement samples are 3.968 MPa, 3.015 MPa, 3.415 MPa, and 4.232 MPa respectively.

A summary of the results for the samples subjected to 100 thermal cycles is presented in Table 4.7. The average compressive strength of the cement designs with neat cement, steel fibers, silica sand, calcined clay, and glass fibers are 2.822 MPa (~410 psi), 3.034 MPa (~440 psi), 2.879 MPa (~418 psi), 2.794 MPa (~405 psi) and 1.989 MPa (~289 psi) respectively.

Table 4.7: Average compressive strength of the cement designs after 100 thermal cycles. Cement designs with steel fibers exhibit the most compressive strength while cement designs with glass fibers have the least compressive strength.

Cement Design	Average Compressive Strength [MPa]	Average Compressive Strength [psi]
Neat Cement	2.822±1.144	409.6±166.1
Steel Fiber	3.034±0.539	440.1±78.09
Silica Sand	2.879±1.333	417.6±193.4
Calcined Clay	2.794±1.081	405.3±156.8
Glass Fiber	1.989±0.919	289.0±132.8

4.6 Phase Change Evaluation

TGA was run on the cement samples after 100 thermal loading cycles to quantify phase changes in the cement composition as a result of thermal cycle loading. Two analyses were conducted on each cement design using sample from the outer region of the core which was in direct contact with the brine and sample from the interior of the core with limited contact to no contact with the fluid. This was done to see if there is a difference across the core due to contact with the brine. Neat, steel fiber, calcined clay, and glass fiber cements cores had more $Ca(OH)_2$ on the inside than on the surface which was in contact with the brine. Silica sand cement core had the opposite result. There was more $Ca(OH)_2$ on the surface than inside in the core.

Figure 4.5 shows comparison of the TGA from the outer region and interior of the neat cement core after 100 thermal cycles. The peak at 421.25^{0}C is for $Ca(OH)_2$. From the outer region of the core, weight loss of 2.664% at the $Ca(OH)_2$ peak indicates approximately 11% $Ca(OH)_2$ exist on the outer region of the neat cement. On the interior region of the neat cement core, weight loss of 3.233% was measured at the 421.25^{0}C peak which indicates approximately 13% $Ca(OH)_2$ exist on the interior of the neat cement. This result means more $Ca(OH)_2$ exist on the interior of the neat cement core as a result of thermal cycle loading.

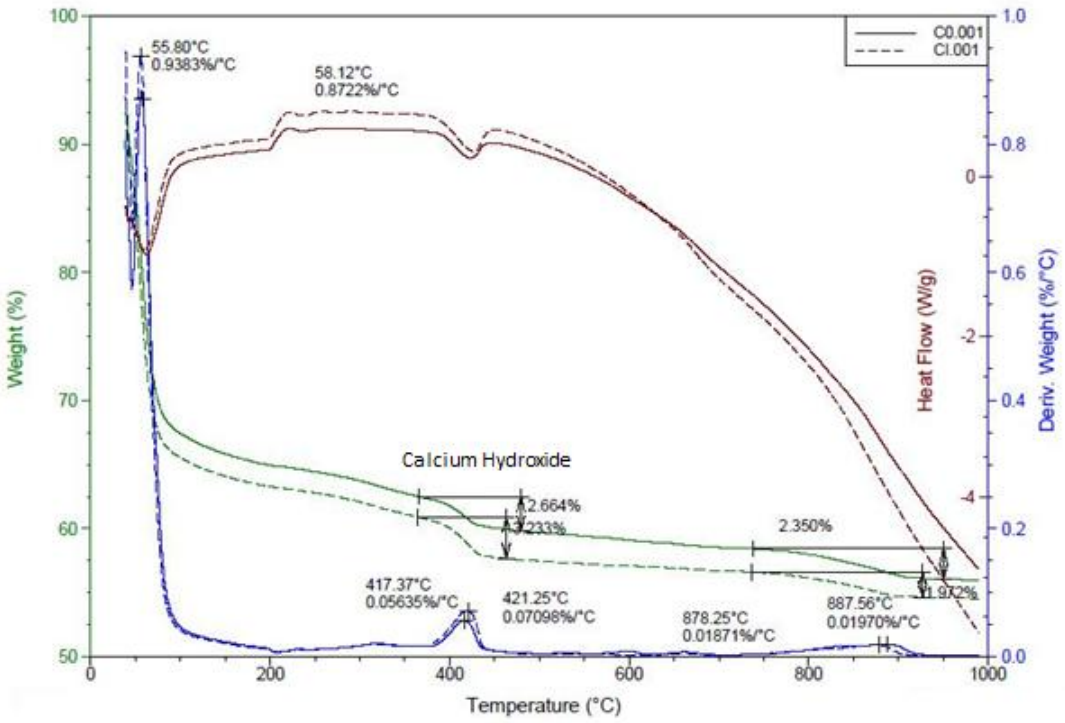

Figure 4.5: Plot of TGA comparison of the outer region and interior region of a neat cement core after 100 thermal cycles. Hashed lines were used to represent from interior the cement core while bold lines were used for the outer region sample. The green line depicts weight percentage lost while the blue line is the endothermal peaks (°C) of the weight percentage lost per unit of heat. From the outside of the core, weight loss of 2.664% was measured at the 421.25^{0}C peak which means approximately 11% $Ca(OH)_2$ exist on the outer region of the neat cement. On the interior region of the neat cement core, weight loss of 3.233% was measured at the 421.25^{0}C peak which indicates approximately 13% $Ca(OH)_2$ exist on the interior region of the neat cement core.

Steel cement samples (Figure 4.6) showed similar results to that of neat cement. TGA showed more $Ca(OH)_2$ exist on the interior region than the outer region of the steel cement core. Weight loss of 1.698% was observed at the $Ca(OH)_2$ peak corresponding to the presence of approximately 7% of $Ca(OH)_2$ on the interior region of the steel fiber. There was no significant weight loss on the outside of the core.

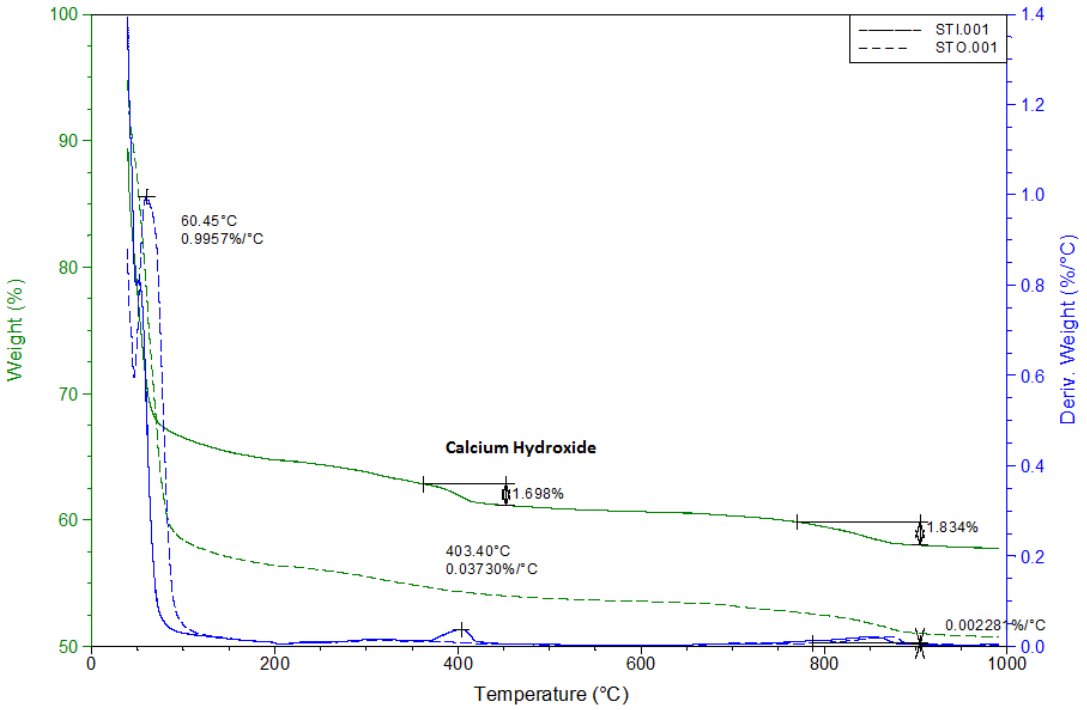

Figure 4.6: TGA plot showing comparison in steel cement after 100 thermal cycles. Hashed lines represent result from outer region of the cement core while bold lines were used for the interior region of the core. The green line depicts weight percentage lost while the blue line is the endothermal peaks (°C) of the weight percentage lost per unit of heat. The peak at 403.40^0C is for $Ca(OH)_2$. The $Ca(OH)_2$ peak showed a weight loss of 1.698% which indicates a presence of 7% $Ca(OH)_2$ on the interior region of the core. No $Ca(OH)_2$ was observed on the outer region of the steel cement as there was insignificant weight loss in the 403.40^0C.

Figure 4.7 compares the phase changes along the surface of the silica sand cement cores and the interior of the silica sand cement cores after 100 thermal loading cycles. The 1.347% weight loss at the 420^0C indicates that there is approximately 5% $Ca(OH)_2$ on the surface. This

is greater than the amount of $Ca(OH)_2$ observed on the interior of the silica sand cement. A weight loss of 0.7254% was observed in similar temperature region, meaning only 3% $Ca(OH)_2$ remains on the interior region of the silica sand cement.

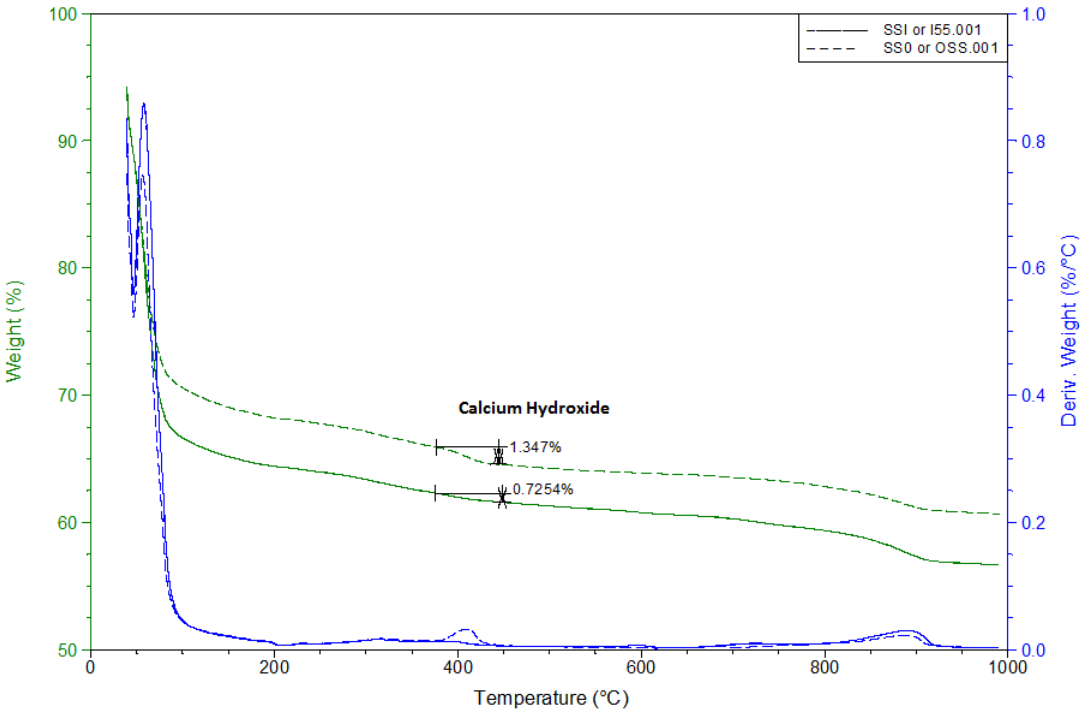

Figure 4.7: TGA plot comparing chemical changes on the surface of silica sand cement core to the interior of the core after 100 thermal loading cycles. Hashed lines represent result from outer region of the cement core while bold lines were used for the interior region of the core. The green line depicts weight percentage lost while the blue line is the endothermal peaks (°C) of the weight percentage lost per unit of heat. $Ca(OH)_2$ peak is at approximately 420^0C. The weight loss of 1.347% was observed on the surface of a silica sand cement core corresponding to the presence of approximately 5% $Ca(OH)_2$ on the surface of the core. The weight loss on the interior region of the same core was 0.7254% indicating 3% of $Ca(OH)_2$ remained.

TGA on samples from the interior region and outer region of a calcined clay core after 100 thermal cycles indicate higher amount of $Ca(OH)_2$ was removed from the outside of the calcined clay core than on the inside. A weight loss of 1.825% was measured on the sample from the surface of the calcined clay compared to 1.106% on the sample from the interior region of the

calcined clay core (Figure 4.8). This corresponds to almost a 3 % change in the amount of $Ca(OH)_2$ present across the core.

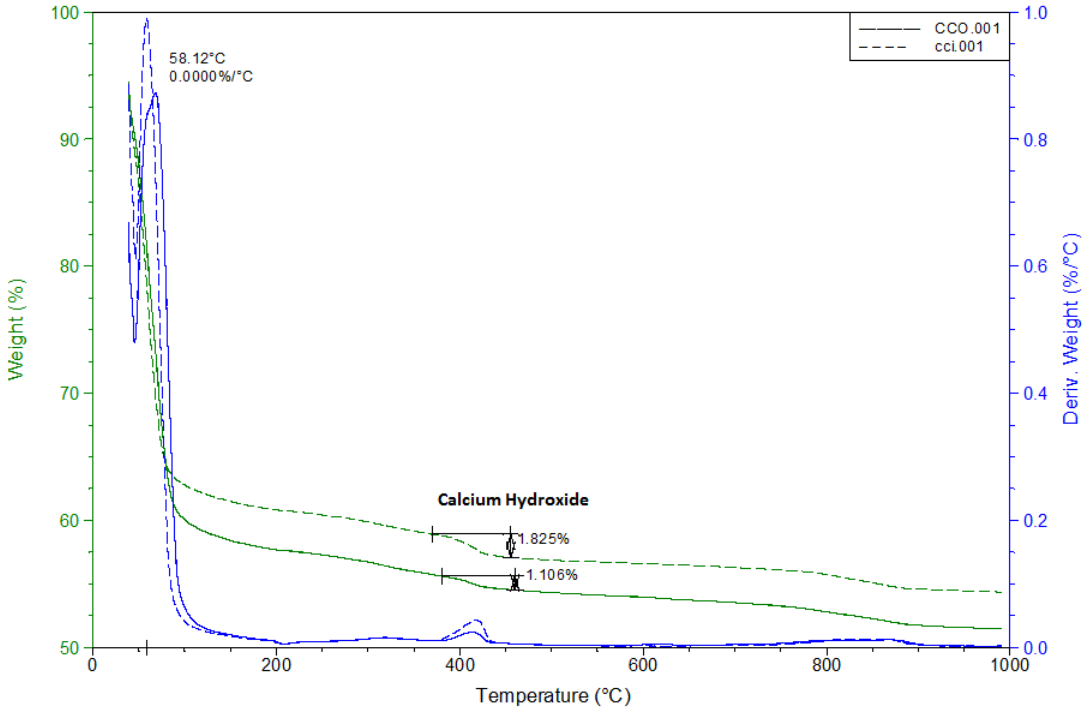

Figure 4.8: TGA plot comparing chemical changes on the surface of calcined clay cement core to the inside of the core after 100 thermal loading cycles. Hashed lines represent result from inside the cement core while bold lines were used for the sample from the surface of the core. The green line depicts weight percentage lost while the blue line is the endothermal peaks (^{0}C) of the weight percentage lost per unit of heat. $Ca(OH)_2$ peak is at approximately 420^{o}C. The weight loss of 1.825% was observed on the surface of a silica sand cement core corresponding to the presence of approximately 7% $Ca(OH)_2$ on the surface of the core. The weight loss on the inside of the same core was 1.106% indicating approximately 4% of $Ca(OH)_2$ remained.

Figure 4.9 depicts the result of TGA on the glass fiber cement core. Higher amount of $Ca(OH)_2$ was measured on the interior of the core than on the surface of the core. At 419^{o}C which is the $Ca(OH)_2$ peak, 1.934% was the weight loss measured on sample from the surface of the glass fiber core while a weight loss of 0.6903% was measured on the sample from the interior region of the glass fiber core. This means that approximately 8% and 3% of the original 25%

$Ca(OH)_2$ present remained from the interior region and outer region of the glass fiber cement core respectively.

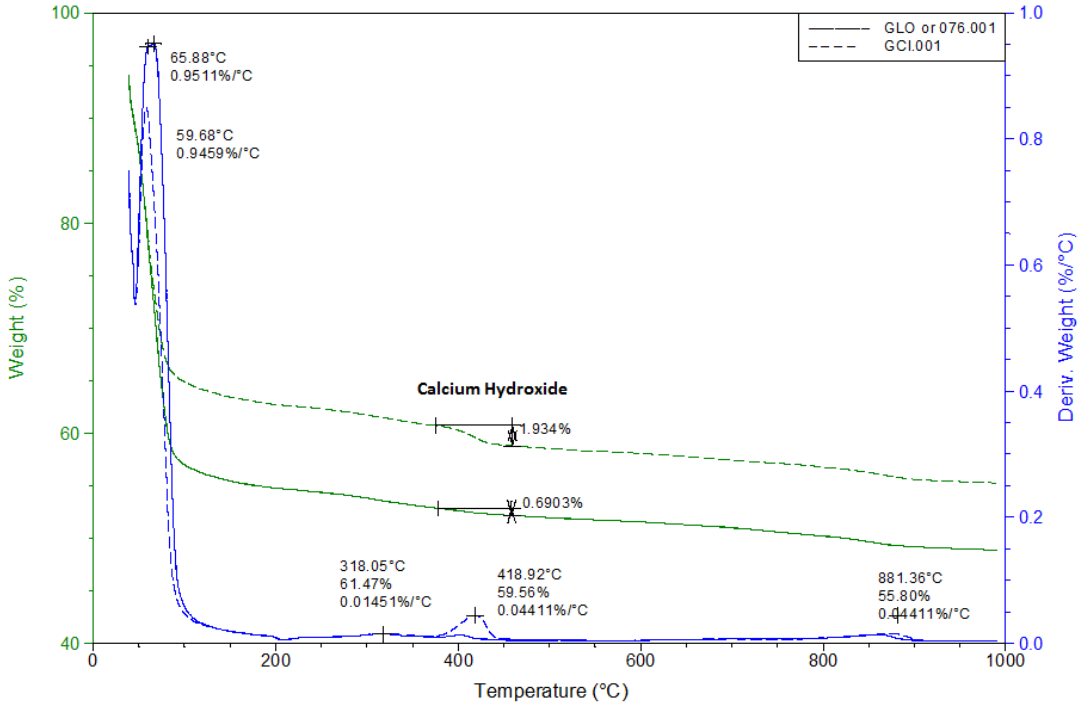

Figure 4.9: TGA plot showing comparison in glass cement after 100 thermal cycles. Hashed lines represent result from the interior of the cement core while bold lines were used for the sample from the surface of the core. The green line depicts weight percentage lost while the blue line is the endothermal peaks (^{0}C) of the weight percentage lost per unit of heat. $Ca(OH)_2$ peak is at approximately 420^{o}C. The weight loss of 1.934% was observed on the surface of a silica sand cement core corresponding to the presence of approximately 8% $Ca(OH)_2$ on the surface of the core. The weight loss on the interior of the same core was 0.6903% indicating approximately 3% of $Ca(OH)_2$ remained on the interior region of the core.

4.7 Microstructural Characterization

SEM was carried out to observe the microstructure of each cement design after 100 thermal cycles. SEM micrographs showed that the mineral composition of the designs were very similar. In the neat cement (Figure 4.10), C-S-H, $Ca(OH)_2$ and unhydrated cement clinker dominated the microstructure. The C-S-H observed in the neat cement clinker were very coarse,

large and fibrous. Figure 4.11 shows SEM and EDS analysis performed on steel fiber cement sample. The figure shows that the sample is dominated by quartz and C-S-H. The structure of this C-S-H is different from that observed in the neat cement sample, as they are less fibrous and porous. The steel fiber can be observed in low magnification micrographs because of their grain size. They are well dispersed through the cement matrix and appeared to have kept their shapes and sizes (outlined in Figure 4.11 D).

The composition of the silica sand cement was similar to the steel fiber cement (Figure 4.12). Large bulky quartz as well C-S-H were observed and confirmed in the SEM and EDS respectively. A closer look at the C-S-H shows that they have internal porosity. Na and Cl rich grains were present in the C-S-H structure (Figure 4.12 D). Figure 4.13 are SEM micrographs of the calcined clay cement. Seedlets were observed on the surface of the quartz in micrographs.

Figure 4.14 contain SEM micrographs of glass fiber cement sample. The C-S-H in this sample were very fibrous compared to the rest of the cement design. In addition, large blob of material that appear to be glassy in nature was observed in the SEM micrographs.

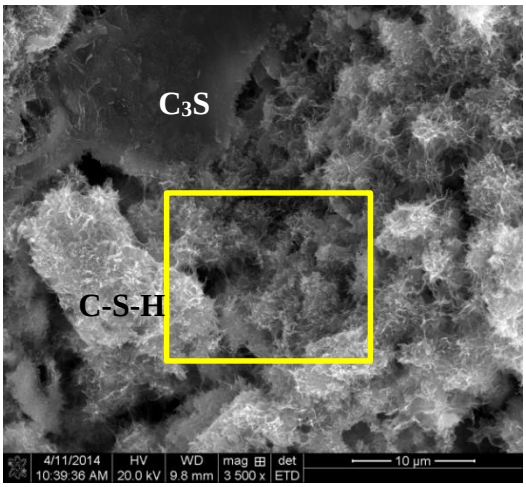

A. Low magnification SEM micrograph (mag: 3500x) of neat cement sample after 100 thermal cycles.

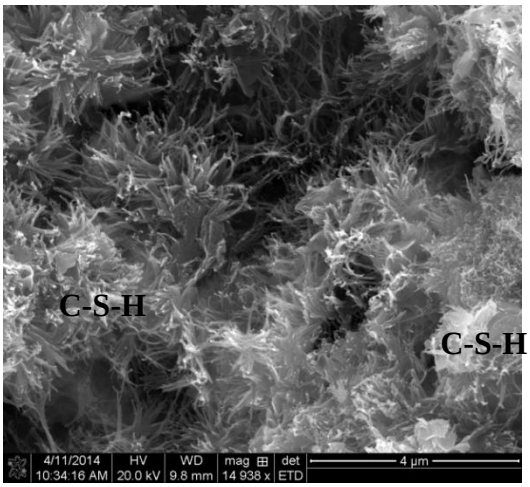

B. High magnification micrograph (mag: 15000x) of the C-S-H (rectangular area from Figure 4.13A). This micrograph shows that the C-S-H are coarse therefore have high porosity.

	Figure 4.10 C_3S Composition		Figure 4.10 C-S-H Composition	
Element	Weight %	Atomic %	Weight %	Atomic %
C	1.84	4.08	-	-
O	30.83	51.31	45.76	66.9
Mg	0	0	0.99	0.95
Al	0.11	0.11	1.16	1
Si	5.03	4.77	8.9	7.41
S	0.58	0.48	1.33	0.97
Ca	57.54	38.22	36.73	21.44
Fe	1.4	0.67	2.39	1

C. Area chemical composition result from EDS analysis of SEM micrographs result showing the presence of C_3S and C-S-H from Figures 4.13 A and 4.13 B. C_3S have a Ca/Si ratio of 3:1 while C-S-H have a Ca/Si ratio o2f 2:1

Figure 4.10: Low magnification SEM micrograph of neat cement sample after 100 thermal cycles shows that C-S-H in neat cement are coarse resulting in higher porosity when they are packed together.

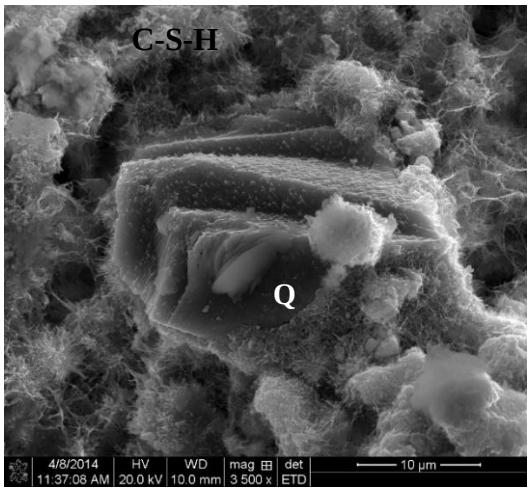

A. SEM micrograph (mag: 3500x) of cement sample with 35% silica flour BWOC and steel fiber. The dominant minerals are C-S-H, quartz, and unhydrated cement clinker.

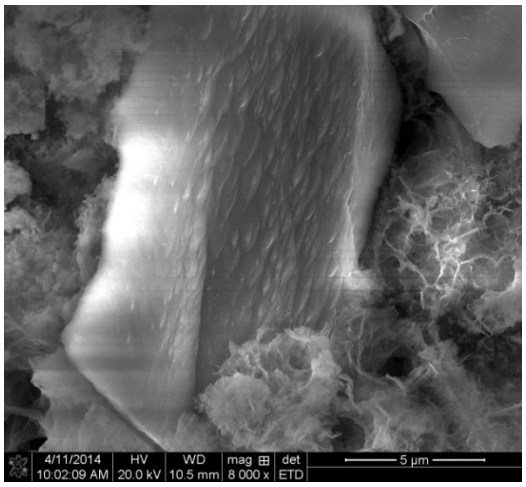

B. Higher magnification micrograph (mag: 8000x) of Figure 4.11A shows that although similar in structure, the C-S-H in the steel fiber cement design are much denser than those observed in the neat cement design.

	Area Composition of Q from Figure 4.11 A		Area Composition of C-S-H from Figure 4.11 A	
Element	Weight %	Atomic %	Weight %	Atomic %
C	2.64	5.54	3.11	6.09
O	37.55	59.16	41.24	60.69
Na	-	-	1.86	1.91
Mg	-	-	0.58	0.56
Al	0.01	0.01	0.63	0.55
Si	17.51	15.71	11.24	9.42
Mo	-	-	0.54	0.13
Cl	2.61	1.85	2.51	1.67
Ca	24.04	15.12	30.19	17.73
Fe	1.82	0.82	0.92	0.39

C. EDS analysis of the steel fiber cement sample from Figures 4.11 A and B. The quartz has a characteristic Si/O ratio of 1:2 while the C-S-H has a characteristics Ca/Si ratio of 2:1.

Figure 4.11: SEM micrographs and EDS of the steel fiber cement design after 100 thermal cycles. Quartz and C-S-H were the two dominant minerals present in the cement matrix.

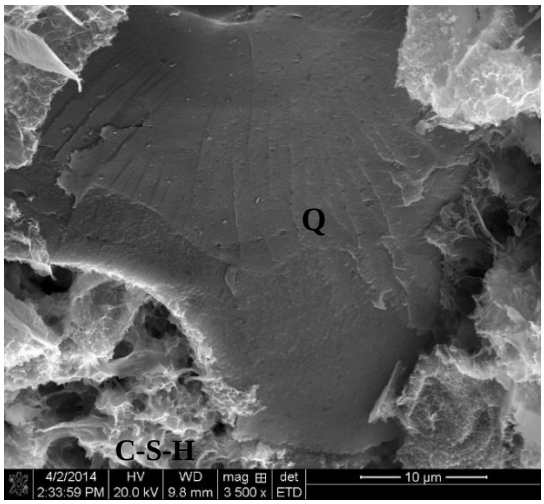

A. SEM micrograph (mag: 3500x) of cement sample from a silica sand design after 100 TCL. C-S-H and quartz were the two main minerals observed on the image.

	Area Composition of Q from Figure 4.12 A		Area Composition of C-S-H from Figure 4.12 A	
Element	Weight %	Atomic %	Weight %	Atomic %
C	-	-	2.27	6.1
O	44.81	59.96	24.71	49.92
Al	0.11	0.08	-	-
Si	50	38.11	6.01	6.91
Cl	0.42	0.25	4.75	4.33
Ca	2.58	1.38	32.44	26.16
Fe	-	-	3.98	2.3

B. EDS analysis of Figure 4.12A showing the presence of quartz mineral (Q) and C-S-H. The quartz has a characteristic Si/O ratio of 1:2 while the C-S-H has a characteristics Ca/Si ratio of 2:1.

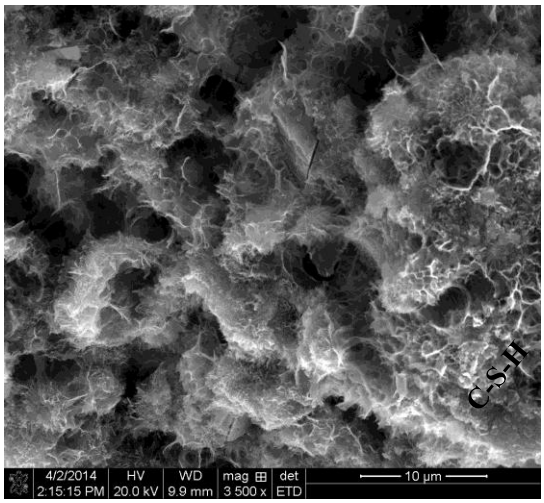

C. SEM micrograph (mag: 3500x) of cement sample from a silica sand design after 100 TCL depicting various shapes and sizes of C-S-H. Internal pores were observed on closer look at the C-S-H.

	Area Composition of C-S-H from Figure 4.12 C	
Element	Weight %	Atomic %
C	4.36	8.87
O	28.47	43.53
Na	10.19	10.84
Mg	0.35	0.35
Al	0.47	0.42
Si	11.17	9.73
Cl	12.44	8.58
Ca	27.42	16.74
Fe	0.92	0.4

D. EDS analysis of Figure 4.12C confirms that the minerals observed on the micrographs are C-S-H. High amount of Na and Cl element were observed in EDS analysis of the C-S-H.

Figure 4.12: SEM micrograph and EDS analysis of the silica sand cement design that have been subjected to at least 100 thermal cycles.

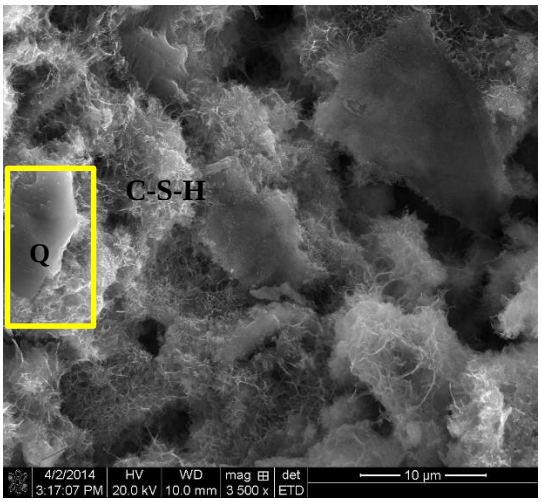

A. SEM micrograph (mag: 3500x) of calcined clay sample after 100 TCL.

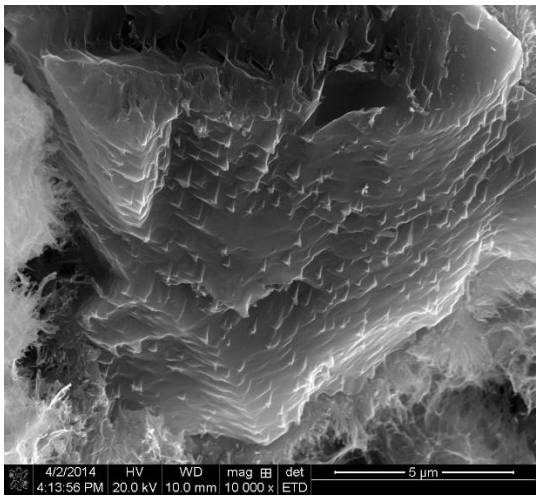

B. High magnification of box outline from Figure 4.13 A showing the structure of the quartz crystals (Q) with seedlets present on its surface in the calcined clay samples.

	Area Composition of Q from Figure 4.13 A		Area Composition of C-S-H from Figure 4.13 A	
Element	Weight %	Atomic %	Weight %	Atomic %
O	21.91	38.49	20.86	38.28
Na	-	-	1.51	1.93
Mg	-	-	0.67	0.8
Al	-	-	0.69	0.75
Si	52	52.04	14.36	15.01
P	0.09	0.08	0.01	0.01
Mo	-	-	0.24	0.07
S	-	-	0.95	0.87
Cl	-	-	4.22	3.5
Ca	6.96	4.88	50.56	37.03
Fe	2.75	1.38	2.27	1.19

C. EDS analysis showing chemical composition of C-S-H and quartz identified on the Figure 4.13. A. The quartz has a characteristic Si/O ratio of 1:2 while the C-S-H has a characteristics Ca/Si ratio of 2:1.

Figure 4.13: SEM and EDS analysis of cement sample from the calcined clay cement design after 100 thermal cycles.

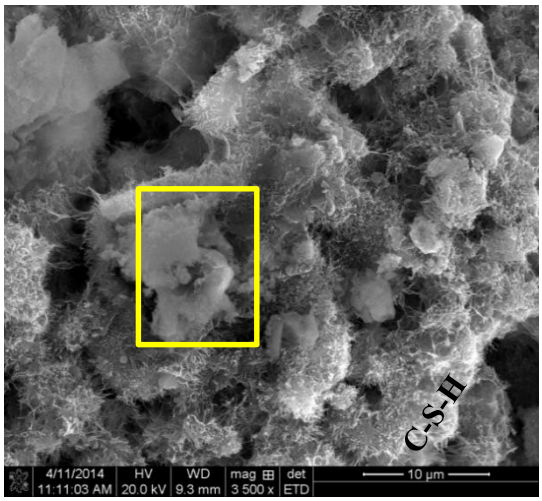

A. SEM micrograph (mag: 3500x) of cement sample from the glass fiber cement design. The rectangle outline depicts glass fibers dissolving in the cement matrix.

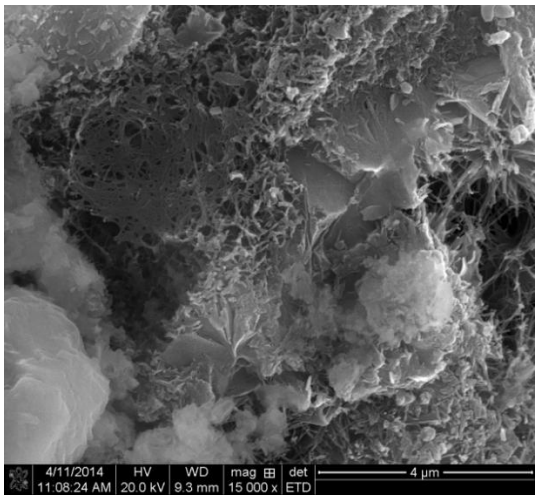

B. Higher magnification SEM micrograph (mag: 15000x) of glass fiber cement.

	Area Composition of C-S-H from Figure 4.4A3 A	
Element	Weight %	Atomic %
C	1.55	3.52
O	336	57.46
Na	0.18	0.21
Mg	1.11	1.24
Al	0.86	0.88
Si	4.81	4.68
S	0.29	0.25
Cl	3.65	2.82
Ca	36.17	24.69
Fe	4.94	2.42

C. EDS analysis showing chemical composition of C-S-H from 4.14 A. The C-S-H has a characteristics Ca/Si ratio of 2:1.

Figure 4.14: SEM micrographs and EDS analysis of sample from glass fiber cement design after 100 thermal cycles.

CHAPTER 5: DISCUSSION

Based on the observations reported in the results chapter, I focus on the most significant data and more importantly draw correlation between this data and as well as the concepts and observation reported in literature in this chapter.

5.1 pH Increase and Presence of Ca^{2+} in Brine

There is exchange of ions between the highly alkaline cement pore water and the brine when cement is in contact with brine. The brine is acidified by atmospheric CO_2, therefore it contains HCO^{3-} and CO_3^{2-} ions along with Na^+, K^+, Mg^{2+}, and Cl^- from the salt dissolved in the brine. Although the cement pore water is Na^+, K^+, and Mg^{2+} rich; their concentrations are much higher compared to those in the brine. This causes an inequilibrium leading to diffusion of those ions from the cement pore water into the brine. The outward diffusion of ions into the brine consequently reduces the pH of the cement pore water and initiate dissolution of $Ca(OH)_2$ from the cement sheath. As $Ca(OH)_2$ dissolves into the brine, the pH of the brine increases. The increase in the pH of the brines where cements were cured indicates that there is leaching of cement during the experiment.

Based on the ICP result, steel fiber cement design and glass fiber cement design seem to be the most impacted by the leaching as their brines have the highest concentration of Ca^{2+}, assuming there was no evaporation since the relative humidity in the chamber was kept at approximately 100%. Evaporation would typically increase the concentration of the ions in the brine. The cement cores are the only possible source for the higher Ca^{2+} that was observed in the cement brines since the control brine only showed traces of Ca^{2+}. This support the theory that $Ca(OH)_2$ is been dissolved from the cement matrix when in contact with low pH fluids.

5.2 Weight of $Ca(OH)_2$ in the Cement

The TGA results definitely confirm that $Ca(OH)_2$ is leached out of the cement and is the main source for the calcium in the brine. Potential source of Ca is the dominant phase in cement, C-S-H. However, this can't be concluded as it is hard to determine the amount and classification of the C-S-H since it does not have a defined crystal structure. Also, its thermal peak is at 56^0C, a point where moisture is been lost from the cement sample as it is been heated. Therefore any C-S-H weight loss measurement would have not been reliable. As $Ca(OH)_2$ from the cement is dissolved and leached out into solution, the porosity of the cement sheath should increase.

The TGA results suggest that the neat cement would fare less against leaching since it had the highest amount of $Ca(OH)_2$. The percentage of $Ca(OH)_2$ in all the cement designs should be similar assuming silica flour was not added to the cement designs with additives. The original weight of $Ca(OH)_2$ was smaller in the steel fiber, silica sand, calcined clay, and glass fiber cement designs compared to the neat cement design since cement has been substituted in with additives most of which was chemically reactive with cement. The reactions between silica flour and $Ca(OH)_2$ to form C-S-H has also been initiated from the high temperature of the experiment even though it is considered a slow process [Nelson and Guillot, 2006]. $Ca(OH)_2$ was higher in neat cement because it was not consumed to form C-S-H during pozzolanic reaction with silica flour, silica sand and calcined clay.

$SiO_2(am) + Ca(OH)_2(s) \rightarrow 3CaO{\cdot}2SiO_2{\cdot}3H_2O(s)$ formation of C-S-H from silica flour and $Ca(OH)_2$

The presence of silica sand in the silica sand cement design could be the cause of the anomaly observed in the comparison analysis of the TGA results. Since silica sand is a pozzolan, and therefore highly reactive, it could have already combined with the $Ca(OH)_2$ in the inside of

the core to form C-S-H (explained in 2.3.1). This would ultimately reduce the amount of $Ca(OH)_2$ in the inside of the core compared to its surface independent of the rate of leaching observed in the ICP and TGA results.

Therefore, the difference between the amount of $Ca(OH)_2$ present on the outside and the inside of the cores from all the designs in the TGA is critical when considering a wellbore. The outside of the core is very similar to the cement-formation interface where the cement is always in contact with the reservoir brine (Figure 2.3). The TGA result means there would be rapid dissolution of the calcium from the cement-formation interface which would result in microannulus formation along the cement-formation interface further exposing the cement sheath to degradation and also flow of gas through the microannuli or sustained casing pressure, which is in agreement with observations reported by Dusseault et al. who studied the impact of circumferential porosity and fractures on migration of formation fluids [Dusseault et al., 2000].

5.3 Cement Porosity

As predicted, the neat cement design had the greatest porosity change since it does not have the benefit of the silica flour and other admixtures (Table 5.1) that produce hydration C-S-H and less $Ca(OH)_2$. Based on the closeness of the porosity measurement using the UGV-200 Porosimeter for both the control and TCL samples, the porosity of cement with water to solid ratio of 0.87 appears to be in the 50% to 60% range. MIP porosity data confirms this observation that hardened cement paste with water to solid ratio of 0.87 should have porosity ranging from 50% to 60% [Mehta and Monteiro, 2006].

Table 5.1: Percent change in average porosity between samples cured at ambient temperatures and samples after 100 TCL.

Cement Sample	Percent Change in porosity (%)
Neat Cement	4.67
Steel Fiber	0.89
Silica Sand	1.68
Calcined Clay	0.57
Glass Fiber	0.59

The MIP data indicates that the changes in porosity due to dissolution and thermal cycling are occurring in the pores with 0.1 μm and 1 μm. This will have enormous detrimental effect as it would further increase permeability of the cement and lead to corrosion of the casing. The implication of this observation is that in order to make cement more durable under such environmental conditions, initial cement design need to yield more C-S-H as hydration products where the associated porosity is less than 0.1 μm.

5.4 Cement Permeability

For all the cement designs, permeability was higher in samples after 100 thermal cycles compared to those exposed to formation brine at ambient temperature. This result shows that the thermal cycles of the cement will cause permeability of the cement sheath to increase (Table 5.2). As the cement cores are heated to 90^0C, they expand, and as the temperature drops to 40^0, the cement contracts. Repetition of this process probably led to the fractures within the cement sheath and hence the higher permeability in samples after 100 thermal cycles.

The main aim of adding the steel fiber and glass fibers is to bridge fractures that would result from thermal cycle loading, thereby preventing the flow of fluids through the cement

matrix. Based on the permeability result, the steel cement is efficient at mitigating the flow of fluid through the cement.

Table 5.2: Change in average permeability between samples cured at ambient temperatures and samples after 100 TCL.

Sample	Change in Permeability due to TCL (nD)
Neat Cement	144.8
Steel Fiber	10.23
Silica Sand	168.3
Calcined Clay	82.37
Glass Fiber	41.69

There is a relationship between the amount $Ca(OH)_2$ present in the cement sheath, change in porosity and change in permeability due to the thermal loading for the cement designs except for the silica sand cement design. The higher the amount of $Ca(OH)_2$ present in the cement sheath, the higher the porosity and permeability for the neat, steel fiber, calcined clay and glass fiber cement design. The relationship is true for porosity in silica sand cement design. The opposite occur in permeability for silica sand design but the same theory can be used to explain this result. Since there is more $Ca(OH)_2$ present in the inner region of the silica sand cement core, there is more positive change in porosity in the inner region compared to the outer region of the core. Because of the higher porosity in the inner region of the silica sand, water can easily flow through the core which results in the higher change in permeability. Therefore, there is correlation between the physical changes in the cement in terms of porosity and permeability with the leaching process (Figure 5.1).

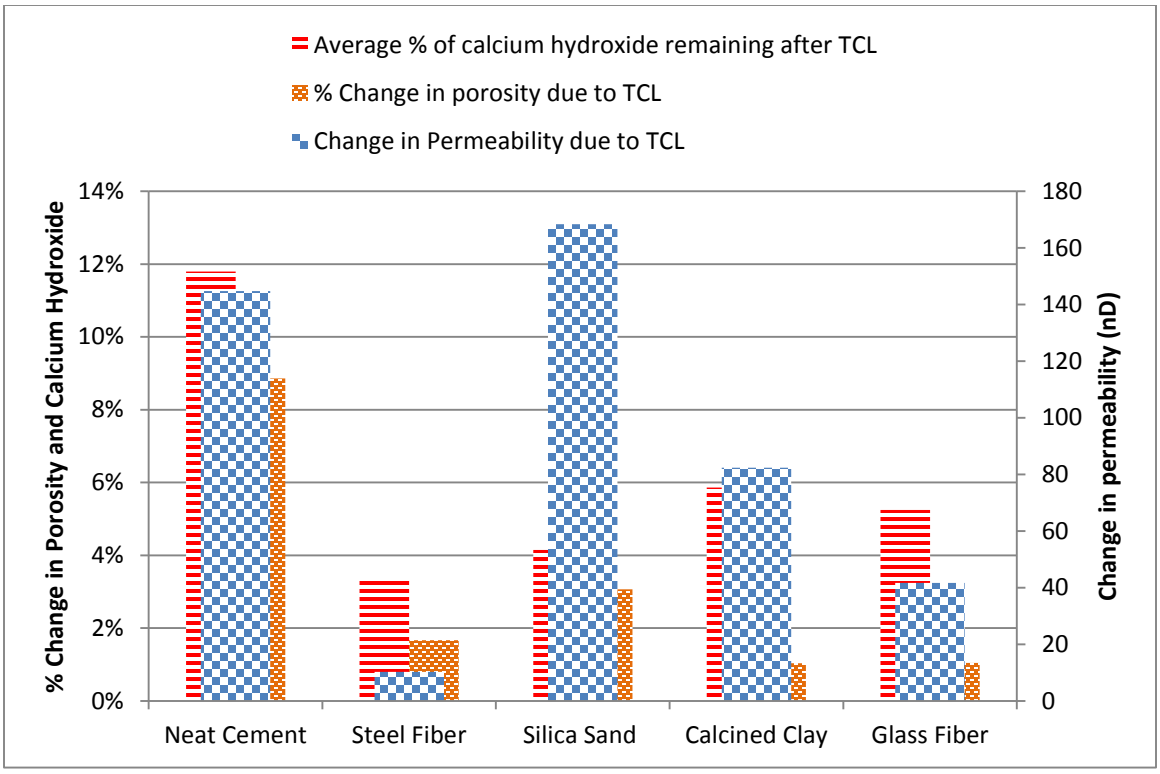

Figure 5.1: Change in porosity plotted against change in $Ca(OH)_2$. This shows that there is a relationship between the amount of $Ca(OH)_2$ in the cement core and change in porosity of the cement designs. The higher the amount of $Ca(OH)_2$ present in the cement design the higher the change in porosity due to thermal cycle loading.

5.5 Mechanical Property of the Cement Design

The compressive strength measurements showcase why additives need to be added to neat cement and the need for the design to be tested in the laboratory before field use. The steel fiber cement samples exhibited high and consistent compressive strength measurements especially in cores subjected to thermal loading cycles. The strength of the neat cements and glass fiber cements were great at ambient conditions but under thermal loading conditions were very poor. As shown in Table 5.3, there was a 64% and 53% loss in strength between neat cement samples that were cured at ambient conditions and neat cement samples after 100 thermal cycles for the neat cement and glass fiber cement respectively.

Table 5.3: Percent change in average compressive strength between samples cured at ambient temperatures and samples after 100 TCL.

Cement Design	Percent Change in Compressive Strength due to TCL (%)
Neat Cement	64
Steel Fiber	24
Silica Sand	5
Calcined Clay	18
Glass Fiber	53

The silica sand and calcined clay samples undergone the least change in compressive strength. This can be attributed to the pozzolanic nature of the cement resulting in additional C-S-H in the cement sheath. The added quartz grains appear to prevent loss of strength.

5.6 SEM Micrographs and EDS Analysis

The SEM micrographs gave an insight to why different cement designs have various porosity and permeability values. The was abundance of larger C-S-H in the neat cement core matrix after 100 thermal cycle loading compared to the rest of the cement designs. Packing of large, coarse C-S-H resulted in the larger porosity measurement resulting from the typical inefficient packing of large, coarse crystals.

The bond between the steel fibers and the cement matrix could be observed in SEM micrographs of the steel cement samples as they kept their shapes (Figure 5.2). This could explain why the steel cement samples possess high and consistent compressive strength as they provided further resistance to the applied load. The better the fibers are attached to the C-S-H in the cement matrix, the better the strength of the cement especially with regards to tensile and shear strength as it would require more force to dislodge the fiber from the matrix. Since the steel

fiber is carbon based, one concern about its use in cement would be its reliability against corrosion during long time exposure to hot brine.

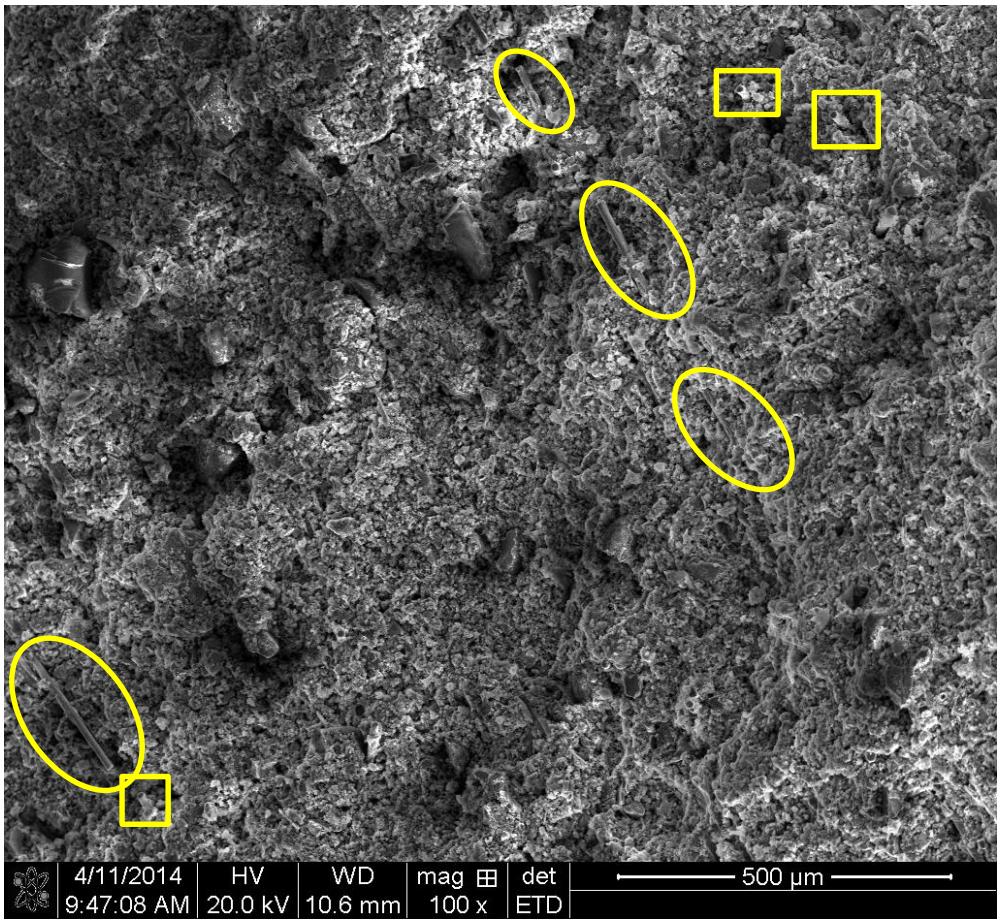

Figure 5.2: Low magnification SEM micrograph of a steel fiber cement sample. The steel fibers could be easily identified in the micrograph as they kept their size and form in the cement. Outlined in rectangles are steel fibers oriented perpendicular to the evaluated surface, and in ovals are steel fibers are parallel to the evaluated surface.

The glass fiber SEM micrographs could also be used to explain why it had the highest porosity but the least permeability 100 thermal cycles and the least change in the microstructure due to TCL. The main aim of adding the glass fibers is to enhance the toughness and strength by synergistically interacting with the micro cracks that developed when the cement sheath is loaded. They were supposed to keep their shape and size in the cement sheath. What was observed was the glass fibers were swelling and dissolving in the cement (Figure 5.3). This

means the glass fibers were susceptible in alkaline medium which hydrated cement is. As the glass fiber dissolves in the cement, they are able to flow and form a new mineral in the cement fractures thereby limiting permeability. This phenomenon have been observed in vegetable fibers, where they dissolve in cement matrix due to cement alkaline pore water [Savatano Jr. et al., 2009] Figure 5.3 A shows that there are abundance of isolated etched pits in the cement as the glass fiber reacts with the cement crystals, contributing to the porosity of the cement. In short time, this may be good for the for the cement sheath as permeability is reduced but as the new mineral (type of C-S-H) starts to precipitate and crystallize, it would cause the cement sheath to crack and fracture a typical phenomenon of crystal growth in solid materials. A possible new mineral that could form from glass fiber dissolving in cement would be a type of C-S-H, since Ca from the cement would preferential react with the quartz from the glass fiber. A way of remedying this process is by adding aluminium to the cement mix as seen in aluminium silicate cement [Suguma, 2006]. One way of doing this is by adding both glass fiber and the calcined clay (the calcined clay additive has ~20% aluminium oxide) to the cement mix. By reducing the Ca and increasing the Al content of the cement, the reaction between glass fiber and cement can be limited.

The SEM micrographs also provide information with regards to the chemical reaction between the silica (quartz) in the cement and the rest of the cement matrix. The quartz in most of the samples serves as foundation for the growth of C-S-H (Figure 5.4). The seedlets on the quartz grains (Figure 4.13 B) are clear indication of chemical interaction between the quartz grains and the surrounding cement matrix.

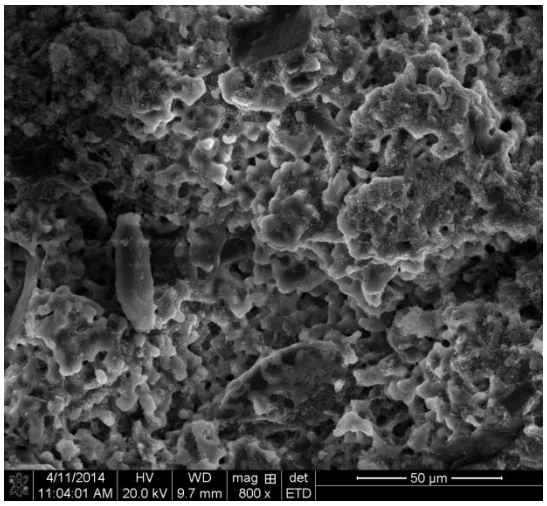

A. Low magnification SEM micrograph of glass fiber cement showing swelling and dissolution of glass fiber in the cement sheath.

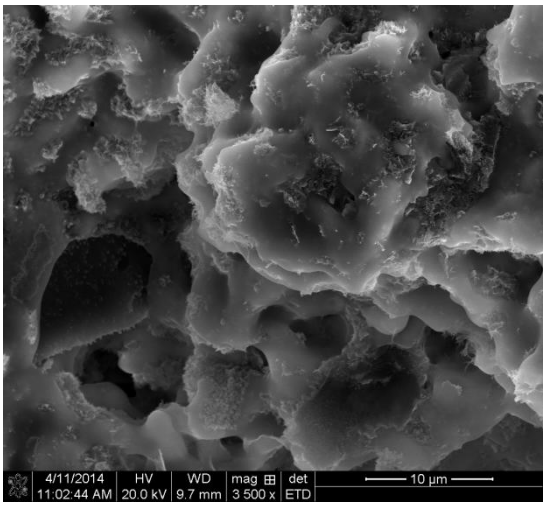

B. High magnification SEM micrograph of the glass fiber cement. Etched pits (isolated pores) in the micrograph are result of preferential dissolution of the glass fiber.

Figure 5.3: SEM micrograph of glass fiber cement samples after 100 thermal cycles.

High amount of chlorine (Cl) was observed in EDS analysis of glass fiber, silica sand, steel fiber cement, and calcined clay cements especially in the pores. The only possible source for the Cl elements present in the pores of the samples and internal pores of the C-S-H is the curing brine which contains Na^+ and Cl^- as the hydration products of cement samples did not have these elements. A possible hypothesis for the presence of Cl in the cement matrix is that Cl^- from the brine was diffused into the cement pore water since the concentration of Cl^- was higher in the brine, and almost nonexistent in the cement pore water. In addition, as $Ca(OH)_2$ is dissolved from the cement sheath and the porosity increases (discussed in section 5.1, 5.2, and 5.3), the brine is able to infiltrate the cement pores. This hypothesis is backed by the high content of the Na and Cl elements measured in silica sand cement design (Figure 4.12D) and the fact this cement has the highest porosity.

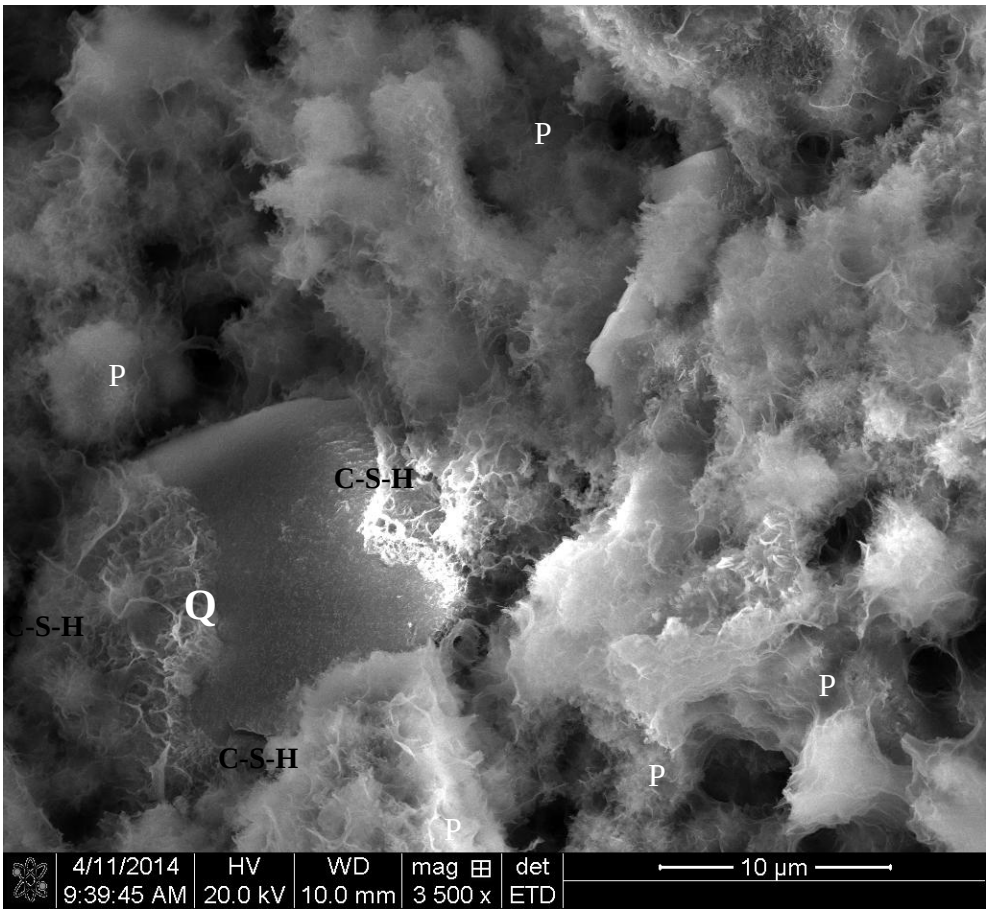

Figure 5.4: SEM micrograph of steel fiber cement sample after 100 thermal cycles. Growth of C-S-H from the quartz (Q) grain can be seen in the lower left corner. P represents the pore spaces.

CHAPTER 6: CONCLUSIONS AND RECOMMENDATIONS

6.1 Conclusions

This study established an experimental process to test cement integrity under thermal cycling with the application to geothermal wellbore environment. It is very crucial to experimentally investigate the effect of thermal cycle loading on the cement sheath durability in a zero-mass withdrawal wellbore as the success of the cement sheath can determine the life of the wellbore.

Using Portland cement in the geopressured geothermal reservoirs in the Gulf of Mexico would be a problem and could greatly increase the cost of the wellbore over time as regular cement remediation would be required to make the wellbore safe. Leaching of Ca^{2+} out of the cement sheath due to contact with acidic brine would result significantly increase the cement sheath porosity. Preferential dissolution along the cement-formation interface could ultimately result in well having sustained casing pressure issues.

Thermal loading of the well would cause thermal cracks in the cement sheath causing the permeability of the cement sheath to increase and weaken the wellbore although addition of silica flour and fibers would be effective in mitigating the rate of deterioration.

This study as summarized by Figure 6.1 shows that silica flour is needed as part of the cement mix if Portland cement is used in a wellbore in this location. Even with the uncertainties with the measurements, steel fiber performed better consistently with regards to porosity, permeability and compressive strength and can be added to improve the quality of the cement sheath.

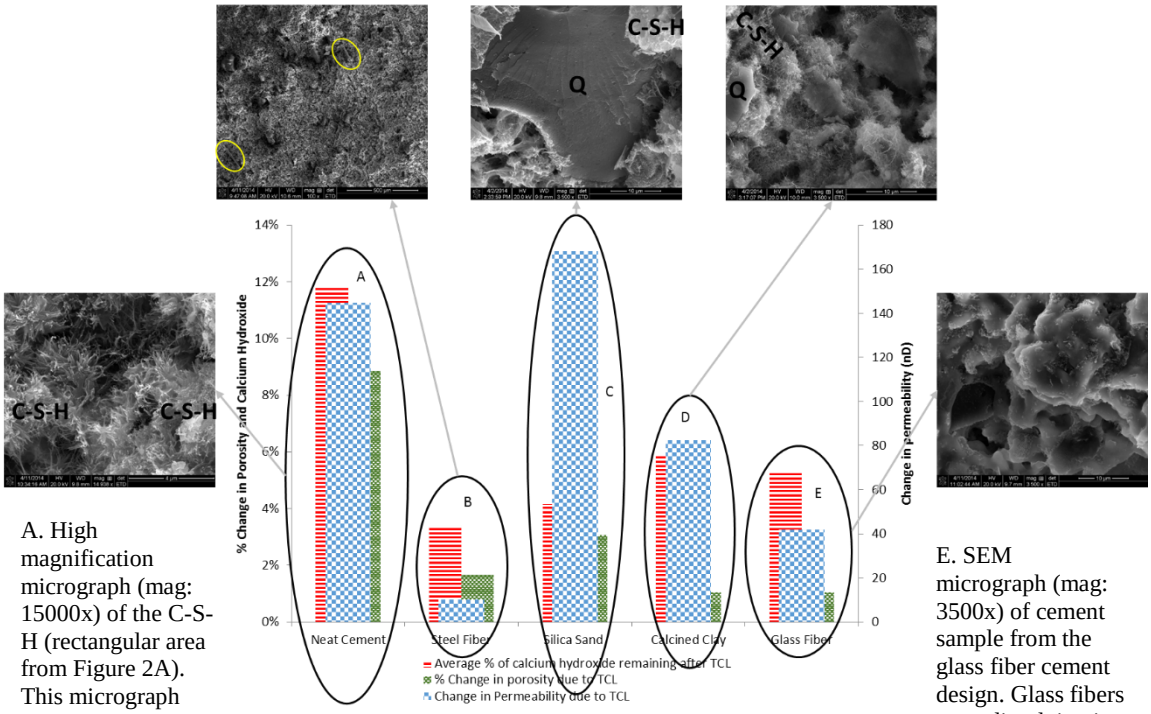

Figure 6.1: Relationship between physical and chemical properties of the cement design. The presence of larger, coarse C-S-H and high amount of $Ca(OH)_2$ in the neat cement design (A) made it vulnerable to leaching of Ca^{2+} as seen in the porosity and permeability results. The presence of denser, smaller amount of $Ca(OH)_2$ and the steel fibers(B) which are bridging across the pores contributed to the low change in porosity and permeability observed in the steel fiber cement design (B). Even though the silica sand cement design cores have small amount of $Ca(OH)_2$ (C), they were more permeable due to thermal cycle loading as there was more change in porosity on the inside of the cores due to leaching. The permeability of the calcined clay cement design cores (D) changed greatly compared to its porosity due to thermal cycle loading. Because glass fiber cement is alkaline, it dissolves in cement when it is combined with silica flour in the cement design as the silica flour makes the cement pore water becomes more acidic as $Ca(OH)_2$ is used to make more C-S-H.

6.2 Recommendations

For future work, similar experiment can be done with different concentration of the secondary additives namely silica sand, steel fiber, calcined clay, and glass fiber to study how that would affect the results. A design with silica flour and both of the fibers can be tested using same protocol established in this study, and see if the performance of calcium based cement under thermal cycling can be improved.

These experiments should be conducted over longer period resulting in multiple cycles. Since the brine contact on the cement plays a significant role, a flow through experiment could be done in place of a batch experiment. This would influence the porosity, permeability, and strength values which would be beneficial in making reliable long term projection on the wellbore cement.

Experiments with different cement systems, various formations and casing surface finishes can be executed. Similar experiments on cemented pipes are suggested to simulate thermal cycling on the wellbore. This can provide insight into the stress effect of casing expansion and cooling from thermal cycling on cement microstructure and mechanical properties. The pipes can also be expanded using the expandable casing technique to see if the properties of the cement can be improved [Radonjic, 2013; Kupresan et al., 2013, and Kupresan et al., 2014].

REFERENCES

1. Abell, A.B., Willis, K.L., and Lange, D.A.: "Mercury Intrusion Porosimetry and Image Analysis of Cement Based Materials" Journal of Colloid and Interface Science, Volume 211, pp. 39-44, 1999.

2. Ambroise, J., Murat, M., and Pera, J.: "Hydration Reaction and Hardening of Calcined Clays and Related Materials: V. Extension of the Research and General Conclusions.", Cement and Concrete Research, Volume 15, pp. 261-268, 1985.

3. Berndt, M.L., and Philippacoulos, A. J.: "Incorporation of Fibres in Geothermal Well Cements", Geothermics, Volume 31, pp. 643-656, 2002.

4. Bishop, P.L., Gong, R., and Keener, T.C.: "Effects of Leaching on Pore Size Distribution of Solidified/ Stabilized wastes", Journal of Hazardous Materials, Volume 31, Issue 1, pp. 59-74, June 1992.

5. Bois, A.P., Garnier, A., Galdiolo, G., and Laudet, J.B.: "Use of a Mechanistic Model to Forecast Cement-Sheath Integrity", SPE Journal paper 139668-PA, SPE Drilling and Completion, Volume 27, Number 2, June 2012.

6. Bosma, M., Ravi, K., van Driel, W., and Schreppers, G.J.: "Design Approach to Sealant Selection for the Life of the Well", SPE paper 56536 prepared for presentation at the 1999 SPE Annual Technical Conference and Exhibition held in Houston, Texas, USA, 1999.

7. Boulin, P.F., Bretonnier, P., Gland, N., and Lombard, J.M.: "Contributions of the Steady State Method to Water Permeability Measurement in Very Low Permeability Porous Media", Oil and Gas Science and Technologies-Rev, IFP Energies nouvelles, Volume 67, pp. 387-401, 2012.

8. Cavanagh, P.H., Johnson, C.R., LeRoy-Delage, S., DeBruijn, G.G., Cooper, I., Guillot, D.J., Bulte, H., and Dargaud, B.: "Self-Healing Cement - Novel Technology to Achieve Leak-Free Wells", SPE-105781 presented at the SPE/IADC Drilling Conference, Amsterdam, The Netherlands, 20-22 February 2007.

9. Chen, T., and Stagg, P.W.: "Semilog Analysis of the Pulse-Decay Technique of Permeability Measurement", Society of Petroleum Engineers Journals. Doi: 10.2118/11818-PA, 1984.

10. Dorfman, M.: "The Outlook for Geopressured/Geothermal Energy and Associated Natural Gas", Journal of Petroleum Technology, Volume 34, Number 9, pp. 1915-1919, 1982.

11. Duguid, A., Radonjic, M. and Scherer, G.W.: "Degradation of Cement at the Reservoir/Cement Interface from Exposure to Carbonated Brine", International Journal of Greenhouse Gas Control, Volume 5, pp. 1413-1428, 2011.

12. Duguid, A., and Scherer, G.W.: "Degradation of Oil Well Cement Due to Exposure to Carbonated Brine", International Journal of Greenhouse Gas Control, Volume 4, pp. 546-560, 2010.

13. Dusseault, M.B., Gray, M.N., and Nawrocki, P.A.: "Why Oilwells Leak: Cement Behavior and Long-Term Consequences", SPE 64733 presented at the SPE International Oil and Gas Conference and Exhibition, Beijing, China, 2000.

14. Ekström, T.: "Leaching of Concrete: Experiments and Modeling", Report TVBM-3090, Lund Institute of Technology, Division of Building Materials, 2001.

15. Feng, Y.: "Numerical Study of Downhole Heat Exchanger Concept in Geothermal Energy Extraction from Saturated and Fractured Reservoirs", Ph.D. Dissertation, Louisiana State University, 2012.

16. Feng, Y., Tyagi, M., and White, C.D.: "Effect of Natural Convection Patterns on Optimal Location and Size of a Heat Sink in a Geothermal Reservoir", 36th Workshop on Geothermal Engineering, Stanford University, Stanford, California. 31 January – 2 February, 2011.

17. Feng, Y., Tyagi, M., and White, C.D.: "A Downhole Heat Exchanger for Horizontal Wells in Low-Enthalpy Geopresured Geothermal Brine Reservoirs", Geothermics, Volume 53, pp. 368-378, accessed September 9, 2014. http://www.sciencedirect.com/science/article/pii/S0375650514000844.

18. Gaurina-Medimurec, N., Matanovic, D., and Krklec, G.: "Cement Slurries for Geothermal Wells Cementing", Rudarsko-geoloSko-naftni zbornik, Volume 6, pp. 127-134, 1994.

19. Geothermal Energy Association: "2013 Annual US Geothermal Power Production and Development Report", accessed May 5, 2014. http://geo-energy.org/pdf/reports/2013AnnualUSGeothermalPowerProductionandDevelopmentReport_Final.pdf.

20. Goldstein, J., Newbury, D., Joy, D., Lyman, C., Echlin, P., Lifshin, E., Sawyer, L., and Michael, J.: "Scanning Electron Microscopy and X-Ray Microanalysis", Third Edition, Kluwer Academic/Plenum Publishers, New York, 2003.

21. Gray, T.: "Geothermal Resource Assessment of the Gueydan Salt Dome and the Adjascent Southeast Gueydan Field, Vermilion Parish, Louisiana", Master's Thesis, Louisiana State University, 2007.

22. Griggs, J.: "A Re-Evaluation of Geopressured-Geothermal Aquifers as an Energy Resource", Master's Thesis, Louisiana State University, 2004.

23. Guen, Y.L., Gouevec, J.L., Chammas, R., Gerard, B., Poupard, O., Van Der Beken, A., and Jammes, L.: "CO_2 Storage: Managing the Risk Associated With Well Leakage Over Long

Time Scales", SPE-116424, SPE Projects, Facilities & Construction, Volume 4, Issue 3, pp. 87-96, 2009.

24. Hanor, J.S., and Mercer, J.A.: "Spatial Variations in the Salinity of Pore Waters in Northern Deep Water Gulf of Mexico Sediments: Implications for Pathways and Mechanisms of Solute Transport", Geofluids, Volume 10, pp. 83-93, 2010.

25. Herrin, E.: "Environmental Problems Associated with the Production of Energy from Geopressured Reservoirs", Geopressured Geothermal Energy Conference, Austin, Texas, June 2-4, 1975.

26. Hewlett, P.C.: "Lea's Chemistry of Cement and Concrete", Fourth Edition, Elsevier, 1998.

27. Iijima, A.: "Geology of Natural Zeolites and Zeolitic Rocks", Pure and Applied Chemistry, Volume 52, pp. 2115-2130, 1980.

28. Jain, J. and Neithalath, N.: "Analysis of Calcium Leaching Behavior of Plain and Modified Cement Pastes in Pure Water", Cement and Concrete Composites, Volume 31, Issue 3, pp. 176-185, 2009.

29. Jones, S.C.: "A Technique for Faster Pulse-Decay Permeability Measurements in Tight Rocks", SPE Formation Evaluation, 1997.

30. Kupresan, D., Heathman, J., and Radonjic, M.: "Application of a New Physical Model of Expandable Casing Technology in Mitigation of Wellbore Leaks", Journal of Canadian Energy Technology & Innovation (CETI), Volume 1, Number 5, December 2013.

31. Kupresan, D., Heathman, J., and Radonjic, M.: "Experimental Assessment of Casing Expansion as a Solution to Microannular Gas Migration", Paper SPE 168056 presented at IADC/SPE Drilling Conference, Fort Worth, Texas, 4-6 March, 2014.

32. Kutchko, B.G., Strazisar, B.R., Dzombak, D.A., Lowry, G.V., and Thaulow, N.: "Degradation of Well Cement by CO_2 under Geologic Sequestration Conditions", Environ. Sci. Technol., Volume 41, Issue 13, pp. 4787-4792, 2007.

33. Lepper, G.B.: "Production Casing Performance in a Thermal Field", Journal of Canadian Petroleum Technology. Volume 37, Number 9, 1998.

34. McCoy, R., Hartsock, J., and Dobson, R.: "Preliminary Results of The Wells-of-Opportunity Geopressured-Geothermal Testing Program", SPE Unconventional Gas Recovery Symposium, Pittsburgh, Pennsylvania, 18-21 May, 1980.

35. Mehta, P.K., and Monteiro, P.J.: "Concrete: Microstructure, Properties, and Material", 2006.

36. Natural Renewable Energy Laboratory: "Geothermal Maps", accessed May 5, 2014. http://www.nrel.gov/gis/geothermal.html.

37. Nelson, E.B.: "Well Cementing", Schlumberger, Sugar Land, Texas, 1990.

38. Nelson, E.B. and Guillot, D.: "Well Cementing", Schlumberger, Houston, Texas, 2006.

39. Ozyurtkan, M.H., and Radonjic, M.: "An Experimental Study of the Effect of CO_2 Rich Brine on Artificially Fractured Well-Cement", Cement and Concrete Composites, Volume 45, pp. 201-208, 2014.

40. Plaksina, T.: "Modeling Effects of Coupled Convection and CO_2 Injection in Stimulating Geopressured Geothermal Reservoirs", Master's Thesis, Louisiana State University, 2011.

41. Radonjic, M., Heathman, J., and Kupresan, D.: "Analysis of Defect-Free Wellbore Cement Microstructure Created by In-Situ Mechanical Manipulation", Paper presented at 21st Annual International Conference on Composites/Nano Engineering, Tenerife, Spain, 21-27 July, 2013.

42. Recommended Practice For Testing Oil-Well Cements And Cement Additives, API Recommended Practice 10B, Twentieth Edition, American Petroleum Institute, April, 1977.

43. Savastano Jr., H., Santos, S.F., Radonjic, M., and Sobeyejo, W.O.: "Fracture and Fatigue of Natural Fiber-Reinforced Cementitious Composites", Cement and Concrete Composites, Volume 31, pp. 232-243, 2009.

44. Scherer, G.W., Valenza, J.J., and Simmons, G.: "New Methods to Measure Liquid Permeability in Porous Materials", Cement and Concrete Research, Volume 37, pp. 386-397, 2006.

45. Shryock, S.H.: "Geothermal Well Cementing", 5th SPE Offshore South East Asia Conference, 21-24 February 1984.

46. Sugama, T.: "Advanced Cements for Geothermal Wells", Final report prepared for The U.S Department of Energies Office of Geothermal Technologies, Brookhaven National Laboratory, Upton, New York, 2006.

47. Susan Swapp: "Scanning Electron Microscopy (SEM)" , accessed October 23, 2013. http://serc.carleton.edu/research_education/geochemsheets/techniques/SEM.html.

48. Taoutaou, S., Osman, T.M., Mjthab, M., Succar, N.: "Well Integrity in Heavy Oil Wells: Challenges and Solutions", CSUG/SPE 137079 paper prepared for presentation at the Canadian Unconventional Resources & International Petroleum Conference held in Calgary, Alberta, Canada, 2010.

49. Taylor, H. F. W.: “Cement Chemistry”, Thomas Telford Services, London, 1997.

50. Tian, B. and Cohen, M.D.: “Does Gypsum Formation During Sulfate Attack on Concrete Lead to Expansion?”, Cement and Concrete Research, Volume 30, Issue 1, pp. 117-123, 2000.

51. U.S. Energy Information Administration: “How much U.S. Electricity is Generated from Renewable Energy?” accessed May 5, 2014. http://www.eia.gov/energy_in_brief/article/renewable_electricity.cfm.

52. U.S. Energy Information Administration: “What are the Major Sources and Users of Energy in the United States?” accessed May 5, 2014. http://www.eia.gov/energy_in_brief/article/major_energy_sources_and_users. cfm.

53. Vejmelková, E., Keppert, M., Rovnaníková, P., Keršner, Z., and Černý, R.: “Application of Burnt Clay Shale as Pozzolan Addition to Lime Mortar”, Cement and Concrete Composites, Volume 34, Issue 4, pp. 486-492, 2012.

54. Vignes, B., and Aadnøy, B.: “Well-Integrity Issues Offshore Norway”, SPE 112535-PA, SPE Production & Operations Journal, Volume 25, Number 2, pp. 145-150, May 2010.

55. White, D.F., and Williams, D.L.: “Assessment of Geothermal Resource of the United States.” Technical Report, U.S. Geological Survey (USGS) Circular 726, 1975.

56. Yalcinkaya, T.: “Experimental Study on Single Cement Fracture Exposed to CO_2 Saturated Brine Under Dynamic Conditions”, Master's Thesis, Louisiana State University, 2010.

57. Yalcinkaya, T., Radonjic, M., Hughes, R.G., Willson, C.S., and Kyungmin, H.: “The Effect of CO_2-Saturated Brine on the Conductivity of Wellbore-Cement Fractures”, SPE-139713, SPE Drilling & Completion, Issue 3, pp. 332-340, 2011.

58. Yalkinkaya, T., Radonjic M., Willson C.S., and Bachu S.: “Experimental Study on a Single Cement-Fracture Using CO_2 Rich Brine”, Energy Procedia, Volume 4, pp. 5335-5342, 2011.

59. Yang, H., Jiang, L., Zhang, Y., Pu, Q., and Xu, Y.: “Predicting the Calcium Leaching Behavior of Cement Pastes in Aggressive Environments”, Construction and Building Materials, Volume 29, pp. 88-96, 2012.

APPENDIX A: PREPARATION OF CEMENT SAMPLES

A.1 Preparation of 13.1 lb/gal Neat Cement Cores

1. Brass core molds (Figure 3.1B) were lubricated with Vaseline® petroleum jelly and Great Value® Vegetable cooking spray to allow for easy removal of cement cores after wait on cement. The bottom of each brass mould was covered with aluminium plate.
2. 8.6g of bentonite was mixed with 374g of distilled water in Waring® one Liter blender (Figure 3.1 A) on low speed at approximately 16,000 revolutions per minute (RPM) for minutes.
3. 430g of class H cement was then added to the mixture in the blender and mixed high speed (approximately 20000 RPM) for 35 seconds.
4. Cement slurry was poured into brass moulds from (1). The top of the moulds was covered with aluminium plates.
5. Cement was left on workbench for 24 hours to set and harden (WOC).
6. The neat cement cores were de-moulded and placed in brine for the thermal cycle loading and water bath as control samples.

A.2 Preparation of Steel Fiber Cement Cores

1. Brass core moulds (Figure 3.1 B) were lubricated with Vaseline® petroleum jelly and Great Value® Vegetable cooking spray to allow for easy removal of cement cores after wait on cement. Bottom of the brass moulds were covered with aluminium plates.
2. 8.6g of bentonite was mixed with 520g of distilled water in Waring® one Liter blender (Figure 3.1 A) on low speed at approximately 16,000 revolutions per minute (RPM) for minutes.

3. 430g of class H cement, 150.5g of silica flour, and 8.6g of steel fiber were added to the mixture in the blender and mixed high speed (approximately 20,000 RPM) for 35 seconds.
4. Cement slurry was poured into brass moulds from (1). The top of the mould were covered with aluminium plate.
5. Cement was left on workbench for 24 hours to set and harden (WOC).
6. The steel fiber cement cores were de-moulded and placed in brine for the thermal cycle loading and water bath as control samples.

A.3 Preparation of Silica Sand Cement Cores

1. Brass core moulds (Figure 3.1B) were lubricated with Vaseline® petroleum jelly and Great Value® Vegetable cooking spray to allow for easy removal of cement cores after wait on cement. Bottom of each brass mould was covered with aluminium plate.
2. 8.6g of bentonite was mixed with 520g of distilled water in Waring® one Liter blender (Figure 3.1 A) on low speed at approximately 16,000 revolutions per minute (RPM) for minutes.
3. 430g of class H cement, 150.5g of silica flour, and 8.6g of silica sand were added to the mixture in the blender and mixed high speed (approximately 20,000 RPM) for 35 seconds.
4. Cement slurry was poured into the brass moulds from (1). The top of the moulds were covered with aluminium plates.
5. Cement was left on workbench for 24 hours to set and harden (WOC).
6. The silica sand cement cores were de-moulded and placed in brine for the thermal cycle loading and water bath as control samples.

A.4 Preparation of Calcined Clay Cement Cores

1. Brass core moulds (Figure 3.1B) were lubricated with Vaseline® petroleum jelly and Great Value® Vegetable cooking spray to allow for easy removal of cement cores after wait on cement. Bottom of each brass mould was covered with aluminium plate.
2. 8.6g of bentonite was mixed with 520g of distilled water in Waring® one Liter blender (Figure 3.1 A) on low speed at approximately 16,000 revolutions per minute (RPM) for minutes.
3. 430g of class H cement, 150.5g of silica flour, and 8.6g of calcined clay were added to the mixture in the blender and mixed high speed (approximately 20000 RPM) for 35 seconds.
4. Cement slurry was poured into the brass moulds from (1). The top of the moulds were covered with aluminium plates.
5. Cement was left on workbench for 24 hours to set and harden (WOC).
6. The calcined cement cores were de-moulded.
7. The calcined clay cement cores were placed in brine and water bath for the thermal cycle loading and as control samples respectively.

A.5 Preparation of Glass Fiber Cement Cores

1. Brass core moulds (Figure 3.1B) were lubricated with Vaseline® petroleum jelly and Great Value® Vegetable cooking spray to allow for easy removal of cement cores after wait on cement. Bottom of each brass mould was covered with aluminium plate.
2. 8.6g of bentonite was mixed with 520g of distilled water in Waring® one Liter blender (Figure 3.1 A) on low speed at approximately 16,000 revolutions per minute (RPM) for minutes.

3. 430g of class H cement, 150.5g of silica flour, and 8.6g of glass fiber were added to the mixture in the blender and mixed high speed (approximately 20000 RPM) for 35 seconds.
4. Cement slurry was poured into the brass moulds from (1). The top of the moulds were covered with aluminium plates.
5. Filled moulds were left on workbench for 24 hours to allow cement to set and harden (WOC).
6. The glass fiber cement cores were de-moulded and placed in brine for the thermal cycle loading and water bath as control samples.

APPENDIX B: PROPERTIES OF MATERIALS USED IN EXPERIMENT

B.1 Class H Cement

The class H cement used in cement slurry was donated by Lafarge. Table B.1 displays the chemical composition of the cement.

Table B.1: Class H cement clinker analysis performed by Lafarge.

Mineral	Percentage Composition
Silica Dioxide (SiO2)	21.40%
Aluminum Oxide (Al2O3)	2.70%
Ferric Oxide (Fe2O3)	4.50%
Calcium Oxide (CaO)	63.60%
Magnesium Oxide (MgO)	2.60%
Sulphur Trioxide (SO3)	2.90%
Loss on Ignition	0.83%
C4AF+2C3A	12.87%
Free Lime (XRD value)	0.96%
Tricalcium Silicate (C3S)	63%
Tricalcium Aluminate	0%
Total Alkali as Sodium Oxide	0.23%
Insoluble Residue	0.37%

B.2 Silica Flour

The silica flour was a gift from Halliburton Fluids Laboratory in Broussard, LA. The product trade name is SS-200. It has a specific gravity of 2.63 to water at 20°C and a molecular weight of 60.09 g/mol. It is made of 60-100% crystalline silica (SiO_2).

B.3 Silica Sand

The silica sand with product trade name of MICROSAND was also gifted by Halliburton Fluids Laboratory in Broussard, LA. It is very similar to the silica flour in composition with the

grain size as the difference. It is made of 60-100% crystalline silica (SiO_2), a specific gravity of 2.65 to water at 20^0C and a molecular weight of 60 g/mol.

B.4 Calcined Clay

txi Energy Services provided the calcined clay that was used in the calcined clay cement design. The product trade name is PRESSUR-SEAL™ Fine. Its specific gravity vary between 2.2 to 2.5 while the bulk density 0.7845 g/cc (49 lb/ft^3]. Approximately 70% of the calcined clay would pass through a 325 mesh while about 90% of it would pass through a 200 mesh. Therefore, the grain size of the calcined clay is between 45μm to 75μm. Table B.2 displays the chemical analysis of the calcined clay.

Table B.2: Chemical Analysis of Silica Flour (PRESSUR-SEAL™ Fine).

Oxide	% Range
SiO_2	61-82
Al_2O_3	14-20
Fe_2O_3	6-Apr
CaO	0.8-3.5
MgO	0.6-3.1
SO_3	0.05-1.25
P_2O_5	0.1-0.3
TiO_2	0.5-1.2
Mn_2O_3	0.00-0.15
Na_2O	0.0-1.4
K_2O	1.0-3.2

B.5 Steel Fiber

The steel fiber used in the steel fiber cement is a product of Halliburton. The product trade name of the steel fiber is STEELSEAL® 400. It is an angular, dual composition carbon

based material. It is made out of 60-100% calcined petroleum coke and has a specific gravity of 1.75 to water at 20°C. Owning to its trade name, it has a particle size of 400 μm.

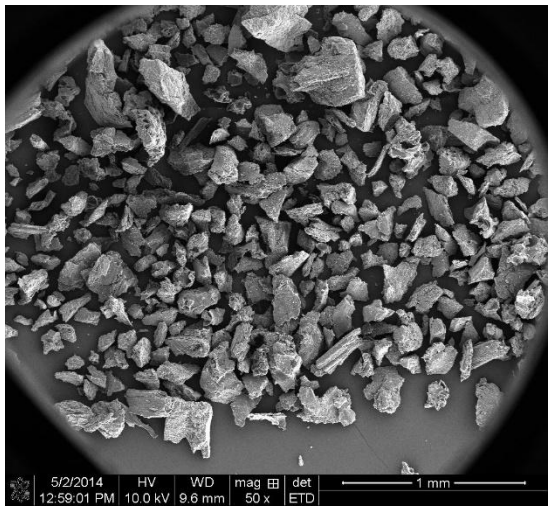

A. SEM micrograph of the steel fiber used in the cement design. The grain sizes are in the 400 μm range.

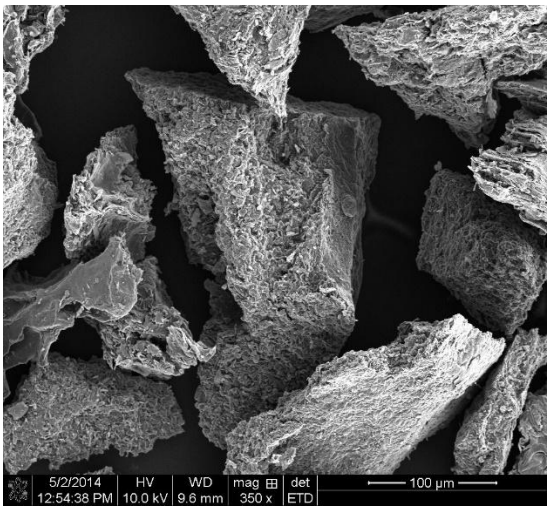

B. Magnified SEM depicting the microstructure of the carbon based steel fiber.

Figure B.1: SEM micrographs of the steel fibers (STEELSEAL® 400).

B.6 Glass Fiber

WellLife™ 74, a product of Halliburton was the glass fiber used in the glass fiber cement slurries. Made of 60-100% glass, it has a specific gravity of 2.62 to water at 20°C and a bulk density of 0.7048 g/cc (44 lb/ft^3).

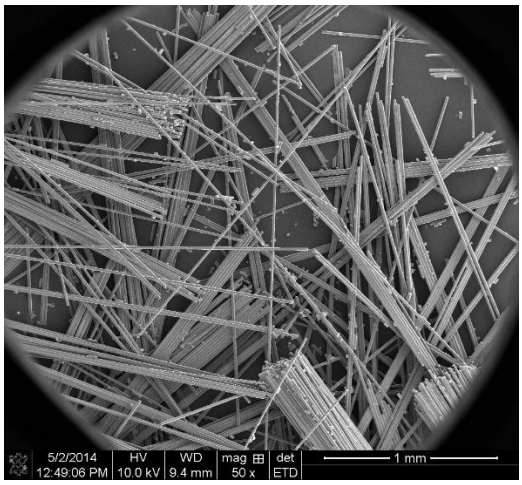	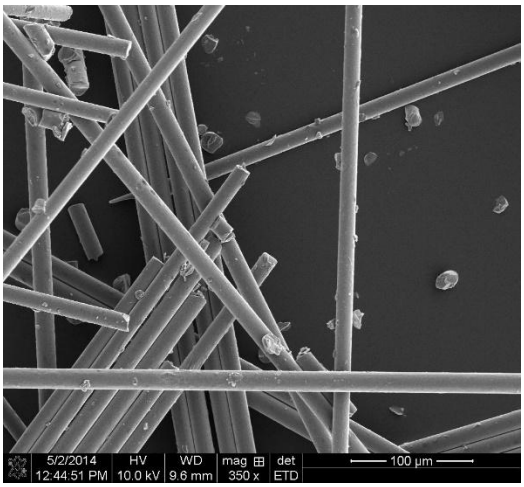
A. SEM micrograph of spherical straight glass fiber.	B. Magnified SEM micrograph of glass fiber.

Figure B.2. SEM micrographs of the glass fibers (WellLife™ 74) used in the cement design.

APPENDIX C: SAMPLE PREPARATION FOR ANALYSIS

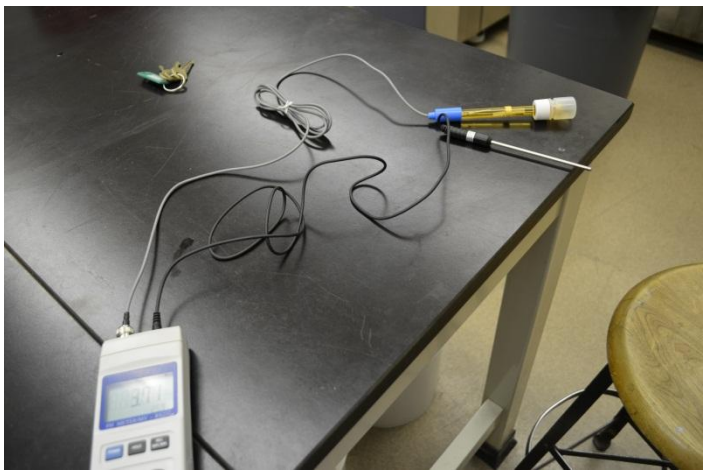	A. pH meter with temperature probe and pH probe.
	B. pH meter was calibrated in pH 7 buffer solution.
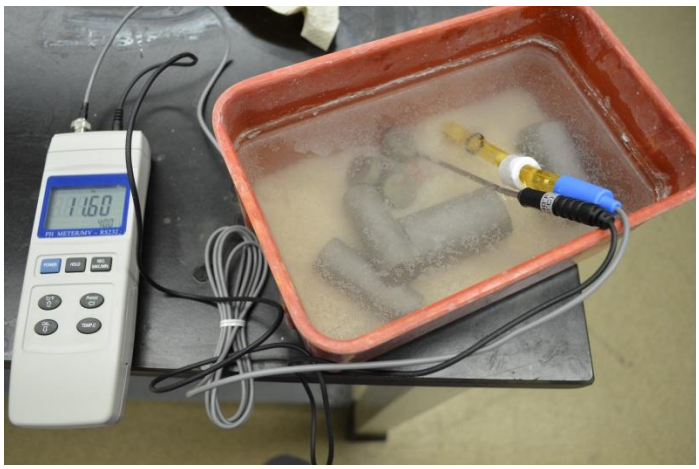	C. pH and temperature probe placed in brine to measure pH of the brine.

Figure C.1: Process for measuring pH of brine.

	
A. 3 in. core sample removed from curing fluid.	B. 3 in. core been prepared to be cut into 2 in. core. 2 in. marked on 3 in. core.
	
C. 2 in. core sample cut from the 3 in. core using a rock cutter.	D. 2 in. core used for porosity, permeability and compressive strength measurement while the left overs were used for SEM, TGA, MIP and XPS analysis.

Figure C.2: Cutting of cement core samples for porosity, permeability and compressive strength measurement.

	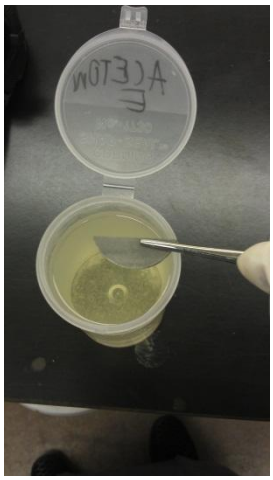
A. Cement core after cutting 2 in. core for porosity, permeability and compressive strength measurement. Remnants were used for SEM, TGA, MIP and XPS analysis.	B. Cement sample dipped in acetone to rapidly remove any water present on the cement surface thereby preventing carbonation.
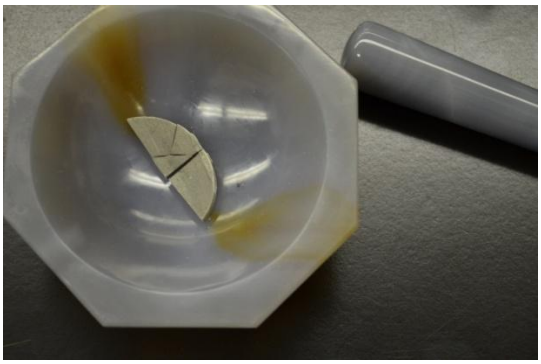	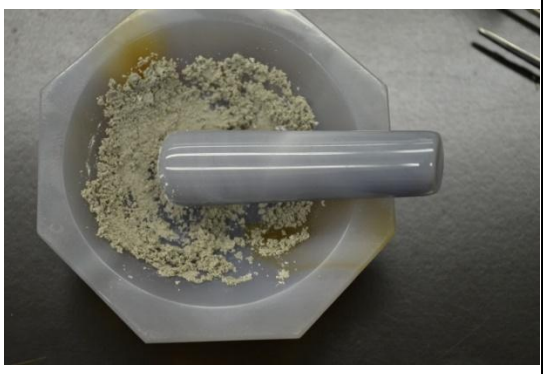
C. Dried sample placed in agate mortar to be crushed into powder.	D. Crushed cement samples used in TGA and XPS analysis.

Figure C.3: Sample preparation for TGA and XPS analysis.

<table>
<tr><td> 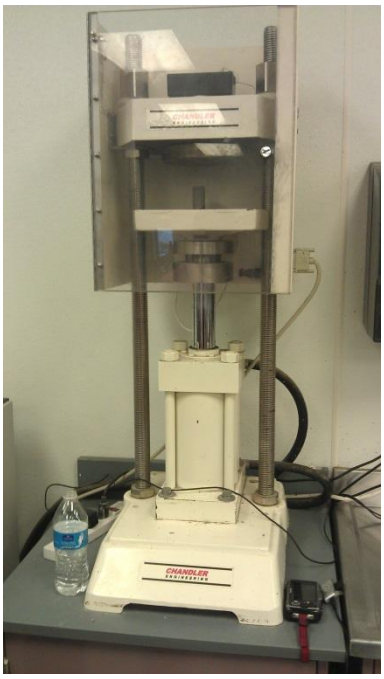 </td><td> 
</td></tr>
<tr><td>A. Cement core sample placed in hydraulic press used in compressive strength.</td><td>B. Automatic digital controller used in compressive strength measurement. The controller also recorded the maximum compressive force required to break the sample.</td></tr>
<tr><td> 
</td><td> 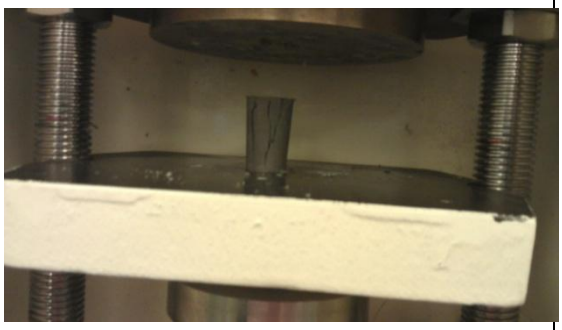 </td></tr>
<tr><td>C. Beginning of crushing cement core sample.</td><td>D. After crush test.</td></tr>
</table>

Figure C.4: Process for measuring compressive strength of cement cores.

APPENDIX D: COMPLETE POROSITY, PERMEABILITY, AND COMPRESSIVE STRENGTH RESULT AND ADDITIONAL SEM MICROGRAPHS

D.1 Porosity and Grain Density Data

Table D.1: Grain Density and Porosity Data for all samples measured, from control and thermal cycle loading experiment.

	Control		Thermal Cycling Loading	
Cement Sample	Grain Density (g/cc)	Porosity (%)	Grain Density (g/cc)	Porosity (%)
Neat-1	2.205	52.8483	2.354	56.72
Neat-2	2.222	52.625	2.350	57.87
Neat-3	-	-	2.326	57.64
Steel-1	2.277	53.6361	2.282	51.03
Steel-2	2.262	53.2995	2.386	56.25
Steel-3	-	-	2.420	55.81
Silica Sand-1	2.271	55.7252	2.393	57.00
Silica Sand-2	2.272	54.035	2.392	56.53
Silica Sand-3	-	-	2.362	56.16
Calcined Clay-1	2.274	54.1882	2.379	55.72
Calcined Clay-2	2.267	55.9311	2.382	55.36
Calcined Clay-3	-	-	2.440	55.81
Glass Fiber-1	2.281	56.7836	2.399	58.34
Glass Fiber-2	2.348	55.9781	2.355	56.87
Glass Fiber-3	-	-	2.437	55.69

D.2 Permeability Data

Table D.2: Permeability data for all samples measured both control and thermal cycle loading experiment.

	Control	Thermal Cycle Loading
Cement Sample	Permeability (nD)	Permeability (nD)
Neat Cement-1	1.51E+02	3.37E+02
Neat Cement-2	1.69E+02	2.80E+02
Neat Cement-3	-	2.99E+02
Steel-1	2.41E+02	2.41E+02
Steel-2	2.54E+02	2.74E+02
Silica Sand-1	2.31E+02	4.50E+02
Silica Sand-2	2.25E+02	5.07E+02
Silica Sand-3	-	2.33E+02
Calcined Clay-1	2.15E+02	3.26E+02
Calcined Clay-2	1.99E+02	2.53E+02
Calcined Clay-3	-	2.08E+02
Glass Fiber-1	1.71E+01	7.06E+01
Glass Fiber-2	1.10E+01	4.08E+01

D.3 Compressive Strength Data

Table D.3: Compressive strength results for all samples measured from control and thermal cycle loading experiment.

	Control		Thermal Cycle Loading	
Cement Sample	Compressive Strength in MPa	Compressive Strength in psi	Compressive Strength in MPa	Compressive Strength in psi
Neat-1	6.321	916.7	2.545	369.2
Neat-2	9.551	1385.3	1.843	267.4
Neat-3	-	-	4.08	592.1
Steel-1	4.451	645.5	2.413	350.1
Steel-2	3.485	505.5	3.379	490.2
Steel-3	-	-	3.309	480
Silica Sand-1	2.177	315.8	2.607	378.2
Silica Sand-2	3.854	559.0	1.703	247
Silica Sand-3	-	-	4.327	627.7
Calcined Clay-1	4.249	616.2	3.739	542.4
Calcined Clay-2	2.581	374.3	1.615	234.3
Calcined Clay-3	-	-	3.029	439.3
Glass Fiber-1	4.381	635.3	1.387	201.2
Glass Fiber-2	4.082	592.1	1.533	224.1
Glass Fiber-3	-	-	3.046	441.8

D.4 Additional SEM Micrographs

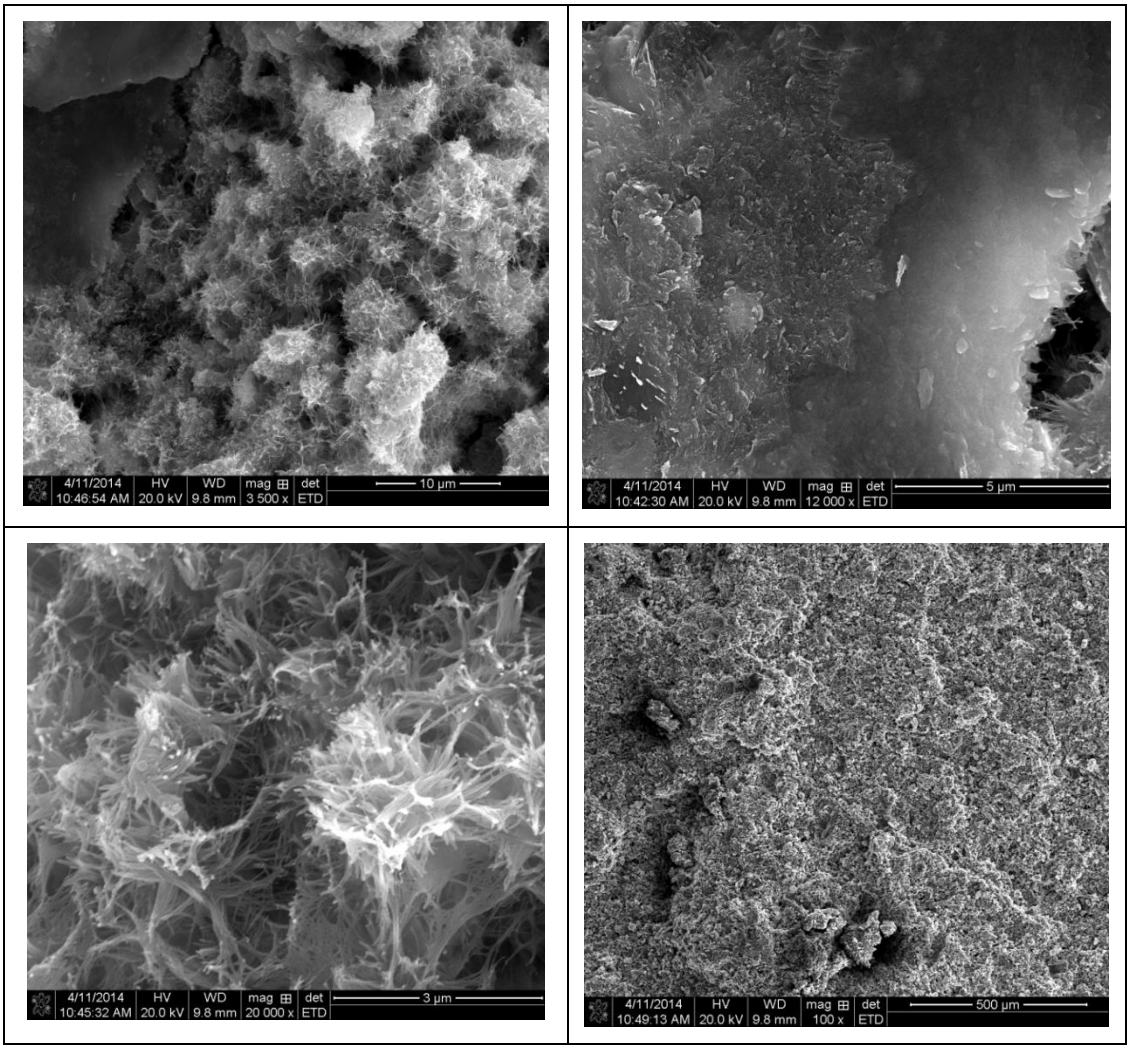

Figure D.1: Additional SEM micrographs of cement sample from neat cement design.

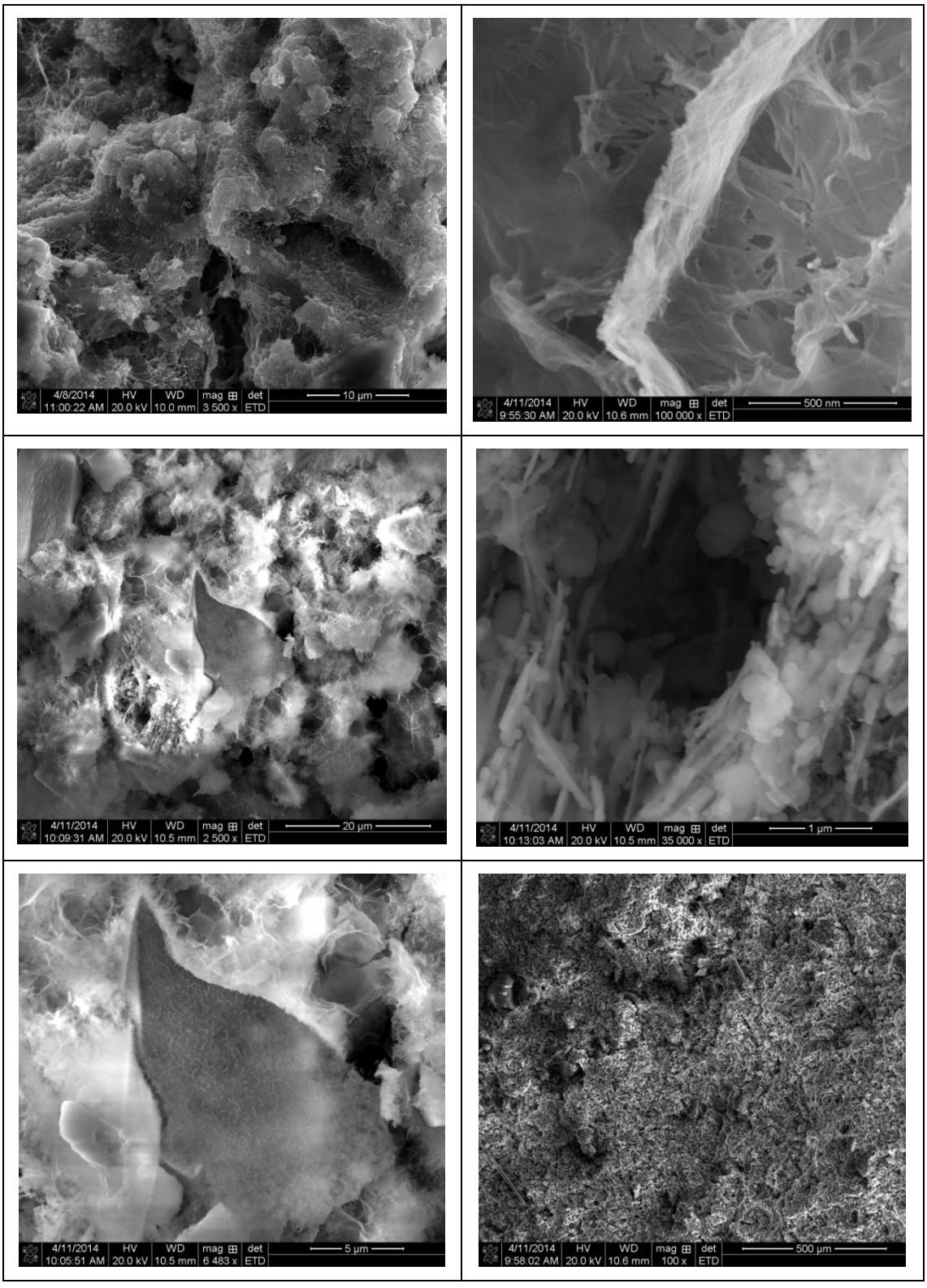

Figure D.2: Additional SEM micrographs of cement sample from steel fiber cement design.

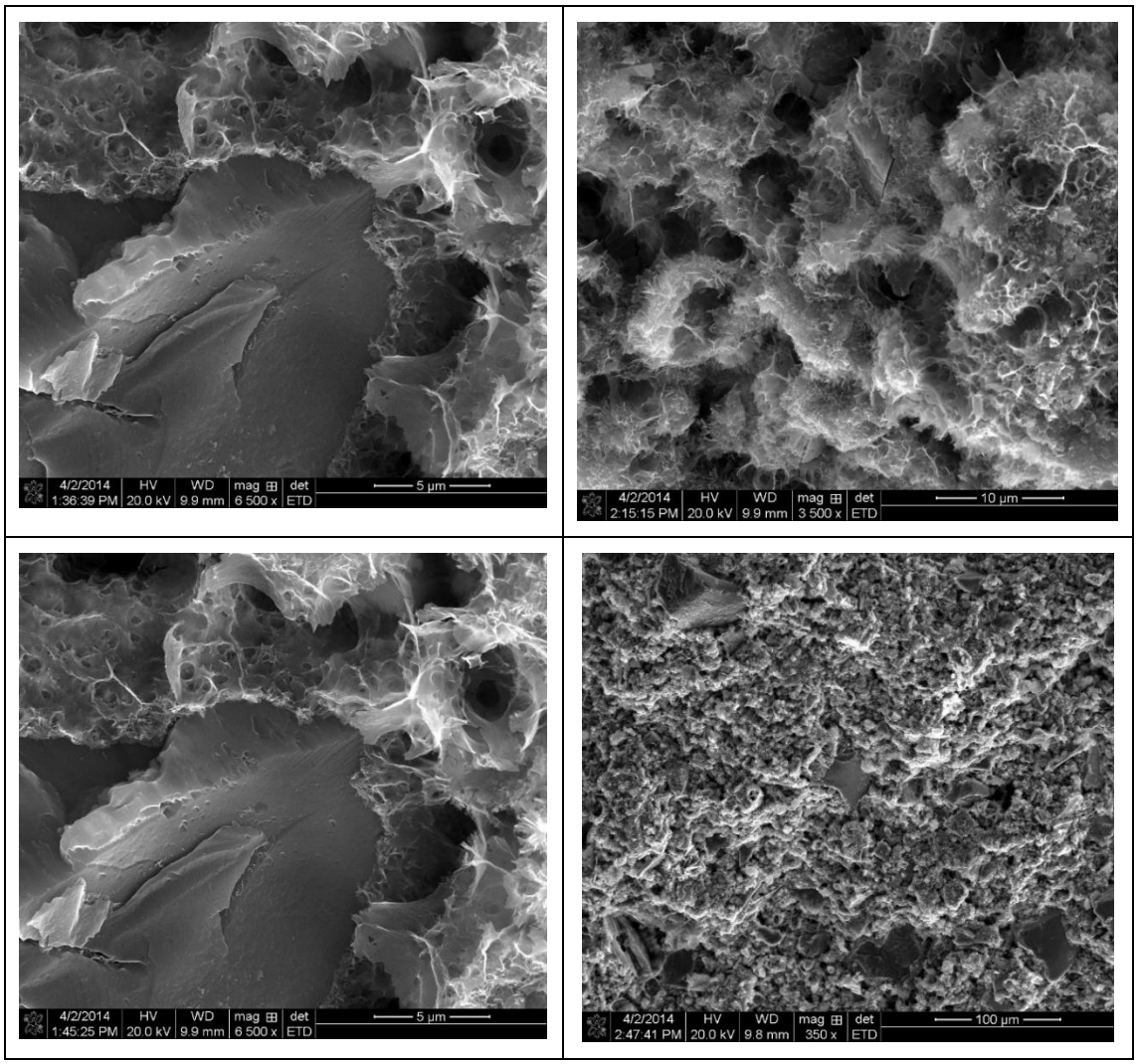

Figure D.3: Additional SEM micrographs of cement sample from the silica sand cement design.

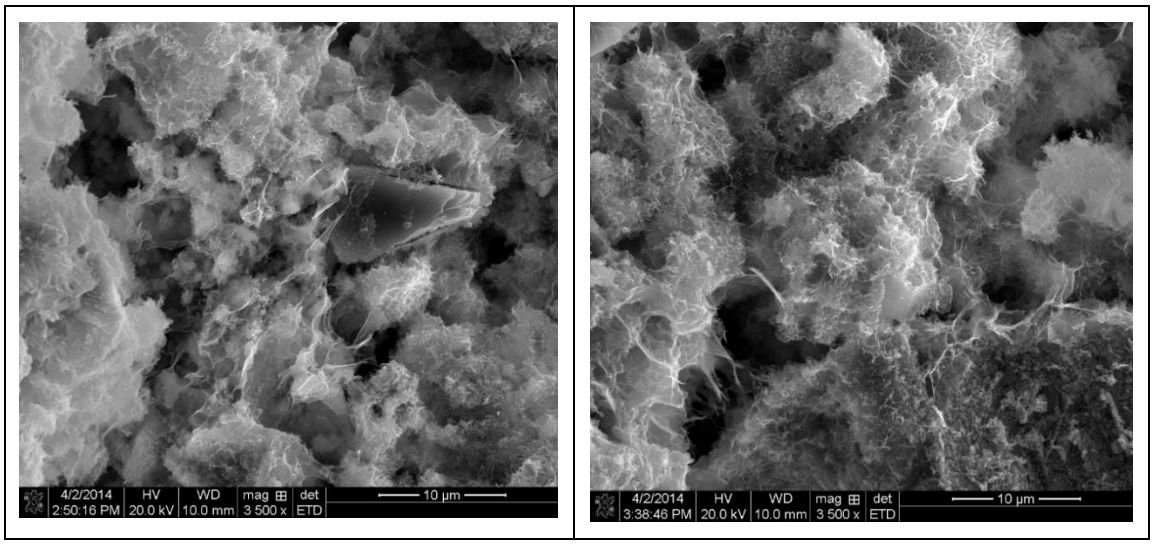

Figure D.4: Additional SEM micrographs of cement sample from the calcined clay cement design.

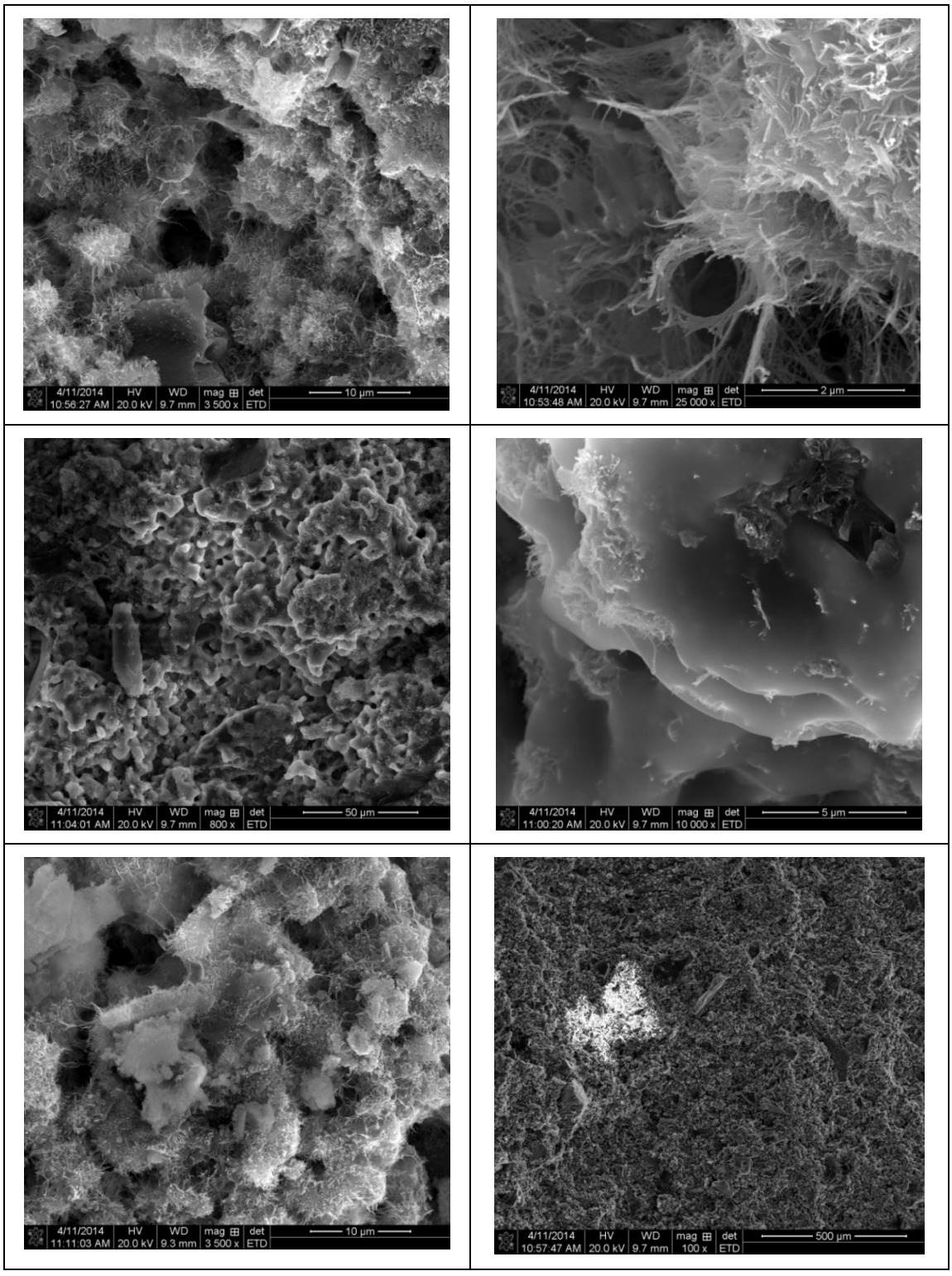

Figure D.5: Additional SEM micrographs of cement sample from the glass fiber cement design.

D.5 Post Experiment X-Ray Photoelectron Spectroscopy (XPS) Analysis

XPS analysis was done to evaluate the chemical difference between all the cement slurry designs. Of main importance are peaks of the calcium and silicon elements. The peaks of the both elements have very similar binding energy with slightly different intensities. These indicate that all the cement designs have very similar chemistry upon hydration. Shift in peaks signifies the presence of different calcium and silicon compounds in the two samples.

Table D.4: Raw XPS data for silicon, calcium, oxygen and iron element peaks for samples from neat cement design, steel fiber cement design and silica sand cement design after 100 TCL.

	Neat Cement		Steel Fiber Cement		Silica Sand Cement Design	
Element	Binding Energy (eV)	Intensity (CPS)	Binding Energy (eV)	Intensity (CPS)	Binding Energy (eV)	Intensity (CPS)
Si 2p	102	1563.8	102.4	1218.34	101.2	1791.3
Ca 2p	347.3	11387.2	346.4	5008.2	346.1	9264.6
O 1s	531.2	21242.4	531.6	10796.4	530.6	19329
Fe 2p	738.5	1261.4	716.4	3777.8	714.7	1261.3

Table D.5: Raw XPS peak data for silicon, calcium, oxygen and iron element peaks for samples from calcined clay cement design and silica sand cement design after 100 TCL.

	Calcined Clay Cement		Glass Fiber Cement	
Element	Binding Energy (eV)	Intensity (CPS)	Binding Energy (eV)	Intensity (CPS)
Si 2p	102.3	1888.8	101.6	2111.6
Ca 2p	347.1	11774	346.2	11279.7
O 1s	531.1	21969.5	530.3	23252.3
Fe 2p	710.9	1824.6	723.3	858.3

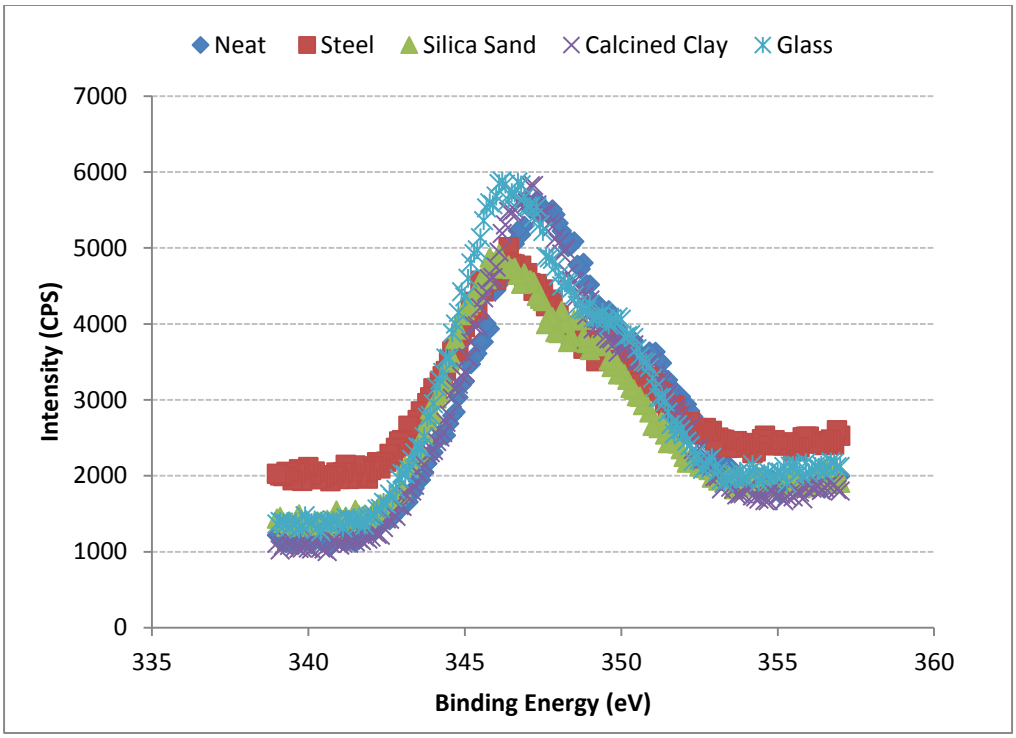

Figure D.6: XPS plots showing similar shift in the calcium peaks in cement samples after 100 thermal cycles.

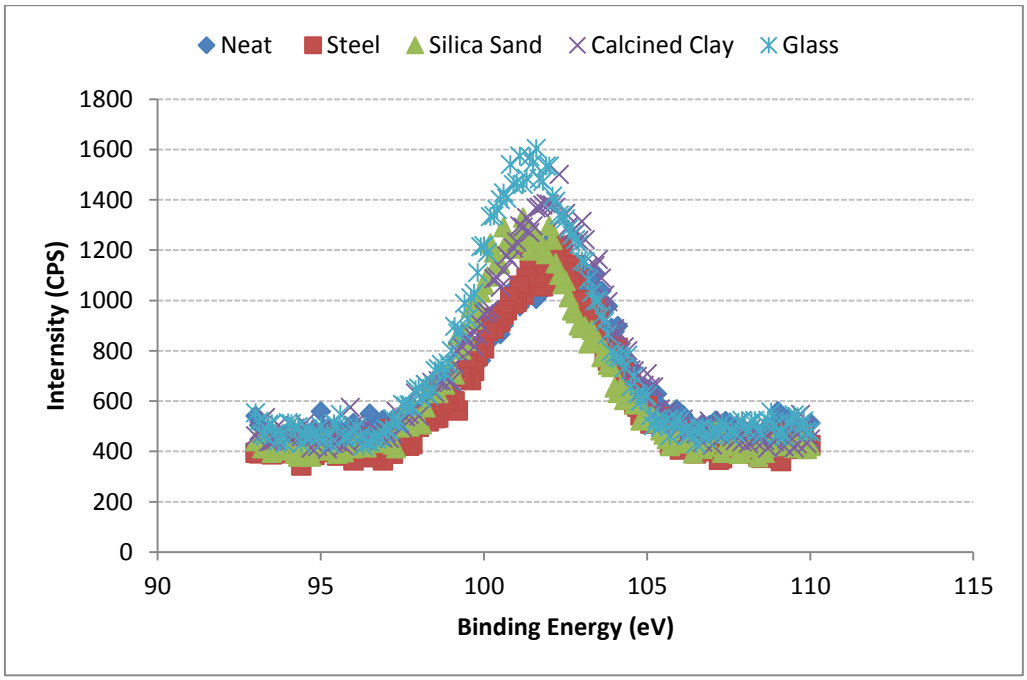

Figure D.7: XPS plots showing similar shift in the calcium peaks in cement samples after 100 thermal cycles

VITA

Kolawole Saheed Bello was born June 3, 1991 in Abeokuta, Ogun State, Nigeria. In 2007, he graduated from Omolaja Sodipo Memorial Anglican School in Abeokuta, Ogun State, Nigeria. He furthered his education by attending McNeese State University and then Louisiana State University where he received his Bachelor of Science in Petroleum Engineering and Bachelor of Science in Geology degrees in 2012. He co-authored two papers that were presented at the 48th US Rock Mechanics Geomechanics Symposium, in Minneapolis, MN and the 5th International Conference on Porous Media and its Applications in Science and Engineering held in Kona, HI. He also co-authored a poster that was presented at the 2013 American Geophysical Union Annual Fall Meeting in San Francisco, CA.